GROSS PROPERTIES OF HEAVY-ION TRANSFER REACTIONS

KAZUO MATSUOKA

(PH.D. THESIS)

DEPARTMENT OF PHYSICS, OSAKA UNIVERSITY

TOYONAKA, OSAKA 560, JAPAN

Abstract

A simple approximation to the semiclassical theory of heavy-ion transfer reactions is presented. For one-nucleon transfer reactions it reduces to the matching condition model given by Brink. Inelastic scattering and multinucleon transfer reactions can also be treated for either case in which heavy ions follow a straight-line trajectory or temporarily form a dinuclear system. For multistep process a binary-step approximation is introduced, in which some effects of the time differences between consecutive transfer events are taken into account.

This model is applied to the analysis of energy spectra, angular distributions and polarizations of outgoing particles. Reactions involving transfers of one, two and seven nucleons, one and two α-particles are treated. The energy spectra are well reproduced for low incident energy, but at high incident energy the agreement is not well. If the circular trajectory is assumed, the better agreement for the polarizations can be obtained than the straight-path trajectory.

Contents

Chapter I. Introduction

In heavy-ion transfer reactions populations of low-lying discrete states are rather well described by the direct reaction treatments such as the distorted wave Born approximation (DWBA). When the incident energy is well above the Coulomb barrier, continuous energy region is also strongly populated. Energy spectra and angular distributions of the transfer to the quasi-elastic region show the importance of direct reaction mechanism. Application of the DWBA formalism used for discrete levels to continuous region involves many difficulties, such as large angular momenta and many overlapping states. Parametrizing the transition amplitude or utilizing the local momentum, some authors proposed simple models based on the DWBA formalism and applied them to the reactions to continuous region.

Tamura, Udagawa and their group treated continuum energy spectra with fully quantum mechanical way.[1~4] Continuum cross section was given as a sum of products of exact-finite-range DWBA cross sections and spectroscopic densities, where the sum was taken over the spins of the final states. Overlap integrals were expressed in an analytic form, which includes the relevant quantum numbers, Q-values and several parameters. Exact-finite-range DWBA calculations were made for a few thousand sets of quantum numbers and Q-values. This was followed by a χ^2-fitting procedure to determine the parameters. The cross-section calculations were then carried out with considerable speed.

With this method they analyzed energy spectra, spin polarizations and angular distributions, assuming one-step or two-step processes. In these calculations parameters were determined for each reaction. The Q-value dependence of the form factor was neglected. Further, for each calculation different functional forms of level density were used, which largely affect the energy spectrum.

One-step no recoil DWBA transition matrix element was parametrized by Mermaz[5] on the basis of the diffraction model for inelastic excitation. Reduced matrix elements were related to the product of the derivatives of reflection coefficients in the entrance and exit channels. They include only a few free parameters, so the DWBA parametrization is extremely simple. He calculated angular distributions and continuum energy spectra. Analyses of experimental data for two-proton and alpha-transfer reactions were successful at low incident energies. On the other hand, energy spectrum of an alpha-transfer reaction at high incident energy could not be reproduced. In this model, recoil effect originating from mass transfer was neglected. Moreover, effects of multistep processes could not be included.

Mcvoy and Nemes[6] treated transfer reactions and projectile-breakup reactions with a simplified plane-wave Born approximation employing Coulomb-corrected local momenta. They discussed about the energy spectra especially its width and concluded that in the case of projectile fragmentation the Fermi motion within the projectile is responsible for the width of the spectrum. For the case of transfer reactions calculated perks are located at the energies near the ones for the breakup reactions, and widths are a little smaller than the values of the breakup calculation. In this treatment, distortion of the wave by the potential was neglected. Further, the effect of absorption by the imaginary potential was not included.

In this paper a simple model for analyzing continuous spectra is developed. Semiclassical approximation is made. Recoil effect to the first order of transferred mass is taken into account. This model was originally given by Brink[7] and applied to one-nucleon transfer reaction to low lying discrete levels. He gave three kinematical conditions for the transfer probability to be large. For a stripping reaction, they are

$$\Delta k = k_n - \lambda_1/R_1 - \lambda_2/R_2 \approx 0 \ , \tag{1.1}$$

$$\Delta L = \lambda_2 - \lambda_1 + \tfrac{1}{2} k_n (R_1 - R_2) + Q_{eff} R/\hbar v \approx 0, \tag{1.2}$$

and

$$\ell_1 + \lambda_1 = even \ , \qquad \ell_2 + \lambda_2 = even. \tag{1.3}$$

Here orbital angular momenta and their z-components of the transferred particle are denoted as ℓ_1, λ_1 and ℓ_2, λ_2 for the initial and final states, respectively. The z-axis is chosen to be the direction of $\mathbb{k}_f \times \mathbb{k}_i$ in the case of repulsive scattering, where $\mathbb{k}_f$ and $\mathbb{k}_i$ are the relative momenta in the final and initial channels. The radii of the two nuclei are R_1 and R_2, and $R = R_1 + R_2$. The relative velocity of the two nuclei in the region of transfer is $\mathbf{v}$, and $\mathbf{k}_n = m_n \mathbf{v}/h$, where m_n is the mass of the transferred nucleon. The effective Q-value is estimated from

$$Q_{eff} = Q - \frac{Z_1^f Z_2^f - Z_1^i Z_2^i}{R} e^2 \ , \tag{1.4}$$

where Z_1^f, Z_2^f and Z_1^i, Z_2^i are charges of the nuclei in the final and initial states, Q is the reaction Q-value.

The first condition, $\Delta k \approx 0$, requires that the y-component of the momentum of the transferred particle should be almost conserved, where the y-axis is the direction of $\mathbf{k}_n$. The second condition, $\Delta L \approx 0$, comes from conservation of the z-component of the total angular momentum. The last two terms of eq. (1.2) are the change in the z-component of angular momentum of relative motion. The last condition, eq. (1.3), arises from the requirement that the transfer should occur near the reaction plane.

With these kinematical conditions, relative intensities of cross section to discrete levels have been calculated for heavy ion transfer reactions.[8)]

In the following chapter we lay some foundations on Brink's matching condition model and extend it to the case of accelerated motion and to multi-nucleon transfer reactions. We derive an expression of transfer probability for heavy-ion reactions, starting from a semiclassical theory of Broglia and Winther.[9)] The mass of transferred particle is assumed to be much smaller than the masses of the projectile and the target. Further the particle is assumed to be transferred near the line joining the centers of the two nuclei. If the relative motion of the two nuclei in the region of transfer can be approximated by that of a constant velocity, the kinematical conditions of Brink are derived.

In heavy-ion reactions, interactions between two nuclei are large. Then the projectile may rotate around the target for a short time, especially in the case of low incident energy. We treat this situation with assuming circular trajectory for the relative motion. In many-nucleon transfer reactions or in the reactions transferred to high excited states, multistep processes play an important role. Transition amplitudes for higher order processes are given for the straight-line and the circular trajectories.

We calculate energy spectra and spin polarizations of outgoing particles with the product of the DWBA cross sections and the level densities of residual nuclei. The level density of one-particle excited states is assumed to be independent of the excitation energy. For the distribution of z-component of angular momentum we take a Gaussian form. The n-particle level densities are calculated from the one-particle level density.

Experimental data are analyzed with this model. The method was previously applied[10)] for the two nucleon transfer reaction $^{100}Mo(^{14}N, ^{12}B)$ at incident energy E_{lab} = 90 MeV.[11)] Energy spectra and polarization of the outgoing particle ^{12}B

were analyzed with the assumptions of one-step process and straight-line trajectory. The results showed good agreement with the experimental data in quasi-elastic region. Results of two-step process for straight-line trajectory are shown in this paper. Dependence of the energy spectra and the polarization on the level density parameter (temperature T) and on the rotation angle θ are studied for the case of circular trajectory of one-step and two-step processes. For incident energies of 125 MeV and 200 MeV,[12] the effect of friction is taken into account.

Polarization data of the reaction $^{197}Au(^{19}F, ^{12}B)$ at E_{lab} = 186 MeV show the same trend[2] as those of $^{100}Mo(^{14}N, ^{12}B)$ at E_{lab} = 90 MeV.[11] We also analyze this seven-nucleon transfer reaction as a one-step transfer process and compare it with the calculation by Ishihara et al.[2]

Frölich et al.[3] made the parametrized exact-finite-range DWBA calculations for three alpha-particle transfer reactions $(^{20}Ne, ^{16}O)$, $(^{14}N, ^{10}B)$ and $(^{13}C, ^{9}Be)$ on ^{40}Ca targets. For the reactions $(^{14}N, ^{10}B)$ and $(^{13}C, ^{9}Be)$, peaks and widths of energy spectra are well reproduced. For the reaction ^{40}Ca $(^{20}Ne, ^{16}O)$ the calculated results at forward angles showed a peak at the excitation energy $E^* \sim 80$ MeV, while the experimental peak was at lower excitation energy $E^* \sim 54$ MeV. This difference was attributed to a projectile-breakup and breakup-fusion process.[13] We also treat these transfer reactions assuming both straight-line and circular trajectories. Furthermore, calculations with the level density used by Frölich et al.[3] are made. Differences between their results and ours are discussed.

Angular distribution for these alpha-transfer reactions shows a forward angle peak. In our treatment angular distribution is estimated by the product of elastic cross section with transition probability. In this paper, the elastic cross section is calculated from classical deflection function.

One and two alpha-particle transfer reactions on ^{27}Al target at an incident

energy of 120 MeV[14] are also analyzed. The analysis was also made by Udagawa et al.[4] We compare our results with theirs.

In chapter II we develop a semiclassical theory of heavy-ion transfer reactions. When a straight line trajectory for the relative motion of two ions is assumed, the cross section expression reduces to that given by Brink.[7] Expression for the case of circular trajectory is also shown. Transition amplitudes for higher order process are presented.

In chapter III calculated results of energy spectra, angular distributions and polarizations of outgoing particles are compared with experimental data and with results of the other theoretical treatments.

Chapter IV is the summary and discussions, where we point out restricted applicabilities of a simle picture of direct reactions.

Chapter II. Formulation

§1. Introduction

In heavy-ion transfer reactions, transitions to low-lying discrete states of nuclei are well described by the distorted wave Born approximation (DWBA) method. When the incident energy is well above the Coulomb barrier and/or large numbers of nucleons are transferred, the quasielastic scattering part of the reaction turns over its role to the deeply inelastic collision process. In order to understand the reaction mechanism of the latter process from the viewpoint of the direct reaction theory, it is important to study firstly the applicability of the DWBA method for the analysis of the continuous energy spectra of quasielastic nature.

Along this line, Tamura, Udagawa and their group[1~4] have done detailed calculations on the energy spectra of one- and two-step processes. They used a method called as the multistep direct reaction theory, in which the overlap integrals obtained in the full-recoil DWBA are suitably parametrized. On the other hand, Mermaz[5] simplified the no-recoil DWBA by applying the diffraction model. The overlap integral is related to the product of the derivatives of the reflection coefficients in the entrance and exit channels, for which the strong absorption model is used. It is to be noted that Mermaz could fit the angular distributions of the transitions to the discrete levels. He extracted the level density parameters of the residual nuclei by comparing calculation with experiment.

The purpose of this chapter is to develop a simple DWBA model which can be applied to the analysis of continuous spectra. We use a semiclassical approximation and take into account the recoil effect to the first order in the transferred mass. The model was originally given by Brink[7,15] for the case of one-particle transfer. From the classical argument and simplified semiclassical calculation for the relative motion with a constant velocity,

he derived the cross-section formula which incorporates the conservations of the linear and angular momenta in the transfer process. In the classical limit the expression for the optimum Q-value agrees with that given by Siemens et al,[16] which could explain the relation of the optimum Q-value with the number of transferred nucleons. The relative populations of the final states in the one-cluster transfer reaction can be understood with Brink's model. The model was applied by Ishihara et al.[10] to the analysis of the continuous energy spectra and polarization of the outgoing ion in the ^{100}Mo (^{14}N, ^{12}B) ^{102}Ru reaction and showed good agreement with the experimental data in the quasielastic region. Here we lay some foundations on Brink's matching condition model and extend it to the case of the accelerated motion and to the multinucleon transfer.

In sect.2 we derive the expression for the form factor of the one-nucleon transfer process, starting from the semiclassical theory of Broglia and Winther.[9] It is shown in sect.3 that when the trajectory of the relative motion of heavy ions can be approximated by a straight line, the cross-section expression reduces to that given by Brink. In that section we consider an extension of the method to the cases of the circular orbital motion and of the inelastic scattering. Transition amplitudes for higher order processes are given in sect.4. For the straight-line trajectory, we propose a simple approximation which takes into account partly the effect of time differences between consecutive transfer events. In sect.5 we give a short discussion on the energy spectra obtained by our method. Expressions for the optimum Q-value and the half width of the spectrum are derived. Finally we make some discussions in sect.6.

§2. General formulation

We consider a reaction

$$A + b \longrightarrow a + B \ , \tag{2.1}$$

in which a cluster of nucleons n is transferred from the projectile A to the target b leading to a residual nucleus B, so that

$$A = a + n \ , \quad B = b + n \ . \tag{2.2}$$

We follow Broglia and Winther.[9] The angular momentum quantum numbers of the states of A are denoted as $I_A M_A$, and similarly for the others. In the semiclassical theory, the differential cross section is given by

$$d\sigma/d\Omega = (d\sigma/d\Omega)_{el} \cdot P \ , \tag{2.3}$$

where $(d\sigma/d\Omega)_{el}$ is the elastic scattering cross section while P is the transfer probability

$$P = (\hat{I}_A \ \hat{I}_b)^{-2} \sum_{\{M\}} |c_{if}|^2 \ , \tag{2.4}$$

in which $\hat{I}$ means $(2I + 1)^{1/2}$.

The first-order approximation for the transition amplitude is given by

$$c_{if}^{(1)} = (i\hbar)^{-1} \int_{-\infty}^{\infty} f_{if}^{(1)}(t)\, dt \ , \tag{2.5}$$

where

$$f_{if}^{(1)}(t) = \left(\tilde{\Phi}^{aB}(t), \ \Delta V \ \tilde{\Phi}^{Ab}(t) \right). \tag{2.6}$$

The perturbing interaction is denoted as ΔV, for which we will take the prior representation. The product wave function in the incident channel is given by

$$\tilde{\Phi}^{Ab}(t) = \Psi^A \Psi^b \exp\left[(i\hbar)^{-1}\int_0^t U_{Ab}(R_{Ab}(t'))\,dt'\right]. \quad (2.7)$$

Here U_{Ab} is the average interaction between A and b, dependent on the relative coordinate R_{Ab}. When the center of mass of a nucleus consisting of N particles is moving, its wave function Ψ in the laboratory system is connected with that of the intrinsic coordinate system, ψ, by

$$\Psi(\{r_i\}) = \psi(\{r_i - R(t)\})\, e^{i(\varphi(t) - Et)/\hbar}, \quad (2.8)$$

where

$$\{r_i\} = r_1, r_2, \cdots, r_N, \quad (2.9)$$

and the origin of the intrinsic system is specified by the classical variable $\mathbf{R}(t)$. The phase factor $\varphi(t)$ is given by

$$\varphi(t) = \mathbf{v}(t)\cdot\sum_{i=1}^{N} m_i r_i - \int_0^t \left\{m v^2(t')/2 + m R(t')\cdot\dot{v}(t')\right\}dt', \quad (2.10)$$

where $\mathbf{v}(t) = \dot{\mathbf{R}}(t)$ and m is the total mass equal to $\Sigma_{i=1}^{N} m_i$. We will choose $t = 0$ as the time of closest approach where the particle transfer takes place. We demand that the intrinsic wave function satisfies the Schrödinger equation $H\psi = E\psi$, where H is the hamiltonian of the nucleus. In the appendix a detailed derivation of eq. (2.5) is given.

The form factor $f^{(1)}_{if}(t)$ can be written as

$$
\begin{aligned}
f^{(1)}_{if}(t) = \int & d\tau_a \, d\tau_b \, d\mathbf{r}_n \; e^{-i\Delta E t/\hbar} \\
& \cdot \psi_a^*(\{\mathbf{r}_i - \mathbf{R}_A\}) \, \psi_B^*(\{\mathbf{r}_i - \mathbf{R}_B\}) \, \Delta V \, \psi_A(\{\mathbf{r}_i - \mathbf{R}_A\}) \, \psi_b(\{\mathbf{r}_i - \mathbf{R}_b\}) \\
& \cdot \exp\Big[\frac{1}{i\hbar} \Big\{ (m_a \mathbf{r}_a \cdot \mathbf{v}_a + m_B \mathbf{r}_B \cdot \mathbf{v}_B - m_A \mathbf{r}_A \cdot \mathbf{v}_A - m_b \mathbf{r}_b \cdot \mathbf{v}_b) \\
& \quad + \frac{1}{2} \int_0^t (m_A v_A^2 + m_b v_b^2 - m_a v_a^2 - m_B v_B^2) \, dt' \\
& \quad + \int_0^t (m_A \mathbf{R}_A \cdot \dot{\mathbf{v}}_A + m_b \mathbf{R}_b \cdot \dot{\mathbf{v}}_b - m_a \mathbf{R}_a \cdot \dot{\mathbf{v}}_a - m_B \mathbf{R}_B \cdot \dot{\mathbf{v}}_B) \, dt' \\
& \quad + \int_0^t \{ U_{Ab}(R_{Ab}(t')) - U_{aB}(R_{aB}(t')) \} \, dt' \Big\} \Big] ,
\end{aligned}
\tag{2.11}
$$

where

$$
\Delta E = E_A + E_b - E_a - E_B , \tag{2.12}
$$

and the c.m. coordinates of each nucleus are denoted as $\mathbf{r}_A$ etc., i.e.

$$
m_A \mathbf{r}_A = \sum_{i \in A} m_i \mathbf{r}_i . \tag{2.13}
$$

We rewrite the exponent in eq. (2.11). By introducing the c.m. and relative coordinates between A and b,

$$
M \mathbf{r}_{cm} = m_A \mathbf{r}_A + m_b \mathbf{r}_b , \qquad M = m_A + m_b , \tag{2.14a}
$$

$$\mathbf{r}_{Ab} = \mathbf{r}_A - \mathbf{r}_b , \qquad m_{Ab} = m_A m_b / M , \tag{2.14b}$$

$$M \mathbf{v}_{cm} = m_A \mathbf{v}_A + m_b \mathbf{v}_b , \qquad \mathbf{v}_{Ab} = \mathbf{v}_A - \mathbf{v}_b , \tag{2.14c}$$

and similarly for B and a, we have

$$\begin{aligned}
& m_a \mathbf{r}_a \cdot \mathbf{v}_a + m_B \mathbf{r}_B \cdot \mathbf{v}_B - m_A \mathbf{r}_A \cdot \mathbf{v}_A - m_b \mathbf{r}_b \cdot \mathbf{v}_b \\
&= (m_a \mathbf{r}_a \cdot \mathbf{v}_a + m_B \mathbf{r}_B \cdot \mathbf{v}_B - M \mathbf{r}_{cm} \cdot \mathbf{v}_{cm}) - (m_A \mathbf{r}_A \cdot \mathbf{v}_A + m_b \mathbf{r}_b \cdot \mathbf{v}_b - M \mathbf{r}_{cm} \cdot \mathbf{v}_{cm}) \\
&= \frac{1}{M}\{(m_a + m_B) m_a \mathbf{r}_a \cdot \mathbf{v}_a + (m_a + m_B) m_B \mathbf{r}_B \cdot \mathbf{v}_B - (m_a \mathbf{r}_a + m_B \mathbf{r}_B) \cdot (m_a \mathbf{v}_a + m_B \mathbf{v}_B)\} \\
&\quad - \frac{1}{M}\{(m_A + m_b) m_A \mathbf{r}_A \cdot \mathbf{v}_A + (m_A + m_b) m_b \mathbf{r}_b \cdot \mathbf{v}_b - (m_A \mathbf{r}_A + m_b \mathbf{r}_b) \cdot (m_A \mathbf{v}_A + m_b \mathbf{v}_b)\} \\
&= \frac{1}{M} m_a m_B (\mathbf{r}_a \cdot \mathbf{v}_a + \mathbf{r}_B \cdot \mathbf{v}_B - \mathbf{r}_a \cdot \mathbf{v}_B - \mathbf{r}_B \cdot \mathbf{v}_a) - \frac{1}{M} m_A m_b (\mathbf{r}_A \cdot \mathbf{v}_A + \mathbf{r}_b \cdot \mathbf{v}_b - \mathbf{r}_A \cdot \mathbf{v}_b - \mathbf{r}_b \cdot \mathbf{v}_A) \\
&= m_{aB} \mathbf{r}_{aB} \cdot \mathbf{v}_{aB} - m_{Ab} \mathbf{r}_{Ab} \cdot \mathbf{v}_{Ab} .
\end{aligned} \tag{2.15}$$

Making use of the relation (see fig.1)

$$\mathbf{r}_{Ab} = \mathbf{r}_{ab} + (m_n / m_A) \mathbf{r}_{na} , \tag{2.16a}$$

$$\mathbf{r}_{aB} = \mathbf{r}_{ab} - (m_n / m_B) \mathbf{r}_{nb} , \tag{2.16b}$$

we can write eq. (2.15) as

$$\begin{aligned}
& m_{aB} \mathbf{r}_{aB} \cdot \mathbf{v}_{aB} - m_{Ab} \mathbf{r}_{Ab} \cdot \mathbf{v}_{Ab} \\
&= (m_{aB} \mathbf{v}_{aB} - m_{Ab} \mathbf{v}_{Ab}) \cdot (\mathbf{r}_{Ab} + \mathbf{r}_{aB}) / 2 - \sigma(\mathbf{r}_n, t) ,
\end{aligned} \tag{2.17}$$

where

$$\sigma(\mathbf{r}_n, t) = \hbar \mathbf{k}_0 \cdot (\mathbf{r}_{Ab} - \mathbf{r}_{aB})$$
$$= \hbar \mathbf{k}_0 \cdot \left\{ (m_n/m_A)\mathbf{r}_{na} + (m_n/m_B)\mathbf{r}_{nb} \right\}, \tag{2.18}$$

$$\hbar \mathbf{k}_0(t) = (m_{Ab}\mathbf{v}_{Ab} + m_{aB}\mathbf{v}_{aB})/2. \tag{2.19}$$

Exponentials in eq. (2.11), dependent on the kinetic energy and accelelation, can be rewritten by use of the relations similar to that of eq. (2.15), i.e.,

$$m_A v_A^2 + m_b v_b^2 - m_a v_a^2 - m_B v_B^2 = m_{Ab} v_{Ab}^2 - m_{aB} v_{aB}^2, \tag{2.20a}$$

$$m_A \mathbf{R}_A \cdot \dot{\mathbf{v}}_A + m_b \mathbf{R}_b \cdot \dot{\mathbf{v}}_b - m_a \mathbf{R}_a \cdot \dot{\mathbf{v}}_a - m_B \mathbf{R}_B \cdot \dot{\mathbf{v}}_B$$
$$= m_{Ab} \mathbf{R}_{Ab} \cdot \mathbf{v}_{Ab} - m_{aB} \mathbf{R}_{aB} \cdot \dot{\mathbf{v}}_{aB}. \tag{2.20b}$$

Then the total phase factor of the form factor becomes

$$(i/\hbar)\left\{ \sigma(\mathbf{r}_n, t) - (\Delta E\, t + \gamma(t)) \right\}, \tag{2.21}$$

where

$$\gamma(t) = \int_0^t (m_{Ab} v_{Ab}^2/2 + U_{Ab}(R_{Ab}))\, dt'$$
$$- \int_0^t (m_{aB} v_{aB}^2/2 + U_{aB}(R_{aB}))\, dt'$$
$$+ \int_0^t (m_{Ab} \mathbf{R}_{Ab} \cdot \dot{\mathbf{v}}_{Ab} - m_{aB} \mathbf{R}_{aB} \cdot \dot{\mathbf{v}}_{aB})\, dt'$$
$$+ (m_{aB} \mathbf{v}_{aB} - m_{Ab} \mathbf{v}_{Ab}) \cdot (\mathbf{R}_{Ab} + \mathbf{R}_{aB})/2. \tag{2.22}$$

In the last term of eq. (2.22) we have made use of the basic assumption of equating the dynamical variables for the center of mass with corresponding classical variables, i.e.,

$$r_{Ab} = R_{Ab}(t) \ , \qquad r_{aB} = R_{aB}(t) . \tag{2.23}$$

Using the identity

$$\begin{aligned} \tfrac{1}{2}(m_{aB}\mathbb{v}_{aB} - m_{Ab}\mathbb{v}_{Ab})\cdot(R_{Ab} + R_{aB}) &= \tfrac{1}{2}\int (R_{Ab}+R_{aB})\cdot(m_{aB}\dot{\mathbb{v}}_{aB} - m_{Ab}\dot{\mathbb{v}}_{Ab})\,dt' \\ &+ \tfrac{1}{2}\int (\mathbb{v}_{aB}+\mathbb{v}_{Ab})\cdot(m_{aB}\mathbb{v}_{aB} - m_{Ab}\mathbb{v}_{Ab})\,dt' - \tfrac{1}{2}(m_{aB}\mathbb{v}_{aB} - m_{Ab}\mathbb{v}_{Ab})\cdot(R_{Ab}+R_{aB})\Big|_{t'=0}, \end{aligned} \tag{2.24}$$

and expanding the potential energy

$$\begin{aligned} U_{Ab}(R_{Ab}) - U_{aB}(R_{aB}) &\approx U_{Ab}(R) - U_{aB}(R) \\ &+ \tfrac{1}{2}(R_{Ab} - R_{aB})\cdot(\nabla U_{Ab}(R) + \nabla U_{aB}(R)), \end{aligned} \tag{2.25}$$

we have the phase factor $\gamma(t)$ as

$$\gamma(t) = \int_0^t (U_{Ab}(R) - U_{aB}(R))\,dt' + \tfrac{1}{2}(m_{aB} - m_{Ab})\int_0^t v^2\,dt' . \tag{2.26}$$

Here R denotes the average position,

$$R(t) = (R_{Ab}(t) + R_{aB}(t)) / 2 . \tag{2.27}$$

In eq. (2.26), we have left out the last term of eq. (2.24), which is the time-independent phase factor.

By carrying out the integration over the coordiantes τ_a and τ_b of the cores a and b, we have for the nuclear overlaps

$$\int \psi_a^*(\{\mathbf{r}_i - \mathbf{R}_a\})\, \psi_A(\{\mathbf{r}_i - \mathbf{R}_A\})\, d\tau_a = \sum_i (I_a M_a j_i m_i | I_A M_A)\, B_i\, \varphi_i(\mathbf{r}_n - \mathbf{R}_a), \quad (2.28a)$$

$$\int \psi_B^*(\{\mathbf{r}_i - \mathbf{R}_B\})\, \psi_b(\{\mathbf{r}_i - \mathbf{R}_b\})\, d\tau_b = \sum_i (I_b M_b j_f m_f | I_B M_B)\, B_f^*\, \varphi_f(\mathbf{r}_n - \mathbf{R}_b), \quad (2.28b)$$

where B_i and B_f are the spectroscopic amplitudes of a bound particle with angular momenta $j_i m_i$ and $j_f m_f$ in the systems A and B, respectively. Corresponding one-particle wave functions are denoted by φ_i and φ_f.

Then we can write the form factor as the sum of

$$f_{if}^{(1)} = e^{(\Delta E\, t + \gamma(t))/i\hbar}\, f(t). \quad (2.29)$$

In the prior representation, f(t) is given by

$$f(t) = N_{if} \int \varphi_f^*(\mathbf{r}_{nb})\, V_f(r_{nb})\, \varphi_i(\mathbf{r}_{na})\, e^{i\sigma(\mathbf{r}_n, t)/\hbar}\, d\mathbf{r}_n, \quad (2.30)$$

where

$$N_{if} = B_i\, B_f^* (I_a M_a j_i m_i | I_A M_A)(I_b M_b j_f m_f | I_B M_B), \quad (2.31)$$

and

$$\Delta V \simeq V_f(r_{nb}). \quad (2.32)$$

§3. Approximate evaluations of the form facor and the transition amplitude

We now consider the integral over $\mathbf{r}_n$ in the form factor. Broglia and Winther[9] adopted the following approximation for $\sigma(\mathbf{r}_n,t)$

$$\sigma(\mathbf{r}_n, t) \approx (m_n V/\hbar)\cdot(\mathbf{r}_n - \mathbf{R}_\alpha(t)), \tag{3.1}$$

by introducing the coordinate

$$\mathbf{R}_\alpha(t) = (m_B \mathbf{r}_a + m_A \mathbf{r}_b)/(m_A + m_B)\,. \tag{3.2}$$

With this approximation, the essential feature of $\sigma(\mathbf{r}_n,t)$ as describing the effect of recoil or momentum mismatch can not be clearly extracted. To remedy this, we express $\sigma(\mathbf{r}_n,t)$ in a different way,

$$\sigma(\mathbf{r}_n, t) = \left(\frac{m_n}{m_A} + \frac{m_n}{m_B}\right)\hbar\mathbf{k}_0\cdot\mathbf{r}_{nb} - \frac{m_n}{m_A}\hbar\mathbf{k}_0\cdot\mathbf{R}_{ab}\,. \tag{3.3}$$

where $\mathbf{R}_{ab} = \mathbf{R}_a - \mathbf{R}_b$. We can expect that the main contribution to the reaction comes from the region where r_{nb} is nearly equal to the target radius R_2, because of the presence of $V_f(r_{nb})$ in eq. (2.30). We put

$$\mathbf{r}_{nb} = \mathbf{R}_2 + \mathbf{y}' + \mathbf{z}'\,. \tag{3.4}$$

As shown in fig. 2, $\mathbf{R}_2$ is the vector having the magnitude R_2 and the direction $\mathbf{R}_{ab}$, while $\mathbf{y}'$ and $\mathbf{z}'$ are perpendicular to $\mathbf{R}_{ab}$. Defining $\boldsymbol{\rho}_1$ by

$$\mathbf{R}_{ab} = \mathbf{R}_2 + \boldsymbol{\rho}_1\,, \tag{3.5}$$

we approximate $\sigma(\mathbf{r}_n,t)$ as

$$\sigma(r_n,t) \simeq \hbar k_n \cdot y' + \sigma'(t) , \tag{3.6}$$

where

$$\hbar k_n = m_n v , \tag{3.7}$$

$$\sigma'(t) = \hbar k_0 \cdot \left(\frac{m_n}{m_B} R_2 - \frac{m_n}{m_A} \beta_1 \right) . \tag{3.8}$$

As the second term of eq. (3.6) does not depend on $\mathbf{r}_n$, it can be taken out from the integral on $\mathbf{r}_n$, which we write as

$$I = \int \varphi_f^*(r)\ V_f(r)\ \varphi_i(r - R_{ab})\, e^{i k_n \cdot y'} d\mathbf{r} \tag{3.9}$$

For the peripheral collision, the integrand contains $\varphi_i \sim \exp(-\gamma_1 |r - R_{ab}|)$, which is maximum if the transferred particle is in the region between two nuclei near the reaction plane.

So we can set the polar coordinates (θ,ϕ) and (θ',ϕ') of the vectors $\mathbf{r} - \mathbf{R}_{ab}$ and $\mathbf{r}$, respectively,

$$\theta \approx \theta' \approx \pi/2 , \tag{3.10a}$$

and

$$y' = \beta_1 \phi_1 = R_2 \phi_2 , \tag{3.10b}$$

where

$$\phi = \phi_0 + \phi_2 , \quad \phi' = \phi_0 + (\pi - \phi_1) . \tag{3.11}$$

Here $\pi - \phi_1$ and ϕ_2 are the azimuthal angles of these vectors in the body-fixed system, and ϕ_0 is the angle between the laboratory x-axis and the body—fixed x'-axis.

In the integrand of eq. (3.9), $u_f(r)$, the radial part of $\varphi_f(r)$, and $V_f(r)$ are evaluated at $r = R_2$, while $u_i(r')$ is approximated by the asymptotic form

$$u_i(r') \approx N_i\, e^{-\gamma_1 r'} . \tag{3.12}$$

Here γ_1 is related to the binding energy ε_1 of the initial state by $\gamma_1^2 = 2m_n \varepsilon_1/\hbar^2$. Expanding $r' = |\mathbf{r} - \mathbf{R}_{ab}|$ as

$$r' = (\rho_1^2 + y'^2)^{1/2} \approx \rho_1 + y'^2/2\rho_1 , \tag{3.13}$$

we find

$$u_i(r') = u_i(\rho_1)\exp(-y'^2/\Delta_y^2), \quad \Delta_y^2 = 2\rho_1/\gamma_1 . \tag{3.14}$$

Effective extensions of the integrand in the x' and z' directions are taken to have Gaussian shapes with widths Δ_x and Δ_z, respectively, both of which are of the orders of magnitudes of nuclear radii. Retaining the azimuthal angular parts and the tail part of the wave functions in the integrand, eq. (3.9) reduces to

$$I \approx I_0 R_2 \int \exp\left[-R_2^2\phi_2^2/\Delta_y^2 + i\left(k_n R_2 \sin\phi_V - \lambda_1 R_2/\rho_1 - \lambda_2\right)\phi_2\right] d\phi_2 , \tag{3.15}$$

where

$$I_0 = \pi \Delta_x \Delta_z \, e^{i\pi\lambda_1} \, Y^*_{\ell_2\lambda_2}\left(\tfrac{\pi}{2}, \phi_0\right) Y_{\ell_1\lambda_1}\left(\tfrac{\pi}{2}, \phi_0\right) U^*_f(R_2) V_f(R_2) U_i(R_1)$$

$$\times \left(\ell_1 \lambda_1 \tfrac{1}{2} \sigma_n \mid j_1 m_1\right) \left(\ell_2 \lambda_2 \tfrac{1}{2} \sigma_n / j_2 m_2\right). \tag{3.16}$$

By extending the limits to $\pm \infty$, we have

$$I \approx I_0 \sqrt{\pi} \, \Delta_y \exp\left[-\left(R_{ab} \Delta k' / \sigma_1'\right)^2 / 2\right], \tag{3.17}$$

in which

$$\Delta k' = k_n \sin\phi_v - \lambda_1/R_1 - \lambda_2/R_2, \tag{3.18}$$

$$\sigma_1'^2 = 2 R_{ab}^2 / \Delta_y^2, \tag{3.19}$$

where ϕ_v is the angle of v in the body-fixed system.

Now we consider the time dependence of the form factor. The reaction Q-value is defined by

$$m_{aB} v^2_{aB}(t=+\infty)/2 = m_{Ab} v^2_{Ab}(-\infty)/2 + Q, \tag{3.20}$$

and is equal to ΔE, eq. (2.12). Comparing the energies before and after the transfer which is assumed to occur at t=0, the instant of closest approach, we define the effective Q-value by

$$m_{aB} v_{aB}^2(+0)/2 = m_{Ab} v_{Ab}^2(-0)/2 + Q_{eff}. \tag{3.21}$$

This gives

$$Q_{eff} = E_A + E_b - (E_a + E_B) + U_{Ab}(t=0) - U_{aB}(t=0). \quad (3.22)$$

The potential energy difference can be taken to be $(Z_A Z_b - Z_a Z_B)e^2/R_{AB}$. We make the approximation that

$$\gamma(t)/t \approx U_{Ab}(0) - U_{aB}(0) + \frac{1}{2}(m_{aB} - m_{Ab})\cdot v^2(0). \quad (3.23)$$

Then we have

$$\Delta E + \gamma(t)/t \approx Q_{eff} + v^2(0)\,\delta\mu/2, \quad (3.24)$$

where $\delta\mu = m_{aB} - m_{Ab}$.

In the evaluation of $\sigma'(t)$ term, we notice the relation[7]

$$m_n(R_2/m_B - \rho_1/m_A) = m_n\{(1/m_A + 1/m_B)(R_2 - \rho_1) + (1/m_B - 1/m_A)(R_2 + \rho_1)\}/2$$

$$\approx \{m_n(R_2 - \rho_1) + R_{ab}\,\delta\mu\}/2\mu, \quad (3.25)$$

in which $\mu = (m_{aB} + m_{Ab})/2$. We assume that for small t the relative motion of heavy ions can be approximated by a straight path along the y-axis, the tangent to the orbit at the distance of closest approach. We take the coordinate system as shown in fig.3. If we denote the y component of $\mathbf{R}_{ab}$ by y, the y components of ρ_1 and $\mathbf{R}_2$ are $(\rho_1/R_{ab})y$ and $(R_2/R_{ab})y$, respectively. We have approximately

$$y \approx vt , \tag{3.26}$$

and so

$$\sigma'(t) = \frac{1}{2} m_n v^2 \frac{R_2 - \rho_1}{R_{ab}} t + \frac{1}{2} \delta\mu v^2 t \tag{3.27}$$

This gives

$$\Delta E t + \gamma(t) - \sigma'(t) = Q_{eff} t - \frac{1}{2} m_n v^2 \frac{R_2 - \rho_1}{R_{ab}} t . \tag{3.28}$$

Again we take the asymptotic form for u_i and write

$$u_i(|R_{ab}(t) - R_2|) \approx e^{-\gamma_1(R_{ab}(t) - d)} u_1(d - R_2), \tag{3.29}$$

d being the closest distance of approach for grazing scattering angle.

The relative distance $R_{ab}(t)$ can be written as

$$R_{ab}(t) = \{d^2 + (vt)^2\}^{1/2} \approx d + (vt)^2/2d . \tag{3.30}$$

Putting $\phi_v = \pi/2 - \phi_0$ and using the approximation $\phi_0 \simeq vt/d$, the form factor can be expressed as

$$f_{if}^{(1)}(t) = N_{if}^{(1)} \exp\left[-(d\Delta k/\sigma_1)^2/2\right] \exp(-\eta t^2 - i\omega_{if} t) . \tag{3.31}$$

Here we have defined

$$N_{if}^{(1)} = N_{if}\,\pi^{3/2}\,\Delta x\,\Delta y\,\Delta z\; e^{i\pi\lambda_1}\; Y_{\ell_1\lambda_1}(\pi/2,0)\; Y^{*}_{\ell_2\lambda_2}(\pi/2,0)$$
$$\cdot(\ell_1\lambda_1\,\tfrac{1}{2}\sigma_n\,|\,j_i m_i)\,(\ell_2\lambda_2\,\tfrac{1}{2}\sigma_n\,|\,j_f m_f)\;\exp\left[-\gamma_1(d-R)\right]$$
$$\cdot U_f(R_2)\,V_f(R_2)\,U_i(R_1), \tag{3.32}$$

$$\eta = (\sigma_2 v/d)^2/2\,, \quad \sigma_1^2 \simeq \gamma_1 d^2/\rho_0\,, \quad \sigma_2^2 \simeq \gamma_1 d, \tag{3.33}$$

$$\omega_{if} = \Delta L\,(v/d)\,, \qquad R = R_1 + R_2\,, \qquad \rho_0 = d - R_2, \tag{3.34}$$

$$\Delta k = k_n - \lambda_1/\rho_0 - \lambda_2/R_2\,, \tag{3.35a}$$

$$\Delta L = \lambda_2 - \lambda_1 + k_n(\rho_0 - R_2)/2 + Q_{eff}\,d/\hbar v, \tag{3.35b}$$

and we have neglected the t dependence of I in eq. (3.18). According to Brink,[7] the transition probability can be expected to be large if Δk is smaller than π/Δ_y, where the spatial extension Δ_y is $R_{AB}/2$. For this value of Δ_y, σ_1 is nearly equal to 2π, which is not so different from the value given here.

Performing the time integration we find the first order transition amplitude as

$$c_{if}^{(1)} = \frac{1}{i\hbar}\,N_{if}^{(1)}\sqrt{\frac{\pi}{\eta}}\,\exp\left[-\frac{1}{2}\left(\frac{d\,\Delta k}{\sigma_1}\right)^2 - \frac{1}{2}\left(\frac{\Delta L}{\sigma_2}\right)^2\right]. \tag{3.36}$$

When we further approximate d by $R_1 + R_2$, Δk and ΔL reduces to the corresponding definitions of Brink,[7] and the exponent of $|c_{if}^{(1)}|^2$ agrees

with his expression.

We here add two remarks. Firstly we consider the case in which two nuclei form a di-nuclear system with a lifetime τ and an angular velocity Ω. As $R_{ab}(t) = d$ is constant and $\phi_0 = \Omega t$, $\phi_v = \pi/2$, we have

$$f_{if}^{(1)}(t) = N_{if}^{(1)} \exp\left[-(d\,\Delta k/\sigma_1)^2/2\right] \exp(-i\,\Omega\,\Delta L\,t). \tag{3.37}$$

The transition amplitude is given by

$$C_{if}^{(1)} = \frac{\tau}{i\hbar} N_{if}^{(1)} \exp\left[-(d\,\Delta k/\sigma_1)^2/2\right] C^{(1)}(x), \tag{3.38}$$

where

$$C^{(1)}(x) = \sin x / x \quad , \tag{3.39a}$$

$$x = \Delta L\,(\Omega\tau/2) \quad . \tag{3.39b}$$

The second case is concerned with the inelastic scattering caused by the macroscopic distortion of the nuclear potential.
The optical potential between two nuclei is assumed to have the Woods-Saxon shape with strength V_0, diffuseness a, and radius $R_1 + R_2$. We consider that the shape change is produced by allowing the surfaces $r = R_i (i = 1,2)$ to oscillate

$$\begin{pmatrix} \delta R_1 \\ \delta R_2 \end{pmatrix} = \sum_{lm} \begin{pmatrix} (-)^l a_{lm}^{(1)} R_1 \\ a_{lm}^{(2)} R_2 \end{pmatrix} Y_{lm}^{*}(\hat{R}_{AB}), \quad \hat{R}_{AB} = (\theta, \phi_0). \tag{3.40}$$

The Taylor expansion of the optical potential then gives to the lowest order in the deformation parameter $a_{lm}^{(i)}$ (i = 1, 2) an interaction term

$$f_{if}^{(1)} = (V_0/a) f_1(x) (\delta R_1 + \delta R_2), \tag{3.41}$$

where

$$f_1(x) = (d/dx)(1 + e^x)^{-1}, \quad x = (R_{AB} - R)/a. \tag{3.42}$$

We take the approximation that $\theta = \pi/2$ and put

$$f_1(x) \approx -e^{-x} \approx -e^{-\frac{|R_{AB}-d|}{a}} e^{-\frac{|d-R|}{a}} \tag{3.43}$$

Performing the time integration we find

$$c_{if}^{(1)} \propto \frac{1}{v} \exp\left[-\frac{1}{2}\left(\frac{\Delta L}{\sigma_2}\right)^2\right] Y_{lm}^*(\pi/2, 0), \tag{3.44}$$

where

$$\Delta L = m + d\, Q_{eff}/\hbar v, \quad \sigma_2^2 = d/a \approx R/a. \tag{3.45}$$

It should be noted that the Gaussian factor expressing momentum matching does not appear in $c_{if}^{(1)}$.

If the Lorentzian spread of each collective level with energy E_0 is taken into account, the transition amplitude acquires a resonance denominator[17]. We write $c \to \tilde{c}$ where

$$\tilde{C}^{(1)}_{if} = \frac{(\Gamma/2\pi)^{1/2}}{E^* - E_0 + i\,\Gamma/2}\, C^{(1)}_{if}(E^*) \qquad (3.46)$$

Here Γ is the width of the resonance and E^* is the excitation energy of the nucleus corresponding to the Q-value under consideration.

§4. Multistep transfer process

4.1 Binary-step approximation for the straight-line trajectory

We shall derive expressions for the transition amplitudes for the multistep transfer process when the relative motion of heavy ions can be approximated by a straight line near the point of closest approach.

The transition amplitude for the two-step sequential transfer via an intermediate state m is given by

$$C_{if}^{(2)} = (i\hbar)^{-2} \int_{-\infty}^{\infty} f_{mf}^{(1)}(t_2)\, dt_2 \int_{-\infty}^{t_2} f_{im}^{(1)}(t_1)\, dt_1 \,. \tag{4.1}$$

By use of the form factor given in eq. (3.31), we get

$$C_{if}^{(2)} = \frac{\sqrt{\pi}}{(i\hbar)^2} E(\sqrt{\mu_{12}}\, a_{12}) \prod_{i=1}^{2} \frac{N_i^{(1)}}{\sqrt{\eta_i}} \exp\left[-\frac{1}{2}\left(\frac{R\Delta k_i}{\sigma_{1i}} \right)^2 - \frac{1}{4} \frac{\omega_i^2}{\eta_i} \right]. \tag{4.2}$$

The second term in the exponent is equal to $(\Delta L_i/\sigma_{2i})^2/2$. The index i = 1 (2) denotes the first (second) step of the process. The function E(ix) is defined by

$$E(ix) = \int_{-\infty}^{ix} e^{-t^2} dt = \frac{\sqrt{\pi}}{2} \{ 1 + erf(ix) \}, \tag{4.3}$$

where[18]

$$erf(ix) = \frac{2i}{\sqrt{\pi}} \int_0^x e^{t^2} dt = \frac{2i}{\sqrt{\pi}} e^{x^2} F(x) \,. \tag{4.4}$$

Here Dawson's integral F(x) varies slowly with x as compared with $\exp(x^2)$. The argument of the function E contains

$$\mu_{12} = \frac{\eta_1 \eta_2}{\eta_1 + \eta_2} , \qquad a_{12} = \frac{i}{2}\left(\frac{\omega_1}{\eta_1} - \frac{\omega_2}{\eta_2}\right). \tag{4.5}$$

It should be noted that Dietrich[19] derived a similar expression for the sequential transfer amplitude in discussing nuclear Josephson effect. Time dependence of his form factor is similar to us, but his method has no relation to the matching of linear and angular momenta.

We also note that if the variation of Dawdon's integral with x can be neglected, the part containeing the imaginary part of E(ix) gives a Gaussian factor $\exp\{-(\omega_1+\omega_2)^2/4(\eta_1+\eta_2)\}$ instead of $\exp\{-\Sigma_{i=1}^{2}(\omega_i^2/4\eta_i)\}$. Thus we have the factor which corresponds to that of the one-step simultaneous transfer.

The transition amplitude of the three-step sequential transfer via intermediate states m and n can be written as

$$C_{if}^{(3)} = (i\hbar)^{-3} \int_{-\infty}^{\infty} f_{nf}^{(1)}(t_3)\, dt_3 \int_{-\infty}^{t_3} f_{mn}^{(1)}(t_2)\, dt_2 \int_{-\infty}^{t_2} f_{im}^{(1)}(t_1)\, dt_1$$

$$= (i\hbar)^{-3} \prod_{i=1}^{3} N_i^{(1)} \exp\left[-\frac{1}{2}\left(\frac{R\,\Delta k_i}{\sigma_{1i}}\right)^2 - \frac{\omega_i^2}{4\eta_i}\right]$$

$$\cdot \int_{-\infty}^{\infty} e^{-\eta_3 x_3^2}\, dx_3 \int_{-\infty}^{x_3 + a_{23}} e^{-\eta_2 x_2^2}\, dx_2 \int_{-\infty}^{x_2 + a_{12}} e^{-\eta_1 x_1^2}\, dx_1 , \tag{4.6}$$

where a_{12} is given by eq. (4.5), and

$$a_{23} = \frac{i}{2}\left(\frac{\omega_2}{\eta_2} - \frac{\omega_3}{\eta_3}\right), \tag{4.7a}$$

$$x_i = t_i + i\,\omega_i / 2\eta_i . \tag{4.7b}$$

We apply the following two transformations successively to the integral variables x_i:

$$(1)\quad \begin{cases} y_3 = (\eta_1 x_1 + \eta_2 x_2)/\eta_{12}, \\ y_4 = x_1 - x_2, \end{cases} \qquad \begin{cases} \eta_{12} = \eta_1 + \eta_2, \\ \mu_{12} = \eta_1 \eta_2 / \eta_{12}, \end{cases} \tag{4.8a}$$

$$(2)\quad \begin{cases} y_1 = (\eta_3 x_3 + \eta_{12} y_3)/\eta_{123}, \\ y_2 = y_3 - x_3, \end{cases} \qquad \begin{cases} \eta_{123} = \eta_1 + \eta_{12} \\ \qquad = \eta_1 + \eta_2 + \eta_3, \\ \mu_{12,3} = \eta_{12}\,\eta_3/\eta_{123}. \end{cases} \tag{4.8b}$$

The integral reduces to

$$(\pi/\eta_{123})^{1/2} \int_{-\infty}^{a_{12}} e^{-\mu_{12} y_4^2}\, dy_4 \int_{-\infty}^{a_{23} + \eta_1 y_4/\eta_{12}} e^{-\mu_{12,3} y_2^2}\, dy_2 . \tag{4.9}$$

We assume that y_4 appearing in the upper limit of the second integral can be replaced by a_1, at which $\exp(-\mu_{12} y_4^2)$ takes the maximum value. Then we can carry out the integration, yielding the result

$$C_{if}^{(3)} = \frac{\sqrt{\pi}}{(i t_k)^3} E(\sqrt{\mu_{12}}\, a_{12})\, E(\sqrt{\mu_{12,3}}\, a_{12,3}) \cdot \prod_{i=1}^{3} \frac{N_i^{(1)}}{\sqrt{\eta_i}} \exp\left[-\frac{1}{2}\left(\frac{R \Delta k_i}{\sigma_{1i}}\right)^2 - \frac{\omega_i^2}{4\eta_i} \right], \tag{4.10}$$

where

$$a_{12,3} = \frac{\eta_1}{\eta_{12}} a_{12} + a_{23}$$

$$= \frac{i}{2}\left(\frac{\omega_1 + \omega_2}{\eta_{12}} - \frac{\omega_3}{\eta_3} \right) . \qquad (4.11)$$

Thus in the present approximation we firstly take up the two-step process consisting of the first and second steps disregarding the third step. Secondly we regard these two steps as a simultaneous process by ignoring their time difference and consider the two-step process consisting of this simultaneous two-particle transfer and the third step. We can extend this approximation to a process with arbitrary number of steps. For example, in the case of a four-step process, we simply multiply eq. (4.10) by a factor corresponding to the two-step process which consists of the simultaneous three-nucleon transfer and the fourth step. We shall call this the binary-step approximation. In the sense that some of the time orderings are taken into account, we can regard this as an improvement over the independent one-step approximation, in which, for example, two integrals of eq. (4.1) are evaluated independently by replacing the second upper limit by $+\infty$.

4.2 Circular orbit

Let us briefly consider the case in which heavy ion follows a circular trajectory from $t = -\tau/2$ to $\tau/2$. The two-step transition amplitude is given by

$$C_{if}^{(2)} = \frac{(i\tau/2)\tau}{(ih)^2} \prod_{i=1}^{2} N_i^{(1)} \exp\left[-\frac{1}{2}\left(\frac{R\Delta k_i}{\sigma_{1i}} \right)^2 \right] C^{(2)}(\vartheta_1, \vartheta_2) .$$

(4.12)

Here

$$C^{(2)}(\vartheta_1, \vartheta_2) = \frac{1}{\vartheta_1}\left[\frac{\sin(\vartheta_1+\vartheta_2)}{\vartheta_1+\vartheta_2} - e^{i\vartheta_1}\frac{\sin\vartheta_2}{\vartheta_2}\right]$$

$$= \frac{1}{\vartheta_1}\left[C^{(1)}(\vartheta_1+\vartheta_2) - e^{i\vartheta_1}C^{(1)}(\vartheta_2)\right], \qquad (4.13)$$

in which the first term corresponds to the simultaneous transfer ignoring the time difference between the first and second steps, while the second term looks like the independent two-nucleon transfer. The imaginary part of $C^{(2)}(\theta_1,\theta_2)$ is exactly the amplitude of this process, but the magnitude is half of the latter. In general we have

$$C^{(n)}_{if} = \frac{\tau(i\tau/2)^{n-1}}{(ih)^n}\prod_{i=1}^{n} N_i^{(1)} \exp\left[-\frac{1}{2}\left(\frac{R\Delta k_i}{\sigma_{1i}}\right)^2\right] C^{(n)}(\vartheta_1, \vartheta_2, \cdots, \vartheta_n) \qquad (4.14)$$

The following recurrence relation holds for $C^{(n)}$

$$C^{(n)}(\vartheta_1, \vartheta_2, \cdots, \vartheta_n) = (\vartheta_1+\vartheta_2+\cdots+\vartheta_{n-1})^{-1}$$
$$\cdot\left[C^{(n-1)}(\vartheta_1, \vartheta_2, \cdots, \vartheta_{n-1}+\vartheta_n) - e^{i\vartheta_1}C^{(n-1)}(\vartheta_2, \vartheta_3, \cdots, \vartheta_n)\right], \qquad (4.15)$$

where

$$\vartheta_i = \Delta L_i\,(\Omega\tau/2) \qquad (4.16)$$

We see that in the right hand side of eq. (4.15) the time difference between the (n-1)-th and n-th steps is ignored in the first term but is included in the second term.

§5. Energy spectra

We shall discuss the energy spectra of outgoing particle in the case of straight-path trajectory in a crude way. From eq. (3.36) we see that the one-step transfer probability is large for the values λ_2 and Q_{eff} that satisfy the conditions $\Delta k = 0$ and $\Delta L = 0$. For a fixed value of λ_1, these optimum values are given by

$$\lambda_2^m = k_n \dot{R}_2 - (R_2/R_1)\lambda_1 , \tag{5.1a}$$

$$Q_{eff}^m = -m_n v^2/2 + (\hbar v/R_1)\lambda_1 . \tag{5.1b}$$

For the states whose values of λ_2 are near the λ_2^m, the condition $\Delta k = 0$ is approximately satisfied and ΔL depends linearly on $Q_{eff} - Q_{eff}^m$. The $\lambda_1 = 0$ component of $|c_{if}^{(1)}|^2$ is approximately proportional to

$$|C_{if}^{(1)}|^2 \propto \exp\left\{-(Q_{eff} - Q_{eff}^{opt})^2/W_0^2\right\}, \tag{5.2}$$

where

$$Q_{eff}^{opt} = -m_n v^2/2 , \tag{5.3a}$$

$$W_0 = \hbar v \sigma_2 / R . \tag{5.3b}$$

Due to the condition that $Y_{\ell_1\lambda_1}(\pi/2;0)$ is not zero, the λ_1 is varied from $-\ell_1$ to ℓ_1 in steps of 2, then each component of $|c_{if}^{(1)}|^2$ for a specific λ_1

shifts its center by $2\hbar v/R_1$ (see fig. 4). The shape of the spectrum obtained by summing up all the λ_1 components is dependent on the ratio of $2\hbar v/R_1$ to W_0, and may retain the Gaussian shape or may become flatter than that. The width is approximately given by

$$W = W_0 + \ell_1 \frac{\hbar v}{R_1} . \tag{5.4}$$

As shown in §4.1, the ΔL-dependent part of the two-step transition probability is given by

$$|C_{if}^{(2)}|^2 \propto \exp\left\{-\left(\frac{\omega_1^2}{2\eta_1} + \frac{\omega_2^2}{2\eta_2}\right)\right\}$$

$$+ \frac{4}{\pi} F(\sqrt{\mu_{12}}\, a_{12}) \exp\left\{-\frac{(\omega_1+\omega_2)^2}{2(\eta_1+\eta_2)}\right\} . \tag{5.5}$$

We can assume that the function F varies slowly with energy. Writing the relative kinetic energy and the intrinsic excitation energy of each step i = 1,2 as T_i and E_i^*, we have

$$E_{c.m.} = T_1 + E_1^* - Q_{gg}^{(1)} , \tag{5.6a}$$

$$T_1 = T_2 + E_2^* - Q_{gg}^{(2)} . \tag{5.6b}$$

We take the sum of $|c_{if}^{(2)}|^2$ over T_1 while fixing the energy T_2 of the outgoing particle. When λ_1 is zero for each step we have

$$\int |c_{if}^{(2)}|^2 dT_1 \propto \exp\left\{-(Q_{eff} - Q_{eff}^{opt})^2 / W_0^2\right\}, \tag{5.7}$$

where

$$Q_{eff}^{opt} = -\sum_{i=1}^{2} m_{ni} v_i^2/2 \quad , \tag{5.8a}$$

$$W_0^2 = \sum_{i=1}^{2} W_{0i}^2 \quad . \tag{5.8b}$$

and we have neglected the T_1 dependence of W_{02}. As in the one-nucleon transfer, the shape of the composite energy spectrum is dependent on the ratio $2\hbar v/(R_1 W_0)$. The width W takes the same expression as eq. (5.4) with ℓ_1 equal to the total angular momentum of two nucleons on the initial system. Thus although the first and second terms of eq. (5.5) depend on ω_i in a characteristic way of the independent-sequential and simultaneous transfer processes, respectively, both show the same kind of energy spectra.

It should be noted that for comparison with experimental data we have to multiply the probability distribution obtained here with the level densities of the intermediate and residual nuclei. It will be shown in the next chapter that their inclusion especially the spin dependence, plays an important role in fixing the shape of the energy spectrum.

§6. Discussions

We developed a method to describe the heavy-ion transfer reaction in a simple way. We followed Brink's argument as a physical guide and used the semiclassical theory of Broglia and Winther as a mathematical means. Brink's formula for one-nucleon transfer cross section was re-derived. Inelastic scattering and multinucleon transfer reactions can now be handled with this method for the straight-line or circular trajectory of relative motion.

For a rough estimate of the absolute magnitude of the cross section it will be convenient to use the Wigner limit for the radial wave function; $u(R) \sim (3/R^3)^{1/2}$. The angular distribution is determined by the product of the elastic scattering cross section $(d\sigma/d\Omega)_{el}$ and the factor due to the tail of bound-state wave function $\exp(-2\gamma_1 d)$, where d is the distance of closest approach dependent on the scattering angle. Because of the absorptive reduction of $(d\sigma/d\Omega)_{el}$ at small d and the damping of the transfer probability at large d, the angular distribution can be expected to have a dumb-bell shape centered at the grazing angle. The energy spectrum is given by the product of the transfer cross section and the level density of the residual nucleus, summed over irrelevant quantum numbers. The level density may affect the optimum Q-value and the width of the spectrum.

Finaly we shall point out a possibility to view the multinucleon transfer as a stochastic process. The transition probability of a n-step process from the state i to f is given by

$$P_{if}^{(n)} = \sum_{\{m,\cdots,l\}} |C_{im\cdots lf}^{(n)}|^2 \rho_m \cdots \rho_l , \qquad (6.1)$$

where m,···, 1 denote intermediate states and ρ is the corresponding level density. For the straight-line trajectory we have

$$P_{if}^{(n)} = \sum_{\ell} P_{i\ell}^{(n-1)} Q_{\ell f} \quad , \tag{6.2}$$

where

$$Q_{\ell f} = \left(\frac{N_n^{(1)}}{t\sqrt{\eta_n}} \right)^2 \exp\left[- \left(\frac{R \Delta k_{1n}}{\sigma_{1n}} \right)^2 - \frac{\omega_n^2}{2\eta_n} \right] E^2\left(\sqrt{\mu_{1\cdots n-1,n}}\, a_{1\cdots n-1,n} \right) \rho_\ell \,. \tag{6.3}$$

We take η_n to be independent of n, and assume that the (n-1)-step part proceedsvia the optimum path as a whole; that is, we take $\Sigma_{i=1}^{n-1}\omega_i = 0$ in the function E. Then for large n we have

$$\mu_{1\cdots n-1,n} = \eta_n \sum_{i=1}^{n-1} \eta_i \Big/ \sum_{i=1}^{n} \eta_i \approx \eta_n \quad , \tag{6.4}$$

$$a_{1\cdots n-1,n} = -\frac{i}{2}\left(\frac{\omega_n}{\eta_n} - \frac{\sum_{i=1}^{n-1} \omega_i}{\sum_{i=1}^{n-1} \eta_i} \right) \approx -\frac{i\,\omega_n}{2\eta_n} \,. \tag{6.5}$$

As Q_{lf} is dependent only on the quantities related to the final n-th step, eq. (6.2) reduces to the Smoluchowski equation. Thus we are lead to a possibility to treat the multinucleon transfer as a Markov process. But our treatment is restricted to a peripheral collision, while for the multinucleon transfer process we can expect the contribution from the overlapping region of two nuclei to be important. It should be noted that

Feshbach et al.[20] showed the possibility that a suitably redefined transfer probability satisfies the diffusion equation when the multistep direct reaction is treated statistically.

Chapter III. Comparison with experiment

§1. Introduction

In chapter II, we developed a semiclassical theory of heavy-ion transfer reactions which incorporates the matching conditions of the linear momentum of transferred particle and total angular momentum as originally proposed by Brink.[7,15] We here intend to report the results obtained by analyzing with this model gross properties of transfer reactions such as energy spectra, angular distributions and polarizations of outgoing particles.

For that purpose we take the products of DWBA cross sections with the level densities of the final and intermediate states (for the two-step process) and sum them over irrelevant quantum numbers. Explicit procedures and parametrizations of the level density are given in sect. 2. In sect. 3 we treat one-nucleon transfer reactions on ^{53}Cr, ^{96}Mo, ^{181}Ta and ^{208}Pb targets. The approximation of a circular trajectory is applied on the ^{100}Mo(^{14}N, ^{12}B) reaction in sect. 4, assuming the simultaneous or sequential transfer of two nucleons. We include the effect of friction at high incident energies. One and two alpha-particle transfer reactions on ^{40}Ca and ^{27}Al targets are analyzed in sect. 5. In sect. 6, the ^{197}Au(^{19}F, ^{12}B) reaction is treated as a one-step process. In sect. 7, some discussions will be made.

§ 2. General considerations on the energy spectra and choice of parameters

We consider a reaction

$$A + b \rightarrow a + B . \tag{2.1}$$

In the one-step process in which one particle n is transferred from the projectile A to the target nucleus b, the energy spectrum can be written as

$$\sigma^{(1)}(E_f, \theta) = (\hat{I}_A\ \hat{I}_b)^{-2} \sum_{\{\ell\lambda\}} \sigma^{(1)}_{\{\ell\lambda\}}(E_f, E_i, \theta) \rho_{\ell_2}(E_i - E_f) , \tag{2.2}$$

The cross section for the scattering of outgoing particle a in the θ direction is denoted as $\sigma^{(1)}_{\{\ell\lambda\}}(E_f, E_i, \theta)$. Here E_i and E_f are the kinetic energies in the initial and final channel. In the semiclassical theory, the cross section is written as the product of the elastic scattering cross section and the transition probability

$$\sigma^{(1)}_{\{\ell\lambda\}}(E_f, E_i, \theta) = \sigma_{el}(\theta) \cdot \left| C^{(1)}_{\{\ell\lambda\}} \right|^2 . \tag{2.3}$$

For the sequential transfer process, we assume that the particles are transferred firstly from the state characterized by $(\ell_1\lambda_1)$ to the $(\ell_2\lambda_2)$ state, and secondly from the $(\ell_1'\lambda_1')$ state to the $(\ell_2'\lambda_2')$ state. The corresponding energy spectrum is given by

$$\sigma^{(2)}(E_f, \theta) = (\hat{I}_A\ \hat{I}_b)^{-2} \sum_{\{\ell\lambda\}} \int dE_m\, \sigma^{(2)}_{\{\ell\lambda\}}(E_f, E_m, E_i, \theta) \rho_{\ell_2}(E_i - E_m) \rho_{\ell_2'}(E_m - E_f) , \tag{2.4}$$

where $\{\ell\lambda\}$ denotes $\ell_1\lambda_1$, $\ell_2\lambda_2$, $\ell_1'\lambda_1'$ and $\ell_2'\lambda_2'$ collectively, and E_m is the channel energy in the intermediate stage. The two-step cross section $\sigma^{(2)}_{\{\ell\lambda\}}$ is given by the product of $\sigma_{el}(\theta)$ and the two-step transition probability $|c^{(2)}_{\{\ell\lambda\}}|^2$ as in eq. (2.3).

In the direct n-particle transfer, the acceptor nucleus is expected to be excited to n-particle 0-hole states as doorway states, for which the following level density formula derived from Ericson's model[21] is adequate

$$\rho_{\ell_2}(E^*) = \rho_0 \frac{(\rho_0 E^*)^{n-1}}{n!(n-1)!} \cdot \frac{(2\ell_2+1)}{\sqrt{8\pi}\,\sigma^3} \exp\left\{-\frac{1}{2}\ell_2(\ell_2+1)/\sigma^2\right\} . \quad (2.5)$$

The spin dependence is taken to have the standard Gaussian form. The level density of one-particle excited states is denoted as ρ_0 which we take to be independent of the excitation energy E*,

$$\rho_0 = \frac{6}{\pi^2}a , \qquad a = \frac{A}{10} \quad (2.6)$$

where A is the mass number. In the Fermi gas model ρ_0 is proportional to $(E^* + E_F)^{1/2}$, where E_F is the Fermi energy. For single-particle transfer reactions peak position of the energy spectrum calculated by use of this ρ_0 shifts to somewhat higher excitation energy as compared with the case of E^*-independent ρ_0. The spin-cutoff parameter can be written as

$$\sigma^2 = \mathcal{J}\,T/\hbar^2 , \quad (2.7)$$

where $\mathcal{J}$ is the moment of inertia of the transferred particle around the target nucleus and T is the nuclear temperature. The spin-cutoff can also be expressed as

$$\sigma^2 = c\langle m^2\rangle , \quad (2.8)$$

in which c is given by n or n^2, dependent on whether n particles are excited independently or fully correlated. The mean square of z components of angular momenta of one-particle states is given by[22]

$$\langle m^2\rangle = 0.146A^{2/3} . \quad (2.9)$$

Spectroscopic factors for the residual nucleus are assumed to be a constant which is independent of E^* and ℓ_2.

The choice of the level density formula affects strongly the energy spectrum. We show in fig. 5 the effects of varying the level density formulas,

eq.(2.5) and the statistical form exp (E^*/T) in addition to the transfer probability. We treat the $^{40}Ca(^{20}Ne, ^{16}O)^{44}Ti$ reaction at the incident energy of 262MeV. In the case of constant $\rho_{\ell_2}(E^*)$, the energy spectrum is obtained by summing over $\lambda_1 (-\ell_1 \leq \lambda_1 \leq \ell_1,\ \ell_1+\lambda_1 = \text{even})$ the components with comparable magnitudes and having maxima at $Q^m_{eff}(\lambda_1)$ given by

$$Q^m_{eff}(\lambda_1) = -\frac{1}{2}m_n v^2 + (\hbar v/R_1)\lambda_1 \quad . \tag{2.10}$$

This result is shown in the top graph of fig. 5.

In the middle of the figure are shown the results obtained by use of the statistical level density exp(E*/T). As $\rho(E^*)$ increases rapidly with E* for low T, the component with $\lambda_1 = -\ell_1$ becomes dominant and the composite spectrum has its maximum at high E*. On the other hand, strong spin dependence of the level density, eq. (2.5), for low T makes contributions of small ℓ_2 and λ_2 dominant. Due to the matching condition of linear momentum, eq. (3.35a) of chapter II, small λ_2 means $\lambda_1 \sim \ell_1$ and the energy of the maximum cross section shifts to low E* region. This situation can be seen from the lowest part of fig. 5. Not only the peak position but the width of the spectrum is affected by the choice of the level density formula.

Siemens et al.[16] found that the experimental optimum Q-values of reactions on ^{232}Th induced by 130 MeV ^{15}N and 120 MeV ^{16}O can be explained by a semiclassical argument similar to ref. 7 if we take into account the nuclear attraction V_N equal to 28MeV. In the following we also include V_N as one of parameters in calculating local velocities or momenta. The optimum Q_{eff} value for $\lambda_1 = 0$ with inclusion of V_N is given by

$$Q^m_{eff} = Q^m_{eff}(V_N = 0) + \frac{m_n}{\mu}V_N \ , \tag{2.11}$$

where μ is the reduced mass of relative motion of heavy ions. Then we can

expect that the peak energy of the energy spectrum changes linearly with V_N and the shift is much smaller than that of V_N itself as long as $m_n \ll \mu$. This result was borne out by the numerical calculations.

The widths σ_1 and σ_2 of the Gaussian factors expressing the matching effects of linear and angular momenta are taken to be [23]

$$\sigma_1 \approx \pi , \qquad \sigma_2 \approx (\gamma_1 R)^{1/2} . \tag{2.12}$$

Use of σ_1 gives in eq. (3.19) of chapter II does not give any noticeable changes in the calculated results. In calculating R_1 and R_2, the radius parameter $r_0 = 1.4$ fm is used.

Level density parameters and V_N used in the calculations are summarized in table 1.

In the figures here, E* in the abscissa means the sum of excitation energies of both final products. The calculated energy spectra are normalized to the experimental data.

In the calculations we use both the straight-line and circular trajectories. The former was originally used by Brink,[15] while the latter was proposed in chapter II The circular trajectory calculation includes the rotation angle θ as one of the parameters. Which approximation describes the orbital motion adequately is a problem which can not be settled from the classical deflection function because of the effects of diffraction, absorption and transferred nucleons.

§3. One-nucleon transfer reactions

In this section we shall study the following four kinds of one-nucleon transfer reactions

$^{53}Cr(^{14}N, ^{13}C)$ at 90 MeV,[24,25]

$^{96}Mo(^{14}N, ^{15}O)$ at 97 MeV,[24,25]

$^{181}Ta(^{16}O, ^{17}O)$ at 96 MeV,[26]

$^{208}Pb(^{16}O, ^{15}N)$ at 312.6 MeV.[27]

Comparisons of experimental data with calculations are shown in figs. 6∿9. As the residual nucleus has constant level density and low optimum excitation energy in the case of one-nucleon transfer, the calculated cross section does not tend to vanish at zero excitation energy. Discontinuous changes can be seen in the energy spectra, which is especially large for the $^{208}Pb(^{16}O, ^{15}N)$ reaction. This reflects the onset of a new excited state in the ejectile. For example, the $(^{16}O, ^{15}N)$ reaction takes place by transferring $p_{1/2}$ and $p_{3/2}$ nucleon for the transitions to the $1/2^-$ ground state and $3/2^-$ 6.324MeV excited state, respectively. In treating the $(^{14}N, ^{15}O)$ reaction, only the transition to the stable ground state of ^{15}O is taken into account, so that no kinks appear. Spectroscopic factors for light nuclei are taken from Cohen and Kurath.[28]

Yoshie and Kohno[25] showed that the relative strengths of one-nucleon transfer reactions on ^{92}Mo leading to low lying excited states of residual nuclei do not agree so well with the prediction of Brink[7] for the ^{12}C projectile, but agree well for the ^{14}N projectile. The region of excitation energies in which the energy spectra can be explained by the present model seems to be restricted to low excitation energy similarly as their analysis. Our model can not predict the second peak around $E^* \sim 10$MeV in the $^{96}Mo(^{14}N, ^{15}O)$ reaction and the broad spectra at high excitation energy region

(not shown in fig. 9) in the $^{208}Pb(^{16}O, ^{15}N)$ reaction.

Similar results can be obtained by using the circular trajectory with $\theta = 1.0$. This value is considerably larger than those of other transfer reactions, and seems to contradict with the physical intuition that as the number of transferred nucleons decreases, the reaction takes place at the outer region of the nucleus. Thus one-nucleon transfer reaction may be more adequately described by use of the straight-path trajectory.

In the above calculations we took V_N to be 28 MeV. Fig. 10 shows the effect of varying V_N on the $^{53}Cr(^{14}N, ^{13}C)^{54}Mn$ reaction. Some minor changes in the shapes of energy spectra can be seen.

§4. Two-nucleon transfer reaction : $^{100}Mo(^{14}N, ^{12}B)$

Sugimoto et al.[11,12] measured the energy spectra and polarizations of ^{12}B emitted from the bombardment of ^{14}N on ^{100}Mo at incident energies of 90, 125 and 200 MeV. Results of our analysis under the assumption of one-step process with straight-path trajectory were reported previously.[10] DWBA calculations yielded similar results.[1] Two-particle spectroscopic factors for $^{14}N \rightarrow {}^{12}B$ were taken from Cohen and Kurath,[29] and ℓ_1 was assumed to be 2.

For the transitions leading to discrete levels of residual nucleus, DWBA calculations were performed by taking into account both simultaneous and sequential processes.[30,31] The latter was shown to contribute comparably with or even dominate over the former, and some discussions were done for the similarity of predictions of both processes. As we do not have as yet corresponding calculations for the continuum region, we here enumerate the results of one- and two-step processes and try to find out the difference between them, if any, from the results. We firstly show in fig. 11 the results obtained by assuming sequential transfer with straight-path trajectory. Real part of the transition amplitude corresponds to the process in which two successive transfer events occur independently of each other. This part has comparable cross sections and similar polarizations as the imaginary part. Calculations shown in the figure make use of $V_N = 28$ MeV, but if we set $V_N = 0$, excitation energies of the maximum cross section and zero polarization become lower by about 5 MeV.

To see the validity of straight-line trajectory we calculated the classical deflection function of the $^{100}Mo(^{14}N, ^{12}B)$ reaction at 90 MeV. For each set of the orbital angular momentum ℓ_i of the initial channel and the excitation energy E* of the final channel, a classical orbit is determined so that the turning points of both channels coincide. The optical model

parameters are[25]

$$V = -80 \text{ MeV}, \quad r_0 = 1.174 \text{ fm}, \quad a = 0.5 \text{ fm}.$$
$$W = -25 \text{ MeV}, \quad r_C = 1.2 \text{ fm} \tag{4.1}$$

As shown in fig.12 the rainbow angle is about 28°(in lab. system) while the observation angle θ_{lab} is 20°. For the orbital angular momenta ℓ_i in the incident channel contributing to the transfer process the orbit may be bent by the nuclear attraction and so can be approximated by a circle near the closest distance of approach. Thus it is worthwhile to pay attention to the calculations of circular trajectory.

Both for the one- and two-step processes we have studied the effects of variations of the nuclear temperature T and the rotation angle θ on the $^{100}Mo(^{14}N, ^{12}B)$ reaction at 90 MeV. Firstly, one-step results are shown in figs. 13∿15. As θ becomes larger, the contact time of two nuclei increases and so the transition probability. At the same time, as $\Delta L \tilde{\gtrsim} 0$ condition becomes more restrictive, the width of energy spectrum becomes more narrow and the polarization more positive. Reflecting the appearance of $\sin(\Delta L \cdot \theta/2)$ in eq.(3.39a) of chapter II, the polarization begins to oscillate with E^*. These situations can be seen in fig. 13.

Effects of varying the temperature T are shown in figs. 14 and 15 for θ = 0.4 and 0.5, respectively. There are some differences between the results for θ = 0.4 and 0.5. The density of levels with large ℓ_2 increases rapidly with increasing T. It shifts E* of the maximum cross section to larger value. Near the maximum the transfer probability with $\lambda_1 = -2$ becomes dominant, corresponding to positive polarization. It should be noted that for large θ we have negative angle scattering, for which the sign of the calculated polarization must be reversed.

Figs. 16 and 17 show the corresponding results for the sequential transfer process. Here we have assumed that the reaction proceeds via the ground state of ^{13}C. General trends of dependences on T and θ are similar to those of the one-step process in line with the arguments of ref. 30. But the oscillation of the polarization at large rotation angles now dissapears and the θ, T dependence of the energy spectra is larger than the one-step case.

Comparisons of calculations with experimental data at 90 MeV are shown in fig. 18. When we take the one-step picture the calculation performed with V_N = 28 MeV, T = 5 MeV and θ = 0.7 reproduces the data. On the other hand, the two-step calculation done by using V_N = 0, T = 5 MeV and θ = 0.4 gives flattened shape for the polarization with respect to E* as compared with the results of straight-line trajectory, thus bringing about better agreement with the data at large E*. From these comparisons, however, it is difficult to conclude which process describes the reaction more adequately. For that purpose, careful analysis of angular distributions and absolute cross sections will have to be supplemented.

For incident energies of 125 and 200 MeV, experimental energy spectra have maxima at 40∿50 and 80 MeV excitation energies, respectively, and their widths are very large, while the behavior of the polarization as a function of the Q-value is pretty independent of the incident energy. As shown in figs. 19 and 20, the maxima of calculated spectra are at E* = 15 and 20 MeV, respectively, and the widths are narrow. Polarizations are zero at E* $\approx$ 50 and 80 MeV in contrast with the experimental situation.

In order to remedy this situation, we tried to take into account the effect of friction, approximately following the line of Alhassid et al.[32] The friction force is proportional to the velocity, so its effect may

be important at high incident energies. For grazing collision the rate of loss of tangential kinetic energy due to friction is

$$dE/dt = \mu v(dv/dt) = -\gamma v^2 = -(2\gamma/\mu)E \tag{4.2}$$

where γ is the coefficient of friction. The duration t of transfer is assumed to be proportional to the number of nucleons; $t = nt_0$. Then the fractional loss of energy is given by

$$\exp[-2\gamma(t/\mu)] = \exp[-\alpha(n/\mu)] \tag{4.3}$$

in which $\alpha = 2\gamma t_0$. We assume that after the incident energy is reduced by the friction, the transfer takes place, and then the ejectile is affected again by the friction. Results obtained by including the effect of friction are shown in the figures as dashed and dotted curves for the straight-line and circular trajectories, respectively. Energies of maximum cross sections become large but those of the zero polarization are affected in the same way. Anyway we cannot reproduce observed attenuation of polarizations at large E*.

§5. Alpha-particle transfer reactions

Fröhlich et al.[3,33] investigated three kinds of α-particle transfer reactions (^{20}Ne, ^{16}O), (^{14}N, ^{10}B) and (^{13}C, ^{9}Be) on a ^{40}Ca target at incident energies of 262, 153 and 149 MeV, respectively. The orbital angular momentum ℓ_1 of α-particle in ^{20}Ne, ^{14}N and ^{13}C was chosen to be 0, 4 and 2, respectively. The (^{14}N, ^{10}B) and (^{13}C, ^{9}Be) reactions were fitted well by assuming α-transfer but the DWBA cross section of the (^{20}Ne, ^{16}O) reaction concentrated near 80 MeV excitation energy in ^{44}Ti, which is much higher than the experimental peak position of E*∿54 MeV, corresponding to the final laboratory energy E_{lab} of 175 MeV and 200 MeV, respectively. The difference was attributed to projectile breakup and breakup-fusion processess.[13] They used the spectroscopic density as given by

$$\rho_S(E^*, \ell) = (E^*/T)^2(\ell/\sigma)^2\exp[(E^*/T) - (\ell/\sigma)^2] \qquad (5.1)$$

in which the ℓ dependent factor is derived from the strength of the scattering wave functions of α-particle, and T = 60 MeV and σ = 11.

Our calculated results are shown in fig. 21. When we take $\ell_1 = 0$ for (^{20}Ne, ^{16}O) we can fit the energy of maximum cross section but the calculated width is about one half of the experimental one, as shown in fig. 21 by a dotted line. We can get much better agreement if we sum up the transitions to the ground state, 6.13 MeV 1^- and 7.12 MeV 3^- states of ^{16}O which have large strength for the transition $^{20}\text{Ne} \to {}^{16}\text{O}^* + \alpha$. The α-particle spectroscopic factors are taken from refs. 34 and 35. In the other reactions with $\ell_1 = 4$ and 2 for the ground state transitions, the effects of inclusion of other ℓ_1 components on the energy spectra are small. For large scattering angles, however, our calculations predict only a small portion of the (^{20}Ne, ^{16}O) energy spectra, centering at E_{lab} = 190 MeV.

Calculations using the spectroscopic density of eq. (5.1) give the optimum E* = 60, 68 and 68 MeV (E_{lab} = 195, 66 and 65 MeV) for (^{20}Ne, ^{16}O), (^{14}N, ^{10}B) and (^{13}C, ^{9}Be), respectively. Influence of the level density on the latter two reactions is stronger than (^{20}Ne, ^{16}O), due to their low incident energies and the difference of the orbital angular momentum ℓ_1. Eq. (5.1) makes use of a large value of T so that it is very similar to eq. (2.5) with T = 20 MeV. The change of optimum E^* according to the choice of two level density formulas is essentially what we can expect from the bottom of fig. 5.

We can make simple argument on the optimum Q-value of the breakup (-fusion) process. Suppose that the projectile A breaks up into a and n, and a is detected as the ejectile. The Q_{eff} value is then given by $\frac{1}{2}av^2 - \frac{1}{2}Av^2 = -\frac{1}{2}nv^2$. This is equal to the optimum Q_{eff} of the transfer reaction in which n is captured in the continuum state of the target b. If the Coulomb interaction of the ejectile a with other particles are assumed to depend on the distance from a to the c.m. of b and n, the optimum Q-value of the breakup process agrees with that of the transfer process. It also coincides with the optimum Q-value of the breakup-fusion process. For the breakup (-fusion) process we need not to multiply the cross section by the level density of residual nucleus. Thus the breakup (-fusion) energy spectra have the maximum at the optimum Q-value as given by Brink.[7]

As in sect. 4 we have performed the calculations by using the circular trajectory. The classical deflection functions are calculated from the optical potential parameters[33]

$$\begin{aligned} &V = -100 \text{ MeV}, \quad r_{0R} = 1.10 \text{ fm}, \quad a_R = 0.634 \text{ fm}, \\ &W = -24 \text{ MeV}, \quad r_{0I} = 1.24 \text{ fm}, \quad a_I = 0.507 \text{ fm}, \\ &\qquad\qquad r_{0C} = 1.25 \text{ fm}. \end{aligned} \tag{5.2}$$

As shown in fig. 22, the projectile's orbit is deflected from the Rutherford trajectory by the nuclear attraction. The energy of the maximum cross section is affected by the choice of rotation angle θ and becomes large for small θ.

With $\theta \gtrsim 1.0$ rad., we get results very similar to those of straight-line trajectory for both densities of eqs. (2.5) and (5.1). The results obtained by using our level density, eq. (2.5), and $\theta = 0.4$ are shown in fig. 22. If we use $\theta = 0.17$ for (^{20}Ne, ^{16}O) we obtain the energy spectra similar to ref. 3. These choices of θ differently taken for three α-particle transfer reactions give agreements with experimental data at large scattering angles, as can be seen from fig. 23. If we use the spectroscopic density, eq. (5.1), and $\theta = 0.4$, the optimum E^* is 80 MeV for (^{20}Ne, ^{16}O), thus giving agreement with that of ref. 3. However, (^{14}N, ^{10}B) and (^{13}C, ^{9}Be) have the optimum E^* of 78 MeV (E_{lab} = 57 and 55 MeV, respectively).

Fig. 24 shows the effect of varying V_N on the energy spectra of the ^{40}Ca(^{20}Ne, ^{16}O)^{44}Ti reaction at 262 MeV incident energy. We assumed $\ell_1 = 0$ for simplicity and straight-line trajectory. The optimum energy varies according to V_N but the shift is much smaller than the change of V_N itself.

Nextly we consider the angular distribution. The elastic cross section $\sigma_{el}(\theta)$ can be evaluated in a semiclassical way by utilizing the classical deflection function.[36] The imaginary part of the optical potential is assumed to affect the attenuation of the elastic wave. The results of the straight-line trajectory are compared with experimental data in fig. 25. At large angles, the calculated cross sections are due to the scattering into negative angles. The forward cross sections of (^{20}Ne, ^{16}O) and (^{14}N, ^{10}B) get some contributions from the rainbow-angle scattering.

In the evaluation of absolute magnitudes of cross sections we assume that extensions Δ_i(i=x,y,z) of the region between two nuclei and effective for the transfer are all equal. The strength of the potential between the α-particle and the ejectile is taken to be 20 MeV; 1/5 of the depth given in eq. (5.2). Then the absolute magnitudes of three α-particle transfer reactions can be fitted by taking the average α-spectroscopic factor of ^{44}Ti* to be about 0.04.

Now we consider the (^{20}Ne, ^{16}O) and (^{20}Ne, ^{12}C) reactions induced by 120 MeV ^{20}Ne impinging upon ^{27}Al.[37] In the analysis of Udagawa et al.[4] the spectroscopic density was taken to have the form exp(E*/T) and $\mathcal{J}$, T were regarded as parameters. The (^{20}Ne, ^{12}C) reaction was assumed to proceed by transferring two α-particles sequentially, and populating only the ground state of ^{12}C. We have used the same assumptions on the reaction mechanism. The results of the straight-line trajectory are shown in fig. 26. One-step α-transfer to the ^{16}O ground state has narrow energy spectrum as shown in the figure by a dotted curve. So we have included three states of ^{16}O as in the ^{40}Ca(^{20}Ne, ^{16}O) reaction. On the other hand, the spectrum of two-step α-transfer is not affected by the choice of intermediate ^{16}O states. The nuclear temperature is chosen to be 10 MeV. For larger value of T, e.g., 20 MeV, we can get better fit to the (^{20}Ne, ^{12}C) reaction. If the (^{20}Ne, ^{12}C) reaction is assumed to be one-step ^{8}Be transfer process, the peak of the energy spectrum shifts to E* still larger than that shown in fig. 26.

On the other hand we could obtain rather good agreements with experiment and with Udagawa et al.[4] if we use the circular trajectory. The results with $\theta = 0.6$, $T = 6$ MeV and $V_N = 10$ MeV are also shown in fig. 26. In the present case we have introduced the Coulomb reduction factor

$$N_c = \exp\left[5.5\left(1 - \sqrt{31/E_f}\right)\right] \qquad (5.3)$$

for $E_f \leq 31$ MeV, as in ref. 4. With the level density exp (E*/T), the results of Udagawa et al. can be reproduced in the circular trajectory approximation by taking $\theta = 0.6$, $T = 20$ MeV and $V_N = 16$ MeV.

§6. Seven-nucleon transfer reaction : $^{197}Au(^{19}F, ^{12}B)$

In this brief section we discuss the energy spectrum and polarization of ^{12}B emitted from the $^{197}Au(^{19}F, ^{12}B)$ reaction at 186 MeV incident energy. The experiment was carried out by Ishihara et al.[2] and was analyzed by the one-step mechanism, assuming the same form for the spectroscopic density as eq. (2.5) with T = 10 MeV.

The mechanism of seven-nucleon transfer reaction can be much complicated. But here we follow the same assumption as Ishihara et al., for simplicity. Calculated results are compared with experimental data in fig. 27 for both cases of straight-line and circular trajectories. It is seen that for the latter trajectory the $\theta = 0.55$ polarization shows pretty different behavior from the $\theta = 0.35$ result. The former oscillates with E* at large E*, thus gives better agreement with the experimental polarization data, but becomes worse for the energy spectrum. When we use the value of σ_1 defined in chapter II the polarization rises with E* more gradually, and the $\theta = 0.35$ result is pretty similar to ref. 2. In the latter, calculated polarization did not show oscillation with E*.

§7. Discussions

We analyzed some of gross properties of transfer reactions with the semiclassical model developed in chapter II. Calculated energy spectra of one-nucleon transfer reactions reprocuce well the experimental data for low excitation energy region. For high excitation energy retion the agreement is not well, especially at high incident energy.

For the reaction ^{100}Mo (^{14}N, ^{12}B) at 90 MeV incident energy, we made calculations for the energy spectra and the spin polarization of ^{12}B. Results of the two-step process with straight-path trajectory show nearly the same trend as the results of the one-step calculation which we have made previonsly. The calculation of two-step process with circular trajectory explain the trend of the experimental data of polarization for high energy excitation region. We can also reproduce the experiment of ^{197}Au (^{19}F, ^{12}B) at an incident energy of 186 MeV by the calculation of one-step process with circular trajectory. On the other hand, at higher incident energies of the reaction ^{100}Mo (^{14}N,^{12}B), we can not describe the experimental data both for energy spectra and for polarization. The situation is not improved by the inclusion of the effect of friction.

We also calculated the alpha-particle transfer reactions (^{20}Ne,^{16}O), (^{14}N,^{10}B) and (^{13}C,^{9}Be) on a ^{40}Ca target. Results of one-step process for straight-path trajectory can explain the energy peak of the data at forward angles. They can also give comparable energy widths with the experiments. Energy spectra of (^{20}Ne,^{16}O) in high excitation energy region can not be reproduced by the calculation from straight-path trajectory.

The exact-finite-range DWBA calculation for transfer process by Frölich et al.[3] has given the broad energy spectra. The peak position is near the excitation energy $E^* \sim 80$ MeV, different from the experimental value of $E^* \sim 54$ MeV. Udagawa and Tamura attributed the difference to breakup and

breakup-fusion processes which have a peak of $E^* \sim 50$ MeV.[13] We made a calculation, using the same functional form of level density as they used. Our peak position by the straight-path trajectory is $E^* \sim 55$ MeV, much lower than their value $E^* \sim 80$ MeV of transfer process. Reproduction of their energy spectrum is possible if we use the circular trajectory with a much smaller rotation angle than the ones for the other two reactions. When we neglect the effect of level dinsity, the optimum Q-value for breakup process will agree with the value calculated from the matching conditions of Brink.[7] So the energy spectrum of (^{20}Ne,^{16}O) in the high excitation energy region can be the contribution of higher order processes such as inelastic breakup, than the transfer process.

Using the classical deflection functions, we also analyzed the angular distributions for these alpha-transfer reactions. Magnitudes of these three reactions are explained by nearly equal spectroscopic factors. At backward angles the contribution is mainly from tne scattering of opposite side of the nucleus.

We also calculated the reactions (^{20}Ne,^{16}O) and (^{20}Ne,^{12}C) at 120 MeV incident energy on a ^{27}Al target. The (^{20}Ne,^{12}C) reaction was assumed to be a two-step alpha-transfer process. We could not fit these reactions with common parameters. If the Coulomb reduction factor which Udagawa et al.[4] have intriduced is taken into account, we can reproduce their results.

Chapter IV. Summary and duscussions

In chapter II we developed a semiclassical method to describe the heavy ion transfer reactions in a simple way, using the theory of Broglia and Winther. Brink's formula for one-nucleon transfer cross section was re-derived. Inelastic scattering and multinucleon transfer reaction can also be treated for the straight-line or circular trajectory of ralative motion.

In chapter III we analyzed a variety of experimental data involving transfer of up to eight nucleons. Values of $\hbar T/\langle m^2 \rangle$ used in the calculation are larger than 1 for one-nucleon transfer, and very close to n and n^2 for (^{14}N, ^{12}B) and alpha transfer, respectively, while it is intermediate between n and n^2 for (^{19}F, ^{12}B).

Calculated energy spectra of one-nucleon transfer reactions were shown not to vanish at zero excitation energy of final products. In the case of $^{208}Pb(^{16}O, ^{15}N)$ at 312.6 MeV incident energy the direct reaction theory explains only a limited region of the energy spectra but not the main body. For the α transfer on ^{40}Ca our results agree with the experimental energy spectra at forward direction but predicts a small portion of the latter at larger angles. Reproduction of such a broad energy spectrum as observed in the $^{40}Ca(^{20}Ne, ^{16}O)^{44}Ti$ reaction at large angles is possible if we use the circular trajectory and the level density of ref. 33, but take a different rotation angle from those of (^{14}N, ^{10}B) and (^{13}C, ^{9}Be). Udagawa and Tamura's group[13] regarded the experimental spectrum as the sum of this broad bump and a narrow distribution with the maximum at excitation energy much smaller than that of the former, and explained them as due to the transfer and breakup (-fusion) mechanism, respectively. Importance of breakup process at high incident energy was also pointed out by other people (e.g., refs. 38,39). High excitation of the projectile sufficient to evaporate light particles subsequent to the collision

is needed for the explaination of the observed yield of emitted light particles. In order to account for the energy spectra and to decide which part of it, high E* or low E*, is contributed by the breakup process, inelastic excitation mechanism must be supplemented to the standard DWBA theory of the breakup process.

Angular distributions of three kinds of α-transfer reactions on ^{40}Ca target have been analyzed in a semiclassical way. Gradual decrease of cross sections with angles can be understood by the scattering into negative deflection angles. Angular distributions should be treated more satisfactorily by extending the semiquantal model of transfer reactions such as developed by Hasan and Brink.[40] Fits to experimental absolute magnitudes of cross sections extracted the average spectroscopic factor of about 0.04 for $^{44}Ti^* \rightarrow {}^{40}Ca + \alpha$.

Polarizations of the outgoing ^{12}B in the $^{100}Mo(^{14}N, {}^{12}B)$ and $^{197}Au(^{19}F, {}^{12}B)$ reactions have been treated. We especially concentrated on the model in which the incident ion is assumed to roll around the target nucleus for a short time interval and studied the effects of varying parameters in some detail. By use of this circular trajectory we could obtain agreement between theory and experiment, better than the case of straight-line trajectory. At high incident energies, however, we have found big dissagreements which can not be resolved even if we include the effect of friction. Thus it seems to be a general trend that the direct reaction picture becomes less valid as the incident energy increases. Inclusion of other effects such as inelastic breakup or temporary formation of a fused system will be necessary.

Acknowledgements

I would like to express my appreciation to Professor M. Morita for his encouragement. Thanks are also due to Dr. T. Kammuri for his guidance and valuable discussions. He not only suggested the problems studied in this thesis but also contributed numerous ideas and suggestions.

I am deeply grateful to Professor M. Sano for his instruction and helpful discussions, and to Professor N. Takahashi for letting have the data of the polarization of ^{12}B.

I thank the members of Nuclear Theoretical Group at Osaka Univessity for fruitful discussions and encouragements.

The numerical calculations were performed by using TOSBAC 5600/160 at Research Center for Nuclear Physics, Osaka University.

Appendix

Below we give the derivation of eqs. (2.5) and (4.2) in chapter II with the line of the paper of Broglia and Winther.[9)]

To describe the intrinsic motion we attach an intrinsic coordinate system to each nucleus whose origin is specified by the classical variable R(t). We want to derive a wave function of a nucleus moving in the optical potential at the laboratory system. In this case the intrinsic motion of the nucleus is not excited.

We demand that the wave function ψ in the intrinsic coordinate system satisfies the Schrödinger equation

$$H\Psi = E\Psi \,. \tag{A.1}$$

A generalized Galilean transformation connects the laboratory system with the accelerated intrinsic coordinate system. We write the wave function Ψ in the laboratory system as

$$\Psi(\{\vec{r}_i\}) = e^{i\varphi(t)/\hbar}\, \psi(\{\vec{r}_i - \vec{R}(t)\})\, e^{-iEt/\hbar}, \tag{A.2}$$

where

$$\varphi(t) = \vec{V}(t)\cdot\sum m_i \vec{r}_i - \int_0^t \left(\frac{1}{2} m V^2(t') + m\vec{R}(t')\cdot\dot{\vec{V}}(t')\right) dt' . \tag{A.3}$$

In eq. (A.3) v is defined as $v(t) = \dot{R}(t)$, and m is the total mass. The wave function Ψ satisfies the equation

$$\left(H - i\hbar\frac{\partial}{\partial t}\right)\Psi = \dot{\vec{V}}(t)\cdot\left(\sum m_i \vec{r}_i - m\vec{R}(t)\right)\Psi \,. \tag{A.4}$$

In the incident channel the total Hamiltonian is

$$H = H_A + H_b + U_{Ab} + (V_{Ab} - U_{Ab}), \tag{A.5}$$

where H_A and H_b are the Hamiltonians of systems A and b respectively. The interaction between A and b is denoted by V_{Ab}, while the average potential of this interaction is U_{Ab} depending only on the relative coordinate $\mathbf{r}_{Ab} = \mathbf{r}_A - \mathbf{r}_b$, where $\mathbf{r}_A$ is the c.m. coordinate of system A and similar for $\mathbf{r}_b$.

We approximate the potential energy as

$$U_{Ab}(\mathbb{r}_{Ab}) = U_{Ab}(\mathbb{R}_{Ab}) + (\mathbb{r}_{Ab} - \mathbb{R}_{Ab}) \cdot \nabla U_{Ab}(\mathbb{R}_{Ab}), \tag{A.6}$$

where $R_{Ab} = R_A - R_b$. The coordinates R_A and R_b are the solutions of the classical equations of motion,

$$m_A \ddot{R}_A = - \nabla_A U_{Ab}(R_{Ab}), \tag{A.7a}$$

$$m_b \ddot{R}_b = - \nabla_b U_{Ab}(R_{Ab}) = \nabla_A U_{Ab}(R_{Ab}). \tag{A.7b}$$

For $t = -\infty$, the perturbing interaction $V_{Ab} - U_{Ab}$ can be neglected. Then the product wave function,

$$\tilde{\Phi}^{Ab}(t) = \Psi^A \Psi^b \exp\left[(i\hbar)^{-1} \cdot \int_0^t U_{Ab}(R_{Ab}(t'))\, dt'\right], \tag{A.8}$$

is the solution of the time-dependent Schrödinger equation

$$(H_A + H_b + U_{Ab})\, \tilde{\Phi}^{Ab}(t) = i\hbar \frac{\partial}{\partial t} \tilde{\Phi}^{Ab}(t), \tag{A.9}$$

where

$$\Psi^A = e^{i\varphi_A(t)/\hbar}\ \psi_A(\{\mathbf{r}_i - \mathbf{R}_A(t)\})\ e^{iE_A t/\hbar}, \tag{A.10}$$

and similar for Ψ^b. The intrinsic wave functions ψ_A and ψ_b are eigen states of H_A and H_b with the eigen values E_A and E_b, respectively. In order to derive the result of eq. (A.9), we have used the identity

$$\begin{aligned}
&\dot{\mathbf{V}}_A \cdot \Big(\sum_{i\in A} m_i \mathbf{r}_i - m_A \mathbf{R}_A(t)\Big) + \dot{\mathbf{V}}_b \cdot \Big(\sum_{i\in b} m_i \mathbf{r}_i - m_b \mathbf{R}_b(t)\Big) \\
&= m_A \dot{\mathbf{V}}_A \cdot \big(\mathbf{r}_A - \mathbf{R}_A(t)\big) + m_b \dot{\mathbf{V}}_b \cdot \big(\mathbf{r}_b - \mathbf{R}_b(t)\big) \\
&= -\nabla U_{Ab}(R_{Ab}) \cdot \big(\mathbf{r}_{Ab} - \mathbf{R}_{Ab}(t)\big) .
\end{aligned} \tag{A.11}$$

In the exit channel we can also define analogous states $\tilde{\Phi}^{aB}$. The set of wave functions $\tilde{\Phi}^{Ab}$ and $\tilde{\Phi}^{aB}$ is not orthogonal. To solve the Schrödinger equation

$$H\,\tilde{\Phi} = i\hbar \frac{\partial}{\partial t}\tilde{\Phi}, \tag{A.12}$$

we expand the total wave function $\tilde{\Phi}$ on the product wave functions

$$\tilde{\Phi} = \sum_{Ab} C^{Ab}(t)\ \tilde{\Phi}^{Ab}(t) + \sum_{aB} C^{aB}(t)\ \Phi^{aB}(t). \tag{A.13}$$

Inserting this wave function into eq. (A.12) we find

$$\begin{aligned}
&i\hbar \sum_{Ab} \dot{C}^{Ab}(t)\ \tilde{\Phi}^{Ab}(t) + i\hbar \sum_{aB} \dot{C}^{aB}(t)\ \tilde{\Phi}^{aB}(t) \\
&= \sum_{Ab} C^{Ab}(t)\,(V_{Ab} - U_{Ab})\,\tilde{\Phi}^{Ab}(t) + \sum_{aB} C^{aB}(t)\,(V_{aB} - U_{aB})\,\tilde{\Phi}^{aB}(t).
\end{aligned} \tag{A.14}$$

If we neglect the overlap integral ($\tilde{\Phi}^{aB}$, $\tilde{\Phi}^{Ab}$), we can get the equation

$$\dot{C}^{aB}(t) = \frac{1}{i\hbar} \sum_{A'b'} \left(\tilde{\Phi}^{aB} . (V_{Ab} - U_{Ab}) \tilde{\Phi}^{A'b'} \right) C^{A'b'}(t)$$

$$+ \frac{1}{i\hbar} \sum_{a'B'} \left(\tilde{\Phi}^{aB} . (V_{aB} - U_{aB}) \tilde{\Phi}^{a'B'} \right) C^{a'B'}(t) . \qquad \text{(A.15)}$$

Further assuming that

$$C^{a'B'}(t) = 0 ,$$

$$C^{A'b'}(t) = \delta_{AA'} \delta_{bb'} , \qquad \text{(A.16)}$$

on the right-hand side of this equation, we find the lowest-order approximation $C^{(1)}_{if}(t)$ for the amplitude $C^{aB}(t)$ as

$$C^{(1)}_{if}(t) = \frac{1}{i\hbar} \int_{-\infty}^{t} f^{(1)}_{if}(t')\, dt' , \qquad \text{(A.17)}$$

where

$$f^{(1)}_{if}(t) = \left(\tilde{\Phi}^{aB} . (V_{Ab} - U_{Ab}) \tilde{\Phi}^{Ab} \right) . \qquad \text{(A.18)}$$

For the two-step sequential transfer process, the lowest-order amplitude $C^{(1)}_{im}$ to an intermediate state m is

$$C^{(1)}_{im}(t) = \frac{1}{i\hbar} \int_{-\infty}^{t} f^{(1)}_{im}(t)\, dt . \qquad \text{(A.19)}$$

We can therefore find the second-order amplitude via an intermediate state m that

$$C_{if}^{(2)}(t) = \left(\frac{1}{i\hbar}\right)^2 \int_{-\infty}^{t} f_{mf}^{(1)}(t') \cdot C_{im}^{(1)}(t') \, dt'$$

$$= \left(\frac{1}{i\hbar}\right)^2 \int_{-\infty}^{t} f_{mf}^{(1)}(t') \, dt' \int_{-\infty}^{t'} f_{im}^{(1)}(t'') \, dt'' . \qquad \text{(A.20)}$$

For t = $+\infty$, eqs. (A.17) and (A.19) reduce to eqs. (2.5) and (4.2) in chapter II, respectively.

References

1) T. Udagawa and T. Tamura, Phys. Rev. Lett. 41 (1978) 1770

2) M. Ishihara, T. Shimoda, H. Frȍhlich, H. Kamitsubo, K. Nagatani, T. Udagawa and T. Tamura, Phys. Rev. Lett. 43 (1979) 111

3) H. Frȍhlich, T. Shimoda, M. Ishihara, K. Nagatani, T. Udagawa and T. Tamura, Phys. Rev. Lett. 42 (1979) 1519

4) T. Udagawa, T. Tamura and B. T. Kim, Phys. Lett. 82B (1979) 349

5) M. C. Mermaz, Phys. Rev. C21 (1980) 2356

6) K. W. McVoy and M. C. Nemes, Z. Phys. A295 (1980) 177

7) D. M. Brink, Phys. Lett. 40B (1972) 37

8) N. Anyas-Weiss, J. Becker, T. A. Belote, J. C, Cornell, P. S. Fisher, P. N. Hudson, A. Menchaca-Rocha, A. D. Panagiotou and D. K. Scott, Phys. Lett. 45B (1973) 231

9) R. A. Broglia and A. Winther, Nucl. Phys. A182 (1972) 112

10) M. Ishihara, K. Tanaka, T. Kammuri, K. Matsuoka and M. Sano, Phys. Lett. 73B (1978) 281

11) K. Sugimoto, N. Takahashi, A. Mizobuchi, Y. Nojiri, T. Minamisono, M. Ishihara, K. Tanaka and H. Kamitsubo, Phys. Rev. Lett. 39 (1977) 323

12) N. Takahashi, Y. Miake, Y. Nojiri, T. Minamisono, A. Mizobuchi, M. Ishihara and K. Sugimoto, Phys. Lett. 78B (1978) 397

13) T. Udagawa, T. Tamura, T. Shimoda. H. Frȍhlich, M. Ishihara and K. Nagatani, Phys. Rev. C20 (1979) 1949 ; E. Takada. T. Shimoda, N. Takahashi, T. Yamaya, K. Nagatani, T. Udagawa and T. Tamura, Phys. Rev. C23 (1981) 772

14) J. B. Natowitz, M. N. Namboodiri, R. Eggers, P. Gonthier, K. Geoffroy, R. Hanus, C. Towsley and K. Das, Nucl. Phys, A277 (1977) 477

15) D. M. Brink, Les Houches, Session XXX, 1977, Nuclear physics with heavy ions and mesons, ed. R. Balian et al. (North-Holland, Amsterdam, 1978) p.1

16) P. J. Siemens, J. P. Bondorf, D. H. E. Gross and F. Dickmann, Phys. Lett. 36B (1971) 24

17) A. R. Farhan, J. George and H. Überall, Nucl. Phys. A305 (1978) 189 ; H. Überall, Electron scattering from complex nuclei (Academic Press, New York, 1971) vol. II

18) Handbook of Mathematical Functions, ed. M. Abramowitz and I. A. Stegun (Dover, New York, 1965)

19) K. Dietrich, Ann. Phys. 66 (1971) 480

20) H. Feshbach, A. Kerman and S. Koonin, Ann. Phys. 125 (1980) 429

21) T. Ericson, Adv. Phys. 9 (1960) 423

22) A. Gilbert and A. G. W. Cameron, Can. J. Phys. 43 (1965) 1446

23) N. Anyas-Weiss, J. C. Cornell, P. S. Fisher, P. N. Hudson, A. Menchaca-Rocha, D. J. Millener, A. D. Panagiotou, D. K. Scott, D. Strottman, D. M. Brink, B. Buck, P. J. Ellis and T. Engeland, Phys. Rep. 12C (1974) 201

24) T. Mikumo, I. Kohno, K. Katori, T. Motobayashi, S. Nakajima, M. Yoshie and H. Kamitsubo, Phys. Rev. C14 (1976) 1458

25) M. Yoshie and I. Kohno, Sci. Papers Inst. Phys. Chem. Res. 69 (1975) 63

26) F. Videbaek, R. B. Goldstein, L. Grodzins, S. G. Steadman, T. A. Belote and J. D. Garrett, Phys. Rev. C15 (1977) 954

27) C. Olmer, M, C. Mermaz, M. Buenerd, C. K. Gelbke, D. L. Hendrie, J. Mahoney, A. Menchaca-Rocha, D. K. Scott, M. H. Macfarlane and S. C. Pieper, Phys. Rev. Lett. 38 (1977) 476

28) S. Cohen and D. Kurath, Nucl. Phys. A101 (1967) 1

29) S. Cohen and D. Kurath, Nucl. Phys. A141 (1970) 145

30) D. H. Feng, T. Udagawa and T. Tamura, Nucl. Phys. A274 (1976) 262

31) T. Kammuri, Z. Phys. A287 (1978) 85

32) Y. Alhassid, R. D. Levine, J. S. Karp and S. G. Steadman, Phys. Rev. C20 (1979) 1789

33) T. Shimoda, Ph. D. Thesis (1980)

34) D. Kurath, Phys. Rev. C7 (1973) 1390

35) K. T. Hecht and D. Braunschweig, Nucl. Phys, A244 (1975) 365

36) K. W. Ford and J. A. Wheeler, Ann. of Phys. 7 (1959) 259

37) J. B. Natowitz, M. N. Namboodiri, R. Eggers, P. Gonthier, K. Geoffroy, R. Hanus, C. Towsley and K. Das, Nucl. Phys. A277 (1977) 477

38) J. B. Ball, C. B. Fulmer, M. L. Mallory and R. L. Robinson, Phys. Rev. Lett. 40 (1978) 1698

39) M. Sasagase, M. Sato, S. Hanashima, K. Furuno, Y. Nagashima, Y. Tagishi, S. M. Lee and T. Mikumo, preprint (1980)

40) H. Hasan and D. M. Brink, J. Phys. G4 (1978) 1573 ; ibid G5 (1979) 771

Table Caption

Table 1. Strength of nuclear attraction, rotation angle and level density parameters. For each reaction the upper part is for the straight-line, the lower part for the circular-trajectory case. Symbol a) means the case for large scattering angles.

Reactions	V_N (MeV)	Θ	$\mathcal{J}/\hbar^2$ (MeV^{-1})	T (MeV)	$\mathcal{J}T/\hbar^2$	$n^2\langle m^2\rangle$	$n\langle m^2\rangle$
$^{53}Cr(^{14}N, ^{13}C)$	28		0.76	6	4.56		2.09
$^{96}Mo(^{14}N, ^{15}O)$	28		1.05	6	6.30		3.04
$^{181}Ta(^{16}O, ^{17}O)$	28		1.51	6	9.06		4.65
$^{208}Pb(^{16}O, ^{15}N)$	28		1.64	6	9.84		5.11
$^{100}Mo(^{14}N, ^{12}B)$							
90MeV	28	0.7	2.35	5	11.8	12.8	6.38
125MeV	0			5			
	0	0.6		5			
200MeV	0			6	14.1		
	0	0.5		6			
$^{100}Mo(^{14}N, ^{13}C)$	28		1.09	6	6.54	3.10	
	0	0.4		5	5.45		
$^{101}Tc(^{13}C, ^{12}B)$	28		1.09	6	6.54	3.19	
	0	0.4		5	5.45		
$^{27}Al(^{20}Ne, ^{16}O)$	16		2.53	10	25.3	23.1	5.76
	10	0.6		6	15.2		
$^{31}P(^{16}O, ^{12}C)$	16		2.73	10	27.3	25.0	6.24
	10	0.6		6	16.4		
$^{40}Ca(^{20}Ne, ^{16}O)$	28		3.14	6	18.8	29.1	7.28
	0	0.4 (0.17)[a]					
$(^{14}N, ^{10}B)$	28						
	0	0.4 (0.4)[a]					
$(^{13}C, ^{9}Be)$	28						
	0	0.4 (0.3)[a]					
$^{197}Au(^{19}F, ^{12}B)$	10		13.9	10	139.2	247.9	35.4
	10	0.35 / 0.55					

Table 1

Figure Captions

Fig. 1. Position vectors used in the transfer reaction $A + b \to a + B$ in which $A = a + n$ and $B = b + n$.

Fig. 2. Positions of nuclei a, b and transferred particle n at the time t after the closest approach. The y-axis is tangent to the trajectory of the relative motion at $t = 0$, while the z-axis is parallel to the $\mathbf{k}_f \times \mathbf{k}_i$ direction for the repulsive scattering. The x'-axis is directed from the nucleus b to a at the time t, and the z'-axis coincides with the z-axis.

Fig. 3. Positions of nuclei a and b at the time t after the closest approach. For small t the trajectory of the relative motion is approximated by a straight line parallel to the y-axis, and the velocity in the region of transfer is taken to be constant.

Fig. 4. Transition probabilities $|c_{if}^{(l)}|^2$ for three different values of λ_1 (solid lines) and their superposition (dashed line), plotted versus $-Q_{eff}$. In this schematic figure, ℓ_1 is taken to be 2.

Fig. 5. Effects of varying the level density formula and the nuclear temperature on the energy spectra of $^{40}Ca(^{20}Ne, {}^{16}O)^{44}Ti$ reaction at 262 MeV incident energy. We have fixed $\ell_1 = 3$, $V_N = 28$ MeV and $\mathcal{J} = 3.14\ \text{MeV}^{-1}$. The top, middle and bottom graphs make use of the following three types of level densities : $\rho_\ell(E^*) = 1$, $(2\ell + 1)\exp\{E^*/T - \frac{1}{2}\ell(\ell + 1)/\mathcal{J}T\}$ and $(2\ell + 1)(E^*/T)^3\exp\{-\frac{1}{2}\ell(\ell + 1)/\mathcal{J}T\}$. Dotted curves in the top of the graph are the components with specified λ_1. In the lower two parts, each curve corresponds to a different choice of the nuclear temperature T. In this and all the following graphs, E^* in the abscissa means the sum of excitation energies of both final nuclei.

Fig. 6. Comparison of theory and experiment for the energy spectrum of the $^{53}Cr(^{14}N, ^{13}C)$ reaction at 90 MeV incident energy.

Fig. 7. Comparison of theory and experiment for the energy spectrum of the $^{96}Mo(^{14}N, ^{15}O)$ reaction at 97 MeV incident energy.

Fig. 8. Comparison of theory and experiment for the energy spectum of the $^{181}Ta(^{16}O, ^{17}O)$ reaction at 96 MeV incident energy.

Fig. 9. Comparison of theory and experiment for the energy spectrum of the $^{208}Pb(^{16}O, ^{15}N)$ reaction at 312.6 MeV incident energy.

Fig. 10. Effect of varying V_N on the $^{53}Cr(^{14}N, ^{13}C)^{54}Mn$ reaction at 90 MeV incident energy.

Fig. 11. Energy spectrum and polarization of ^{12}B in the $^{100}Mo(^{14}N, ^{12}B)$ reaction at 90 MeV incident energy. Successive transfer of two nucleons is assumed. Dotted and dashed curves are the contributions from the real and imaginary parts of the transition amplitude, respectively. Their sum is shown by the solid curve.

Fig. 12. Classical deflection function of the $^{100}Mo(^{14}N, ^{12}B)^{102}Ru$ reaction at 90 MeV incident energy. Solid curves, bold and thin, are calculated for $E^* = 0$ by taking the total potential and Coulomb potential, respectively. Dotted curves are the corresponding results for $E^* = 10$ MeV. Dot-dashed curve is obtained by using the point Coulomb potential at $E^* = 0$.

Fig. 13. Effect of varying the rotation angle θ of the incident ion around the target for the $^{100}Mo(^{14}N, ^{12}B)^{102}Ru$ reaction at 90 MeV incident energy. One-step process with $V_N = 0$ and $T = 5$ MeV is assumed.

Fig. 14. Effect of varying the temperature T in the level density for the $^{100}Mo(^{14}N, ^{12}B)^{102}Ru$ reaction at 90 MeV incident energy. Circular trajectory and one-step process are assumed and $V_N = 0$, $\theta = 0.4$ are taken.

Fig. 15. Same as in fig. 14 except for $\theta = 0.5$.

Fig. 16. Same as in fig. 13 except for the sequential transfer process.

Fig. 17. Same as in fig. 14 except for the sequential transfer process.

Fig. 18. Comparison of theory and experiment for the energy spectra and polarizations of the $^{100}Mo(^{14}N, ^{12}B)$ reaction at 90 MeV incident energy. Both curves are calculated by assuming the circular orbit. Solid curve is the one-step result with $V_N = 28$ MeV, $T = 5$ MeV and $\theta = 0.7$. Dashed curve is the two-step result with $V_N = 0$, $T = 5$ MeV and $\theta = 0.4$.

Fig. 19. Comparison of theory and experiment for the energy spectra and polarizations of the $^{100}Mo(^{14}N, ^{12}B)$ reaction at 125 MeV incident energy. $V_N = 0$ and $T = 5$ MeV are used. Dashed and solid curves are calculated by assuming the straight-line trajectory with and without friction, respectively. Dotted curve is the result of the circular orbit of rotation angle $\theta = 0.6$ and with friction. The α coefficient is 1.25.

Fig. 20. Same as in fig. 19 except for 200 MeV incident energy, $T = 6$ MeV and $\theta = 0.5$.

Fig. 21. Comparison of theory and experiment for the energy spectra of the $^{40}Ca(^{20}Ne, ^{16}O)$, $^{40}Ca(^{14}N, ^{10}B)$ and $^{40}Ca(^{13}C, ^{9}Be)$ reactions. Incident energies are 262, 153 and 149 MeV and laboratory scattering angles are 5°, 8° and 8°, respectively. Solid curves are the sum of the transitions to the levels of emitted particles with large

α-spectroscopic factors, while dotted curves include only the ground state transition. V_N = 28 MeV and T = 6 MeV are used. Dashed curves are calculated by assuming the circular trajectory with θ = 0.4, V_N = 0 MeV, and T = 6 MeV.

Fig. 22. Classical deflection function for the $^{40}Ca(^{20}Ne, ^{16}O)^{44}Ti$ reaction at 262 MeV incident energy. Solid curves, bold and thin, are calculated for E* = 0 by taking the total potential and Coulomb potential, respectively. Dashed and dotted curves are the corresponding results for E* = 40 and 80 MeV. Dot-dashed curve is obtained by using the point Coulomb potential at E* = 0.

Fig. 23. Fit to the energy spectra of the $^{40}Ca(^{20}Ne, ^{16}O)$, $^{40}Ca(^{14}N, ^{10}B)$ and $^{40}Ca(^{13}C, ^{9}Be)$ reactions. Incident energies are 262, 153 and 149 MeV and laboratory scattering angles are 16°, 20° and 20°, and rotation angles used in the circular trajectory calculations are 0.17, 0.4 and 0.3, respectively.

Fig. 24. Effect of varying V_N on the $^{40}Ca(^{20}Ne, ^{16}O)^{44}Ti$ reaction at 262 MeV incident energy. For simplicity ℓ_1 is taken to be 0.

Fig. 25. Comparison of the semiclassical calculation and experiment for the angular distributions of the $^{40}Ca(^{20}Ne, ^{16}O)$, $^{40}Ca(^{14}N, ^{10}B)$ and $^{40}Ca(^{13}C, ^{9}Be)$ reactions at 262, 153 and 149 MeV incident energies, respectively.

Fig. 26. Comparison of theory and experiment for the energy spectra of the $^{27}Al(^{20}Ne, ^{16}O)$ and $^{27}Al(^{20}Ne, ^{12}C)$ reactions at 120 MeV incident energy. Solid and dotted curves are calculated by using the straight-line trajectories with T = 10 MeV and V_N = 16 MeV, while dot-dashed curves are the results with circular trajectories obtained by use of θ = 0.6, T = 6 MeV and V_N = 10 MeV. Dotted curve includes only the transition to the ground state of ^{16}O.

Fig. 27. Comparison of theory and experiment for the energy spectra and polarizations of the $^{197}Au(^{19}F, ^{12}B)$ reaction at 186 MeV incident energy. Solid curve is calculated by assuming a straight-line trajectory. Dashed and dotted curves are the results of circular orbits with $\theta = 0.35$ and 0.55, respectively. $V_N = 10$ MeV and $T = 10$ MeV are used in all cases.

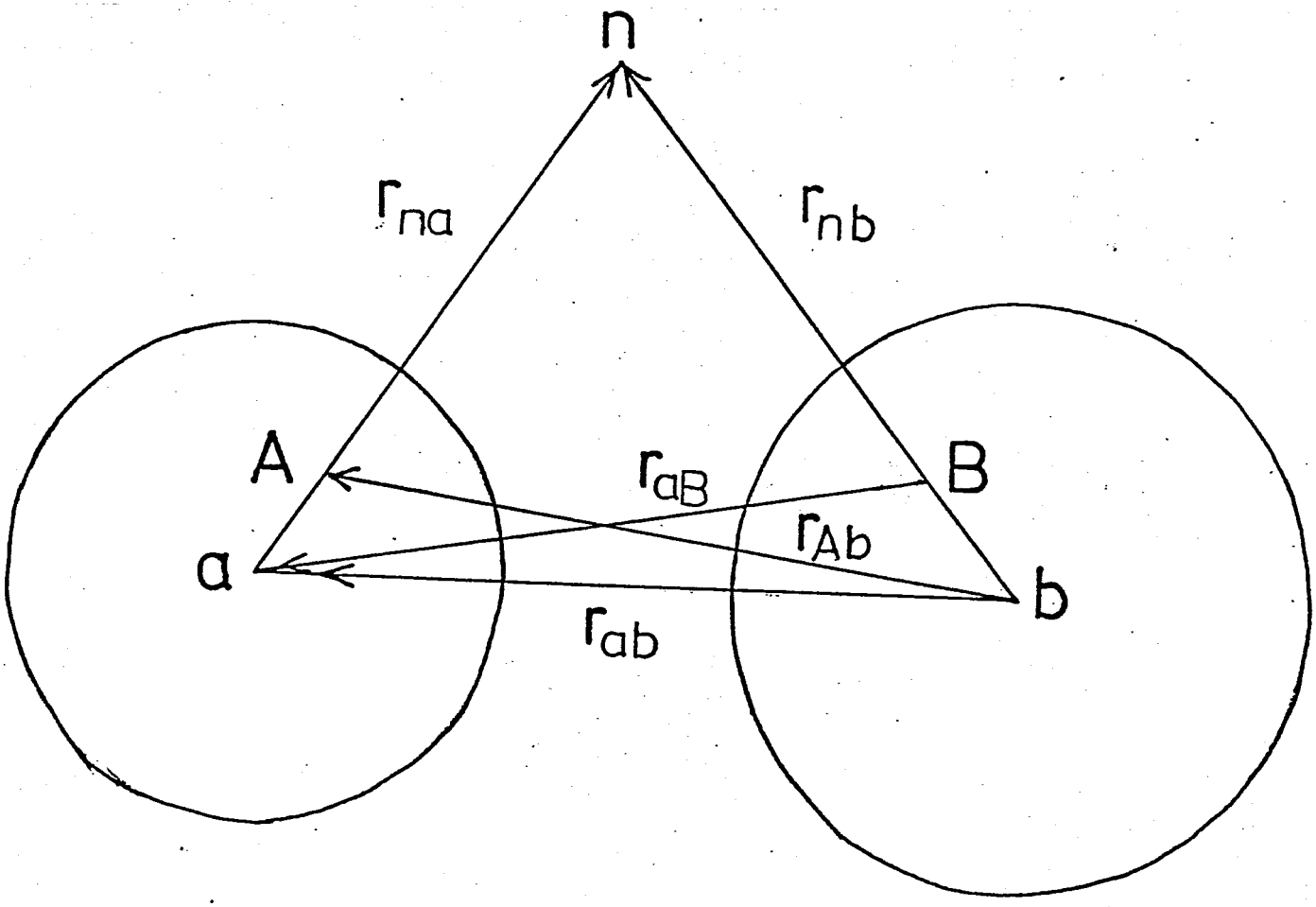

Fig. 1.

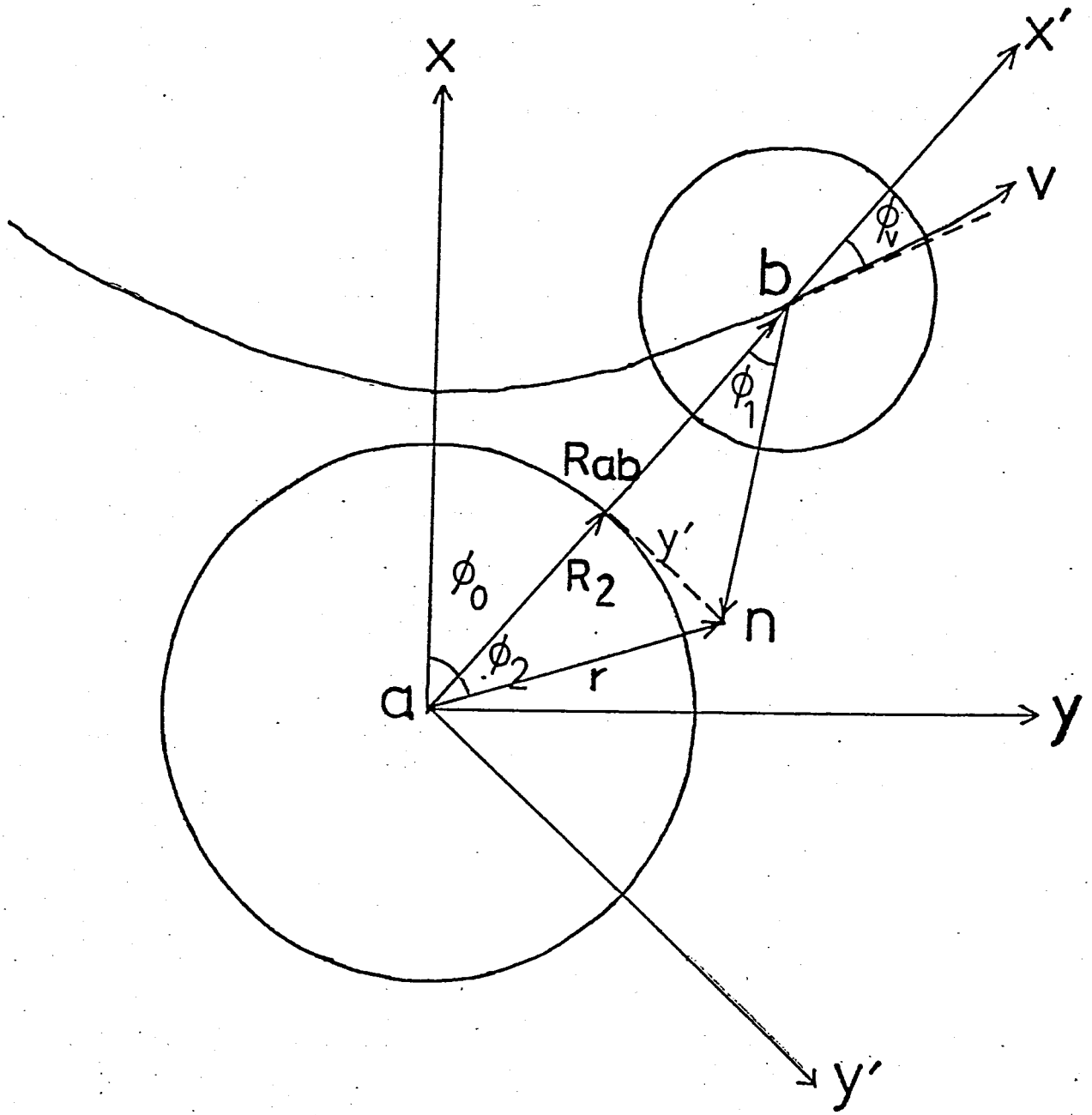

Fig. 2.

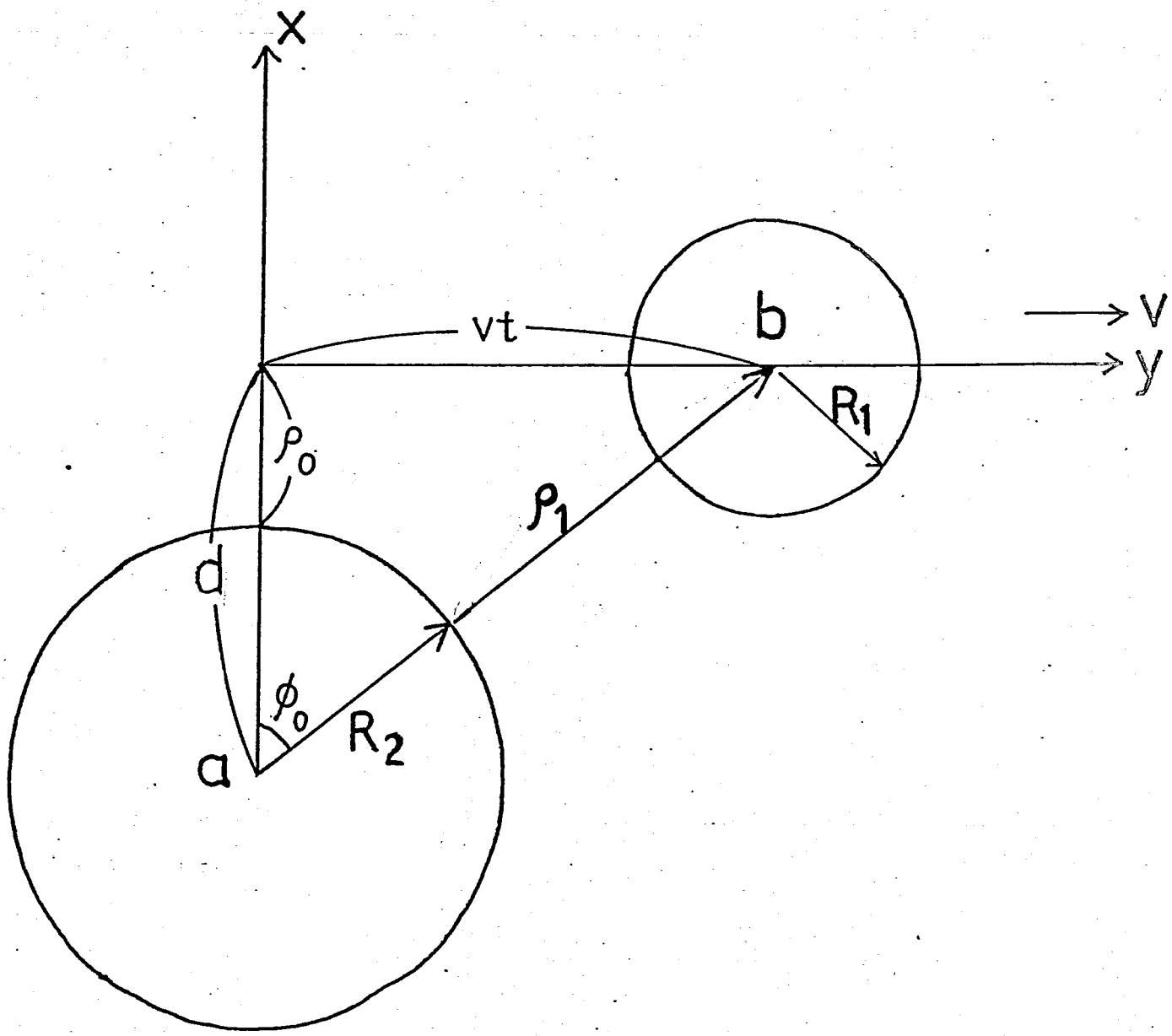

Fig. 3.

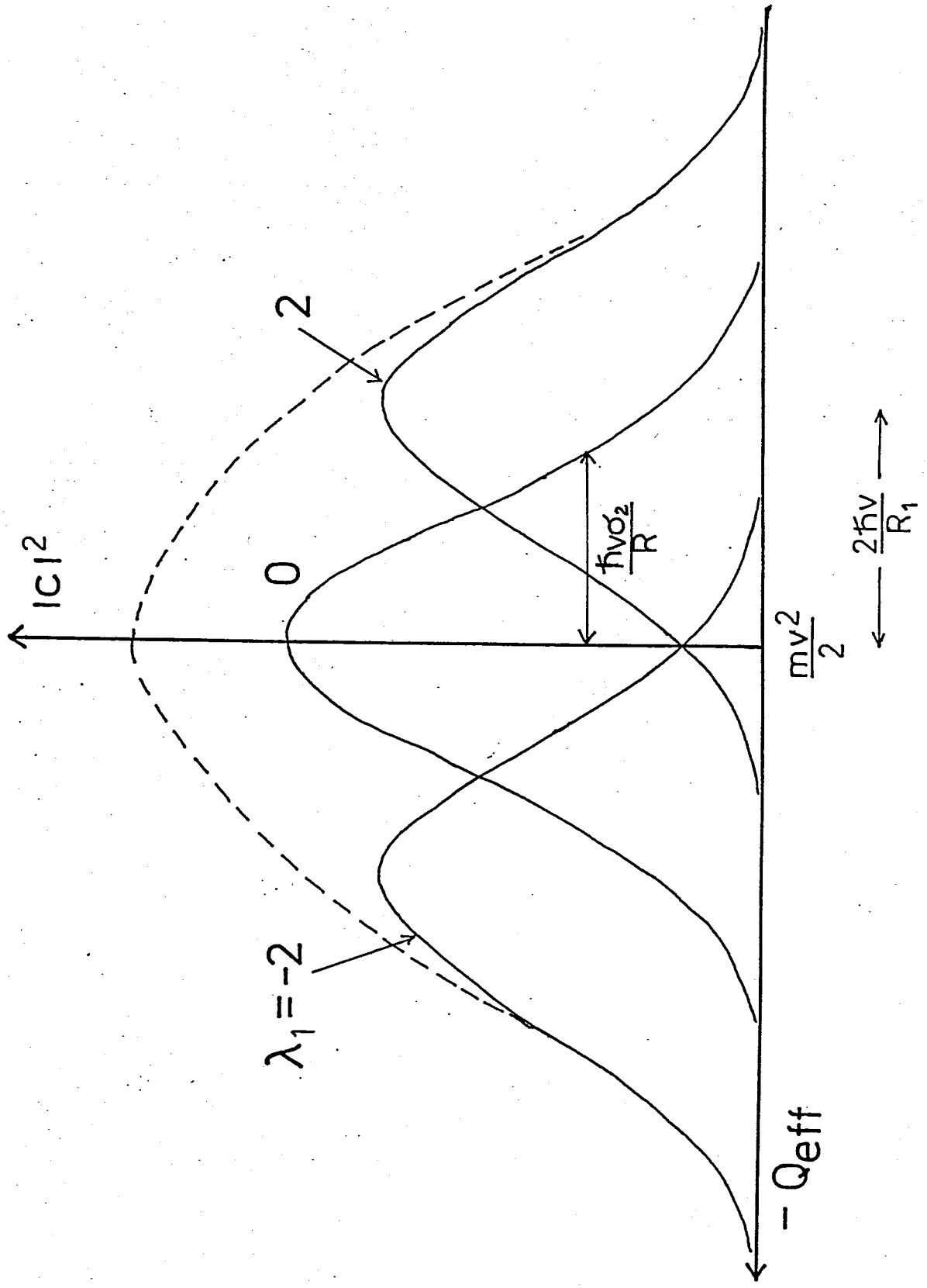

Fig. 4.

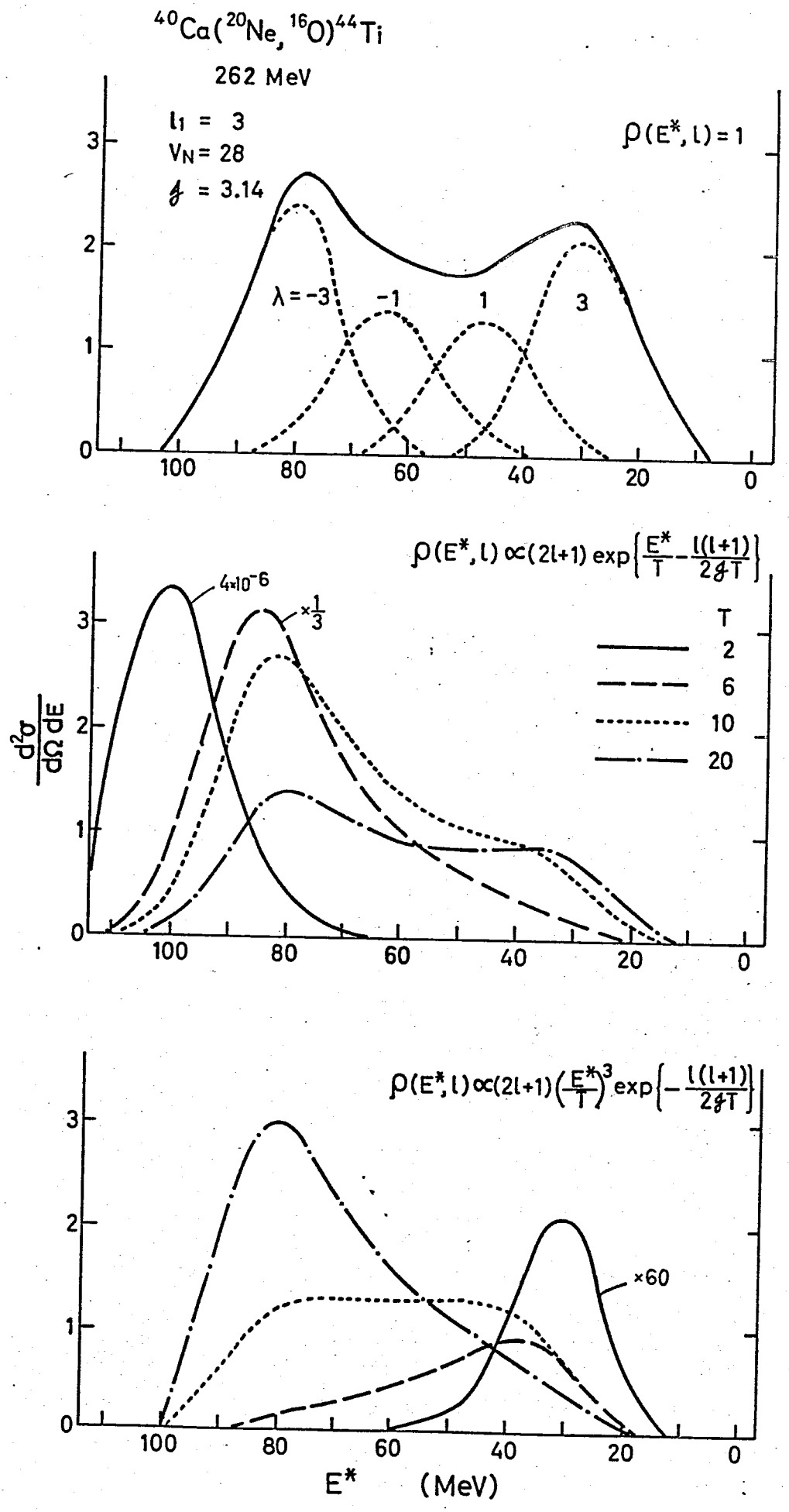
$^{40}Ca(^{20}Ne, ^{16}O)^{44}Ti$
262 MeV
$l_1 = 3$
$V_N = 28$
$\mathcal{J} = 3.14$
$\rho(E^*, l) = 1$
$\lambda = -3$
-1
1
3
$\rho(E^*, l) \propto (2l+1) \exp\left\{\frac{E^*}{T} - \frac{l(l+1)}{2\mathcal{J}T}\right\}$
4×10^{-6}
$\times\frac{1}{3}$
T
2
6
10
20
$\frac{d^2\sigma}{d\Omega\, dE}$
$\rho(E^*, l) \propto (2l+1)\left(\frac{E^*}{T}\right)^3 \exp\left\{-\frac{l(l+1)}{2\mathcal{J}T}\right\}$
$\times60$
E^* (MeV)

Fig. 5.

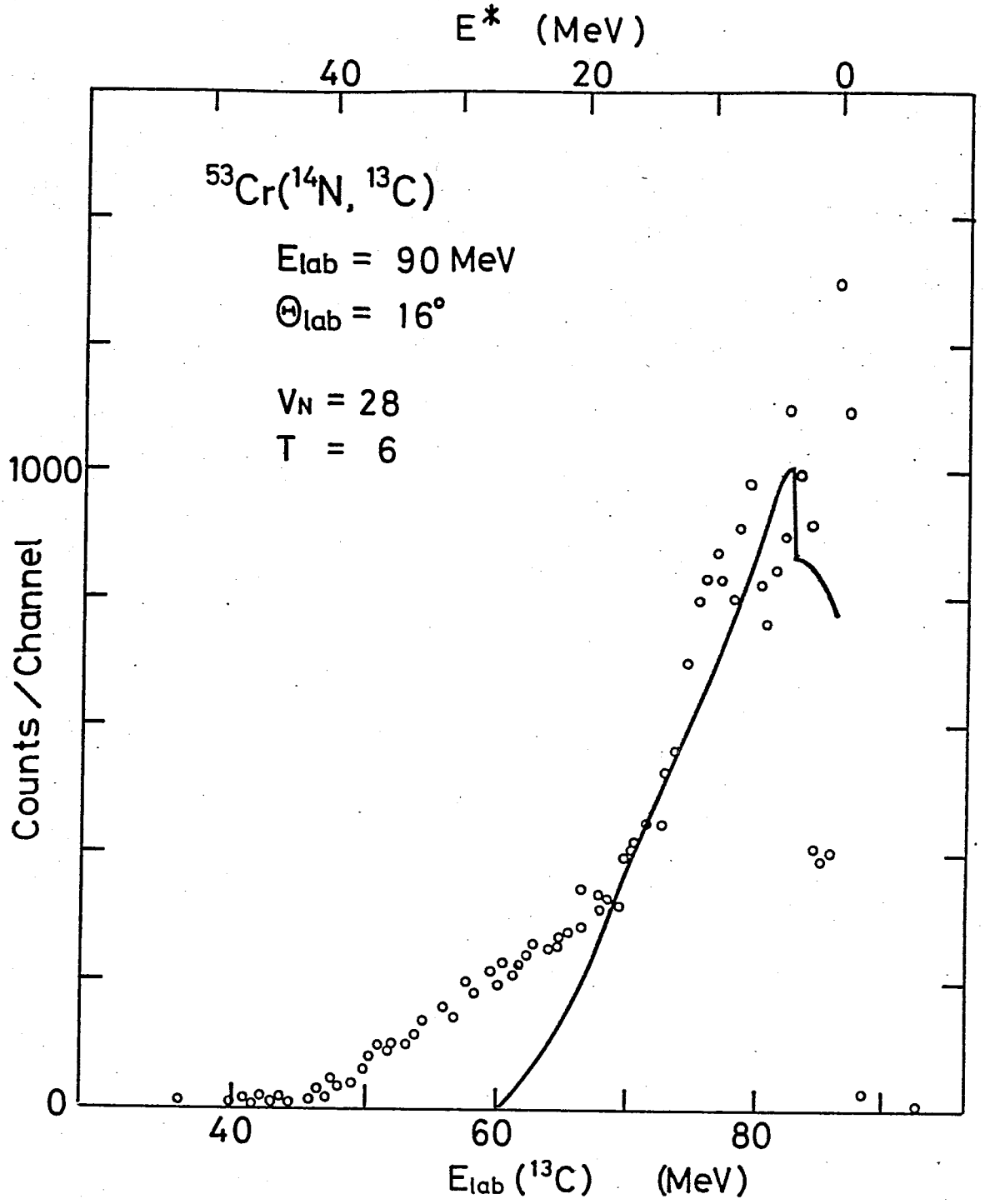
E* (MeV)
40
20
0
$^{53}Cr(^{14}N, ^{13}C)$
E_{lab} = 90 MeV
Θ_{lab} = 16°
V_N = 28
T = 6
1000
0
Counts / Channel
40
60
80
E_{lab} (^{13}C) (MeV)

Fig. 6.

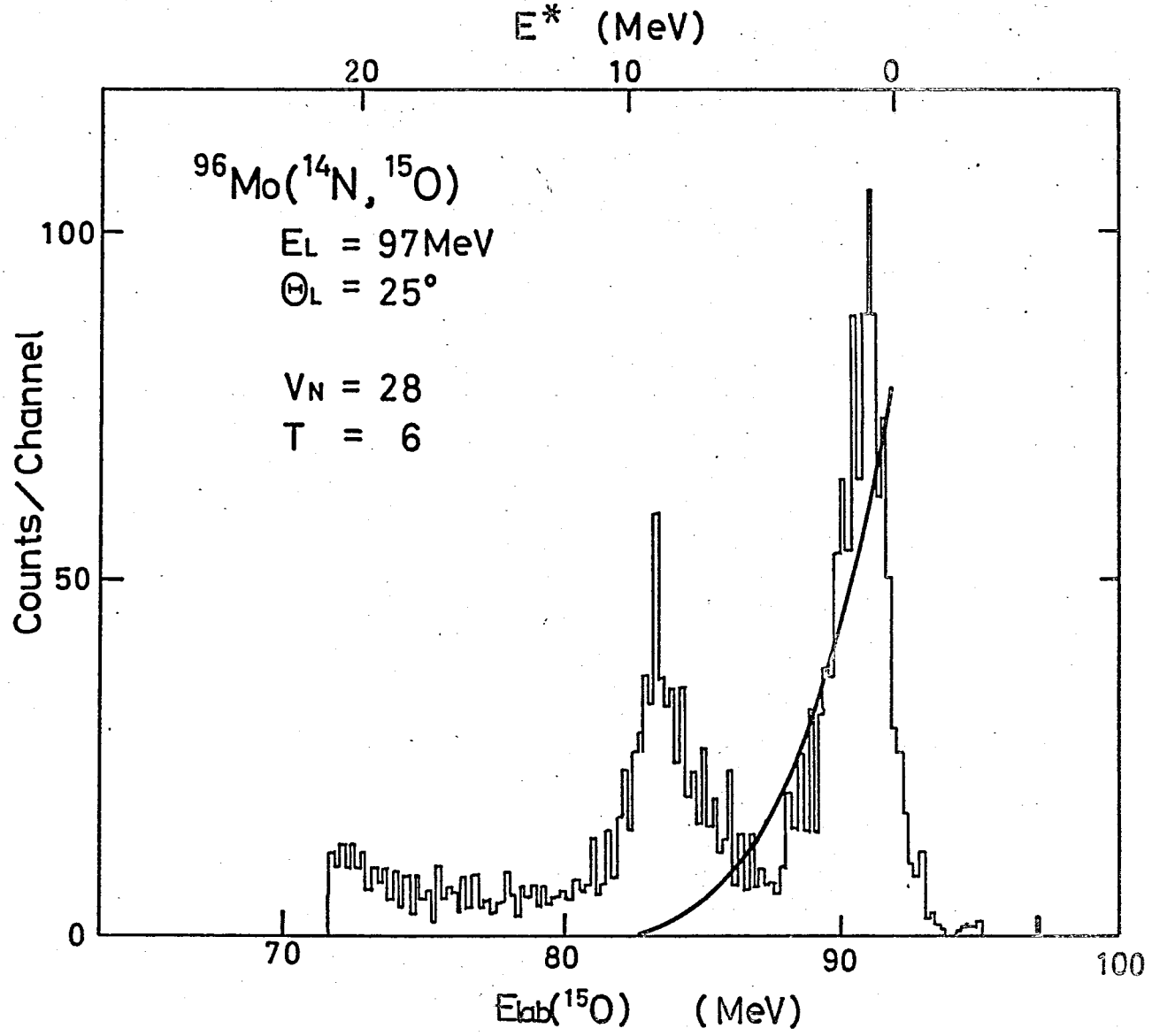
E* (MeV)
20
10
0
$^{96}Mo(^{14}N, ^{15}O)$
E_L = 97MeV
Θ_L = 25°
V_N = 28
T = 6
Counts/Channel
100
50
0
70
80
90
100
$E_{lab}(^{15}O)$ (MeV)

Fig. 7.

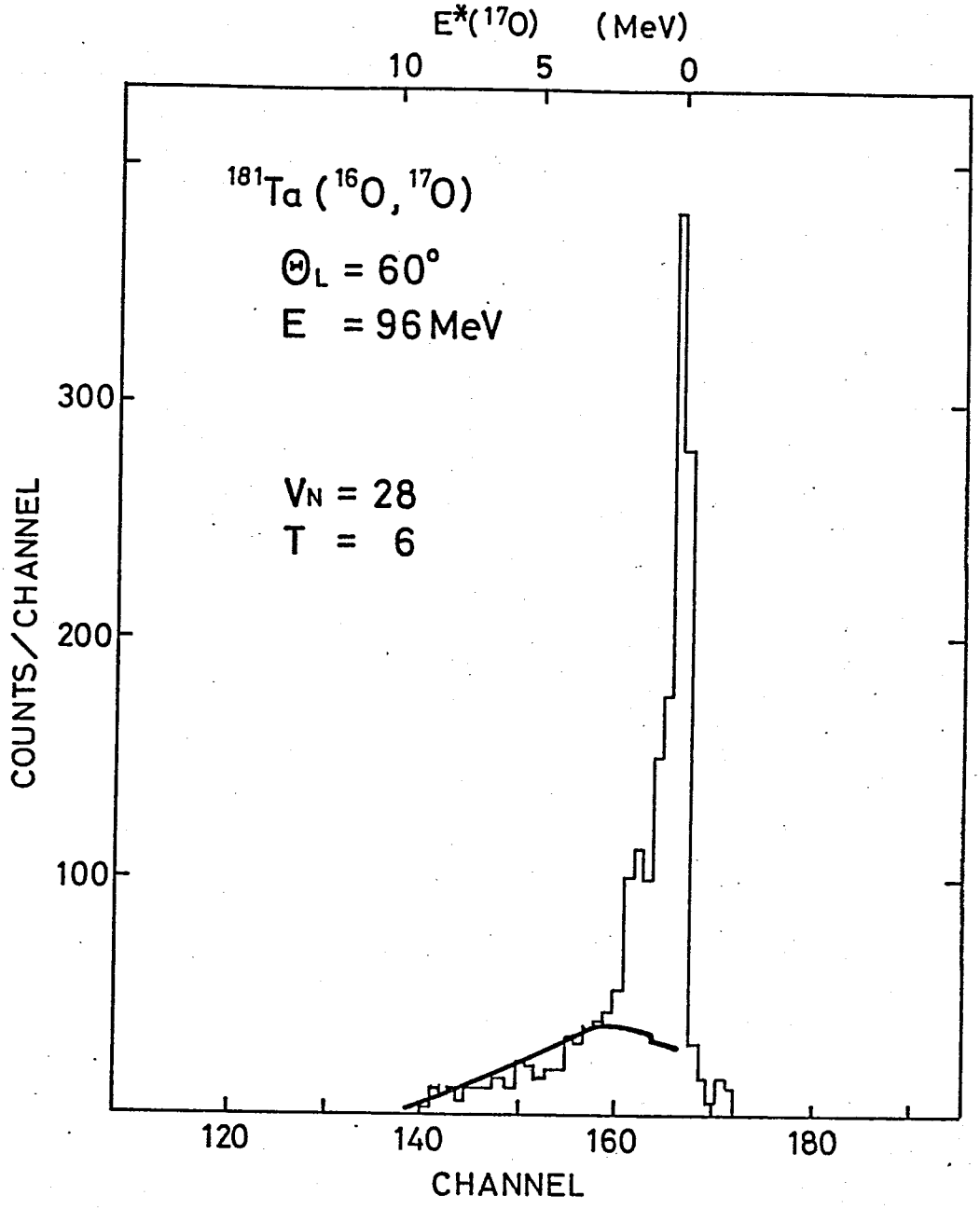
E*(17O) (MeV)
10
5
0
181Ta (16O, 17O)
ΘL = 60°
E = 96 MeV
VN = 28
T = 6
300
200
100
COUNTS/CHANNEL
120
140
160
180
CHANNEL

Fig. 8.

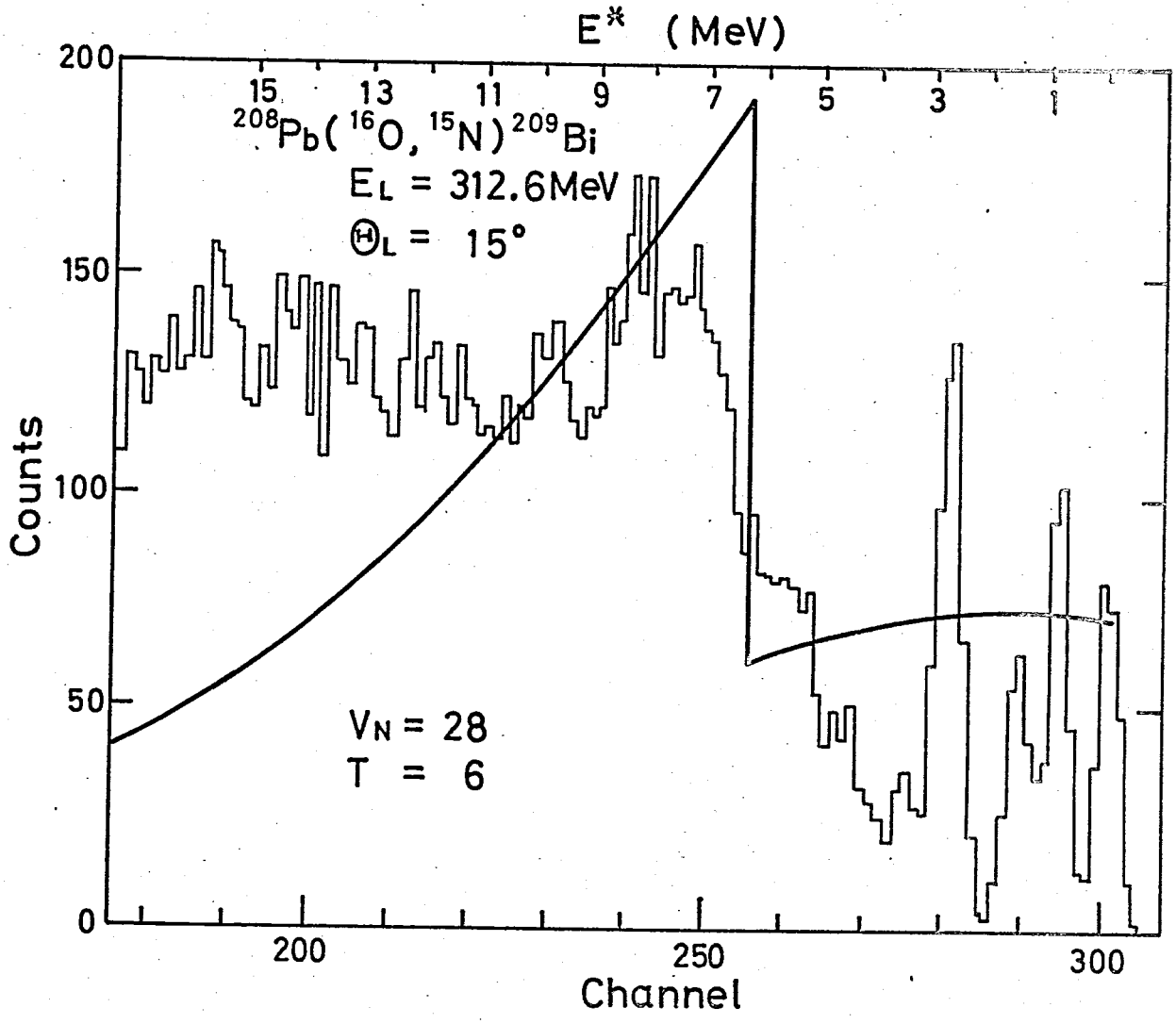
E* (MeV)
15
13
11
9
7
5
3
1
$^{208}Pb(^{16}O,^{15}N)^{209}Bi$
E_L = 312.6MeV
Θ_L = 15°
V_N = 28
T = 6
Counts
200
150
100
50
0
200
250
300
Channel

Fig. 9.

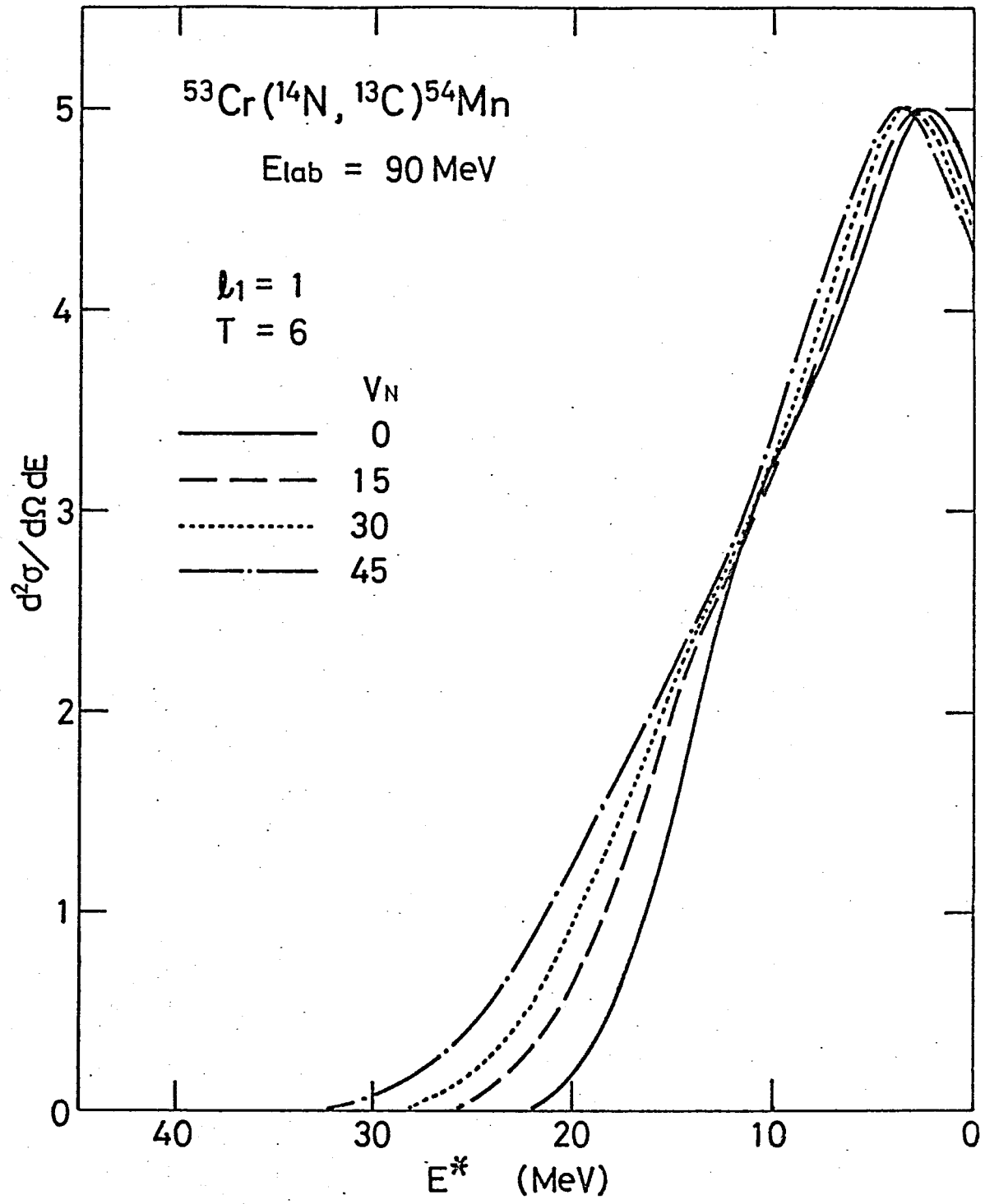
$^{53}Cr(^{14}N, ^{13}C)^{54}Mn$
Elab = 90 MeV
$\ell_1 = 1$
T = 6
V_N
0
15
30
45
$d^2\sigma/d\Omega dE$
0
1
2
3
4
5
40
30
20
10
0
E* (MeV)

Fig. 10.

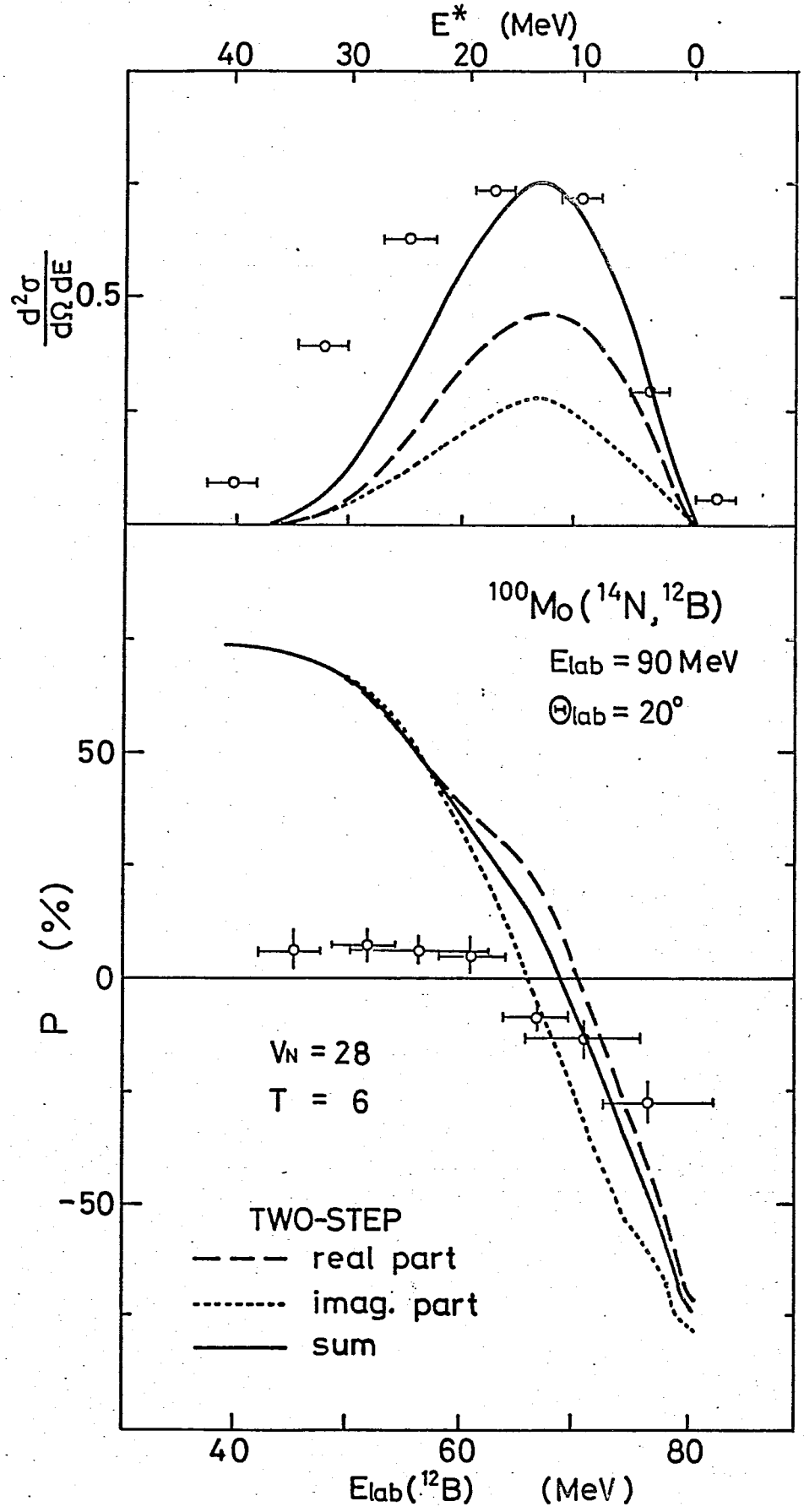
E* (MeV)
40
30
20
10
0
d²σ/dΩdE
0.5
100Mo (14N, 12B)
Elab = 90 MeV
Θlab = 20°
50
P (%)
0
VN = 28
T = 6
-50
TWO-STEP
real part
imag. part
sum
40
60
80
Elab(12B) (MeV)

Fig. 11.

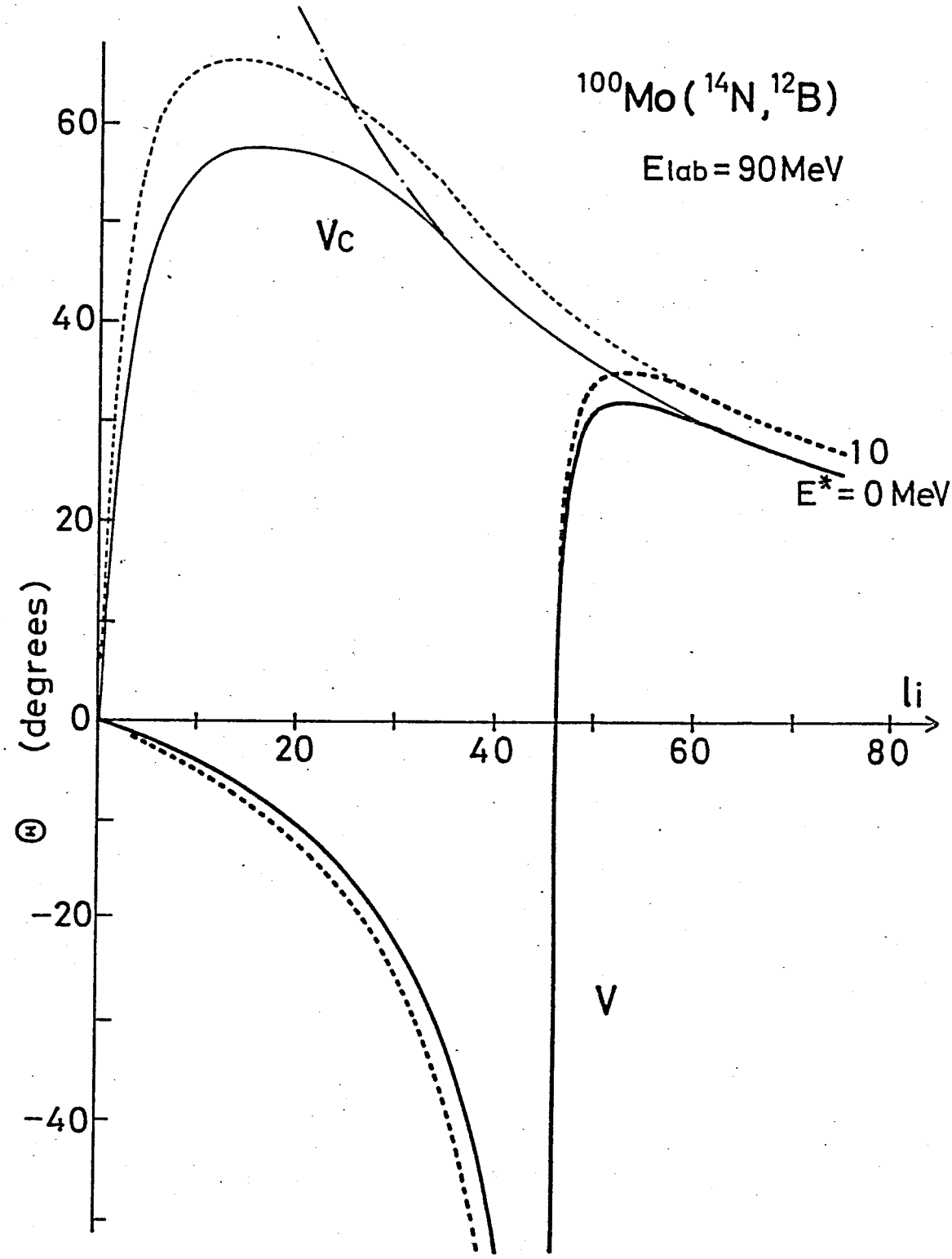
$^{100}Mo(^{14}N,^{12}B)$
Elab = 90MeV
Vc
V
10
E* = 0 MeV
60
40
20
0
-20
-40
20
40
60
80
li
Θ (degrees)

Fig. 12.

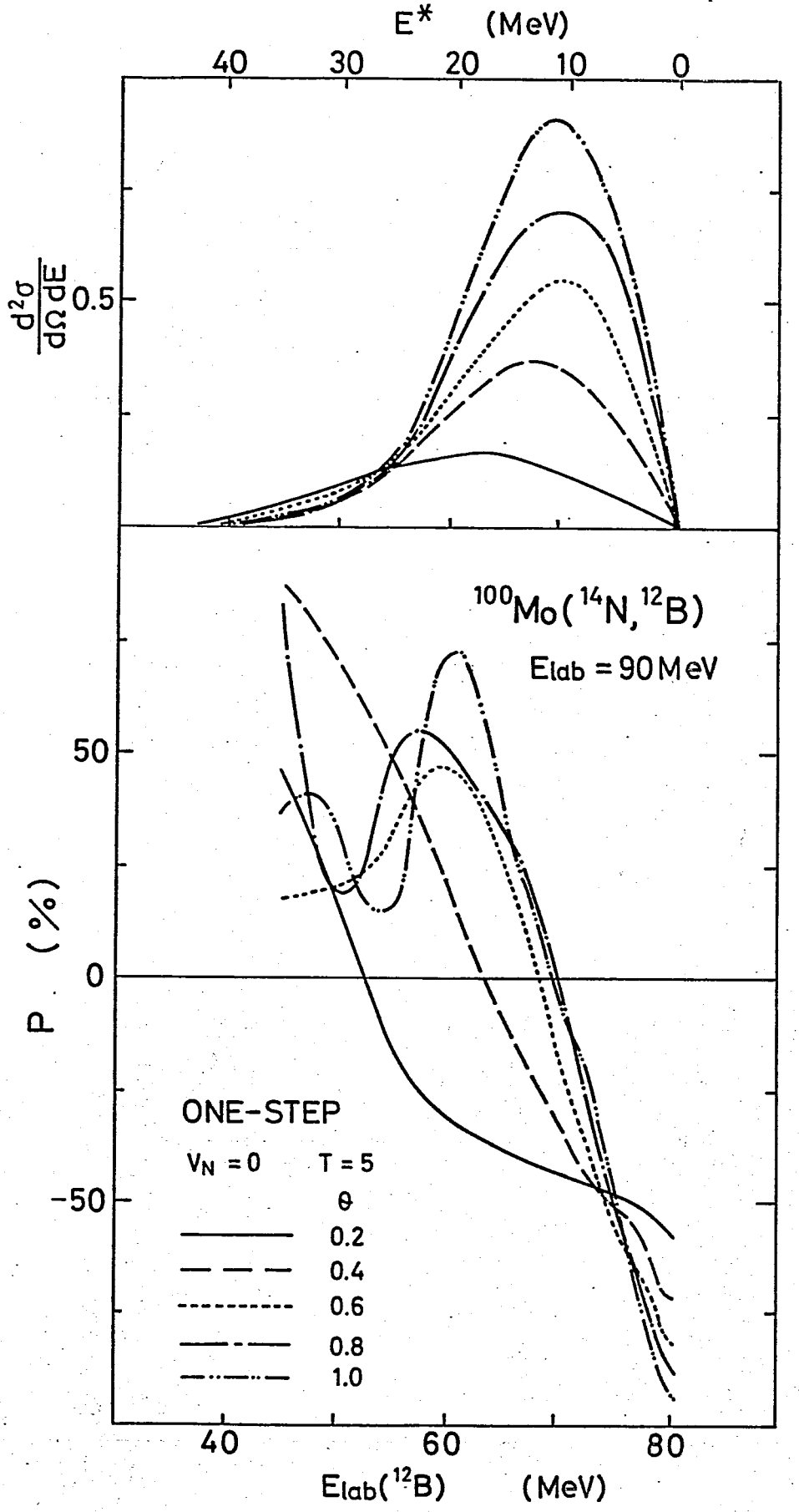
E* (MeV)
40
30
20
10
0
$\frac{d^2\sigma}{d\Omega dE}$
0.5
$^{100}Mo(^{14}N,^{12}B)$
Elab = 90 MeV
50
P (%)
0
ONE-STEP
V_N = 0
T = 5
θ
0.2
0.4
0.6
0.8
1.0
-50
40
60
80
Elab(^{12}B) (MeV)

Fig. 13.

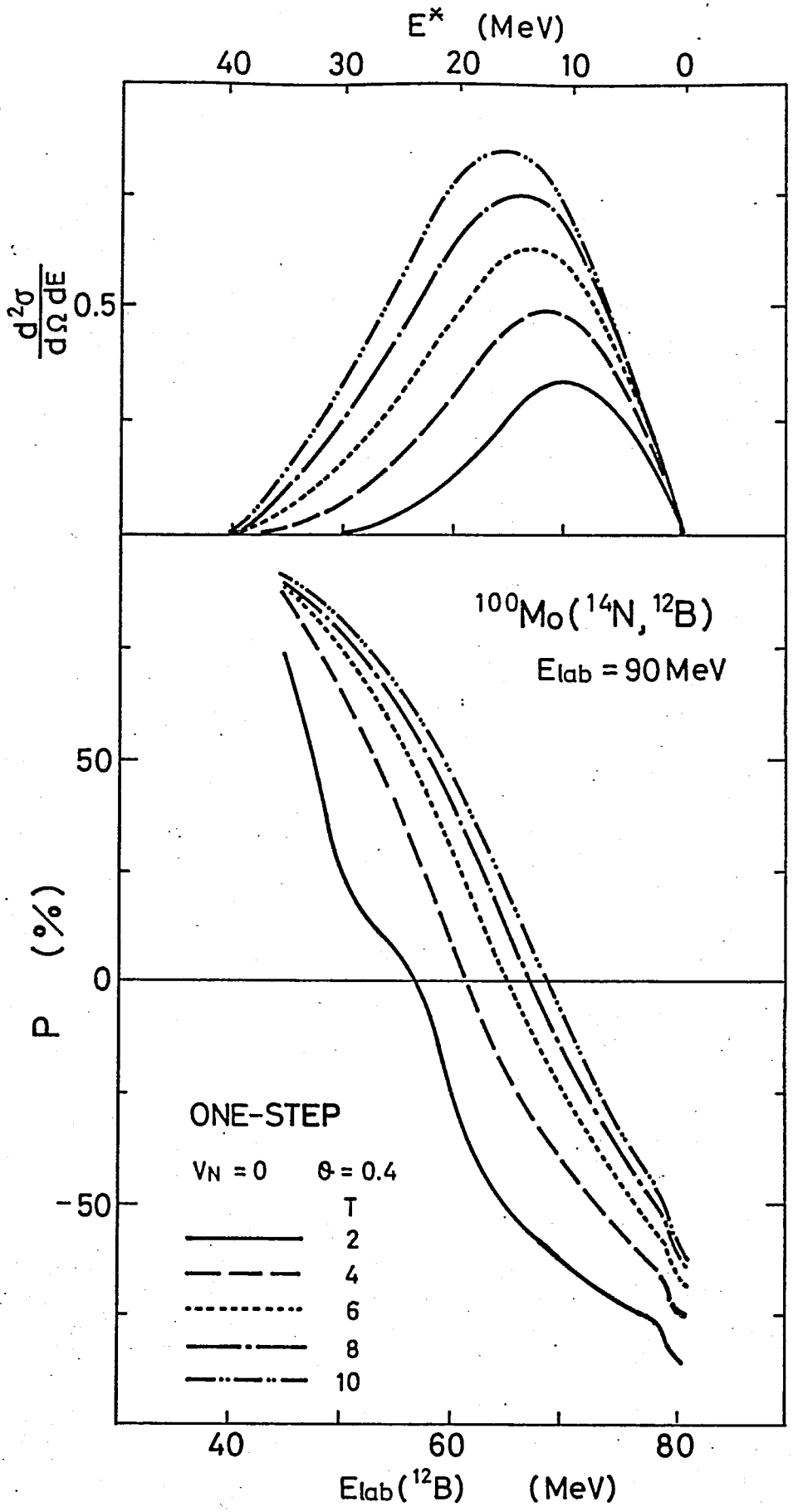
E* (MeV)
40
30
20
10
0
$\frac{d^2\sigma}{d\Omega dE}$
0.5
$^{100}Mo(^{14}N, ^{12}B)$
E_{lab} = 90 MeV
50
0
P (%)
-50
ONE-STEP
V_N = 0
θ = 0.4
T
2
4
6
8
10
40
60
80
$E_{lab}(^{12}B)$ (MeV)

Fig. 14.

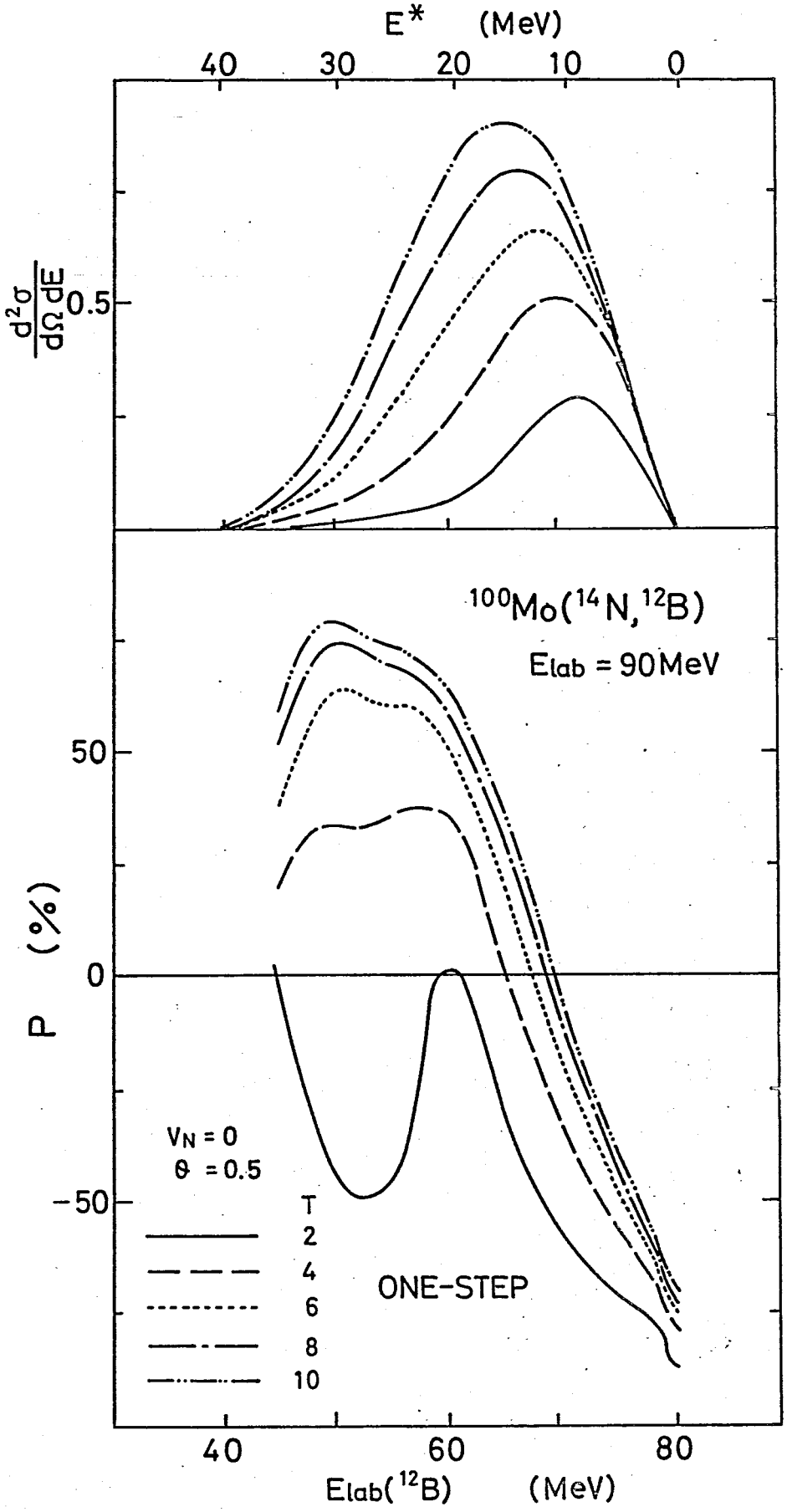
E* (MeV)
40
30
20
10
0
$\frac{d^2\sigma}{d\Omega dE}$
0.5
$^{100}Mo(^{14}N,^{12}B)$
Elab = 90MeV
50
P (%)
0
$V_N = 0$
$\theta = 0.5$
−50
T
2
4
6
8
10
ONE-STEP
40
60
80
Elab(^{12}B) (MeV)

Fig. 15.

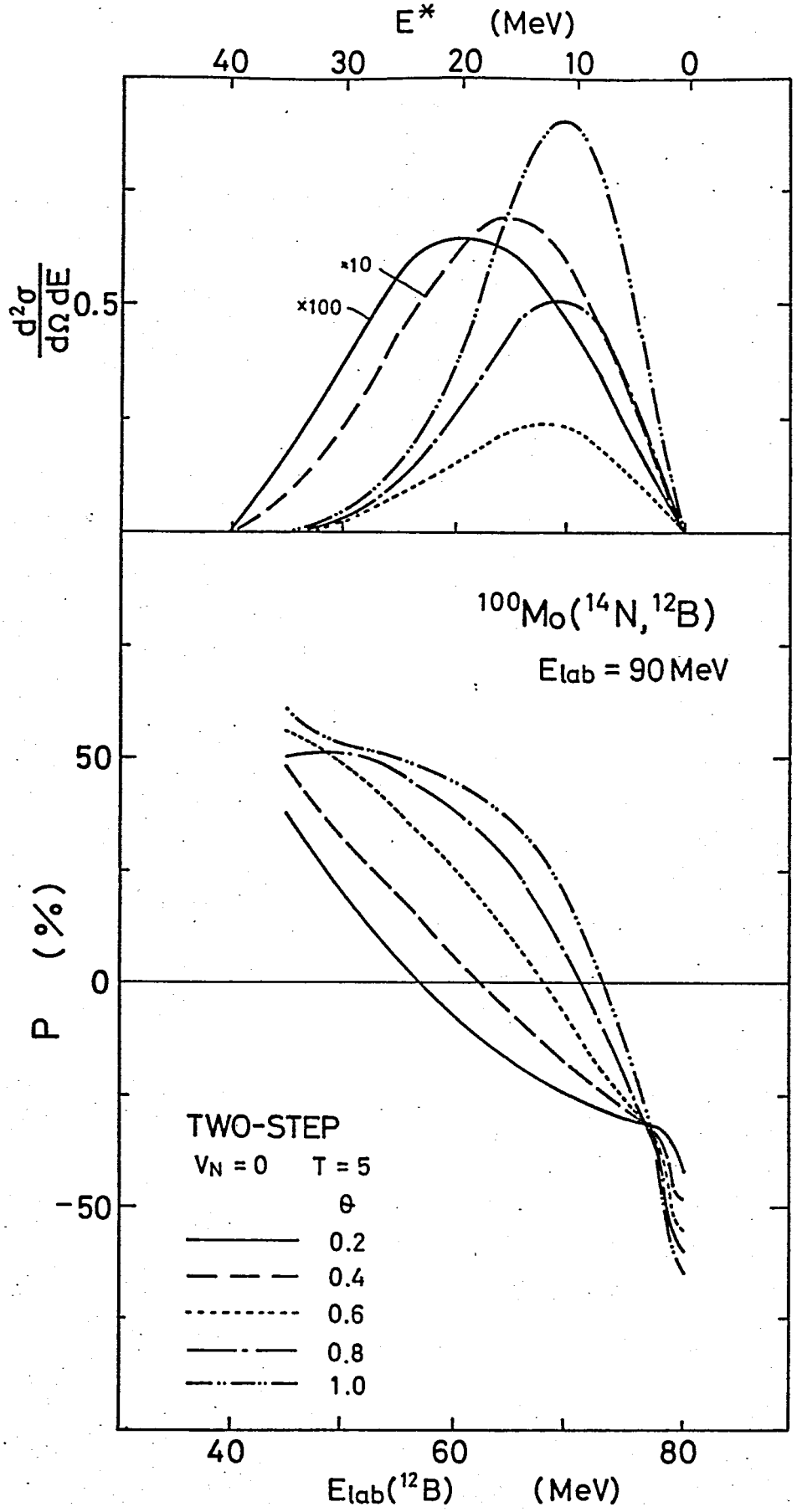
E* (MeV)
40
30
20
10
0
$\frac{d^2\sigma}{d\Omega dE}$
0.5
×10
×100
$^{100}Mo(^{14}N,^{12}B)$
E_{lab} = 90 MeV
50
0
−50
P (%)
TWO-STEP
V_N = 0 T = 5
θ
0.2
0.4
0.6
0.8
1.0
40
60
80
$E_{lab}(^{12}B)$ (MeV)

Fig. 16.

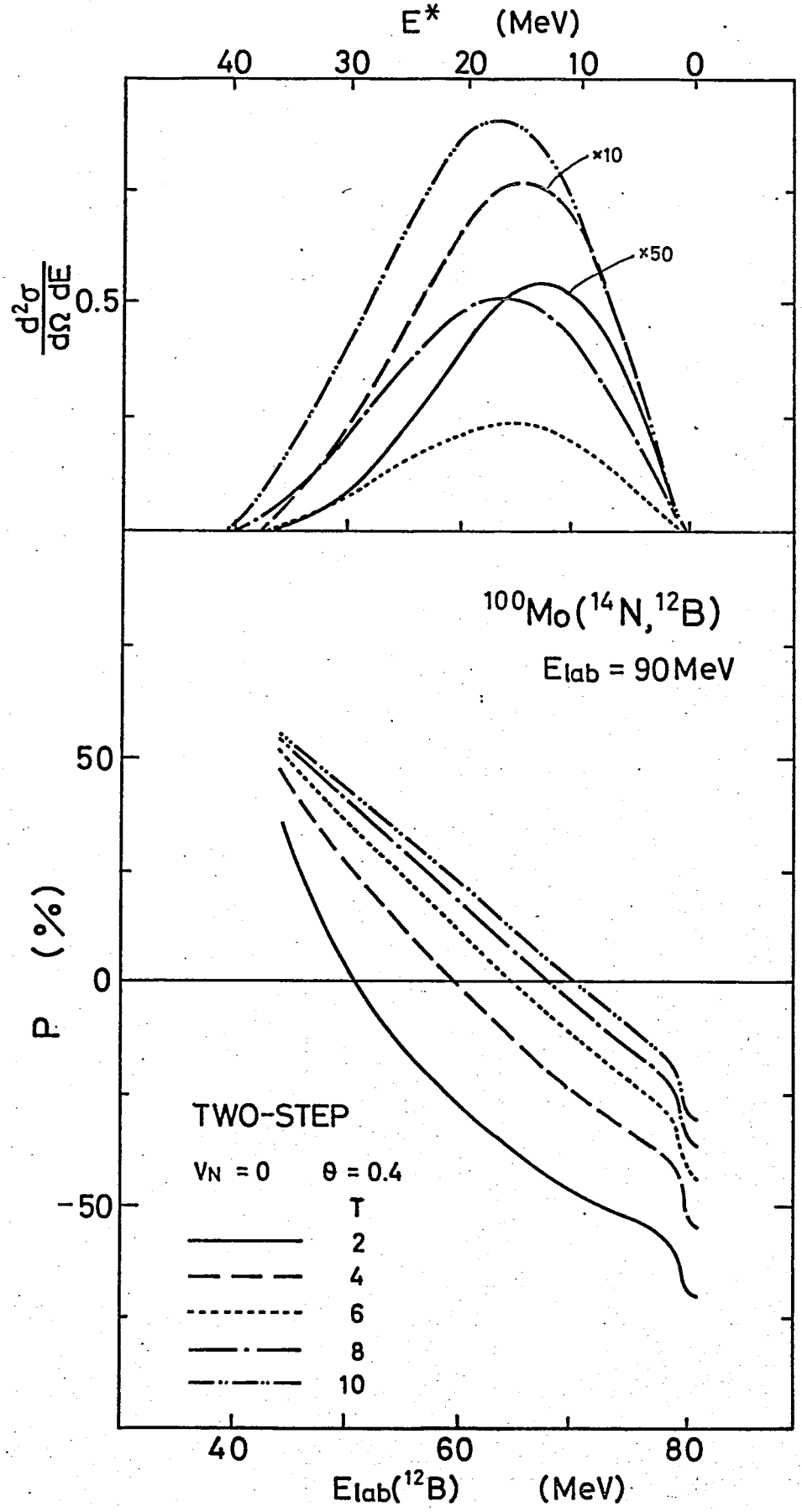
E* (MeV)
40
30
20
10
0
×10
×50
$\frac{d^2\sigma}{d\Omega\, dE}$
0.5
$^{100}Mo(^{14}N,^{12}B)$
E_{lab} = 90MeV
50
0
−50
P (%)
TWO-STEP
V_N = 0
θ = 0.4
T
2
4
6
8
10
40
60
80
$E_{lab}(^{12}B)$ (MeV)

Fig. 17.

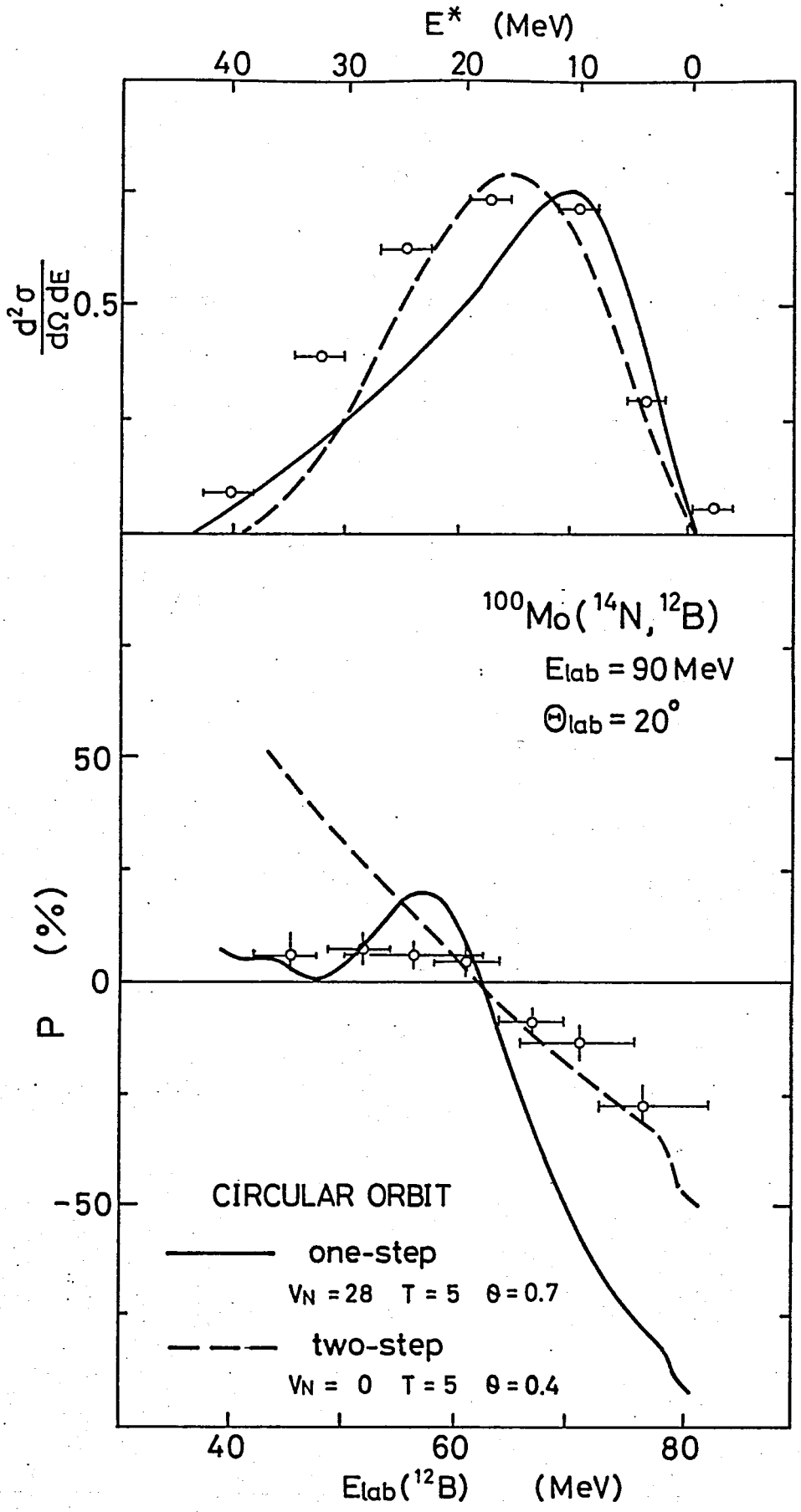
E* (MeV)
40
30
20
10
0
$\frac{d^2\sigma}{d\Omega\, dE}$
0.5
$^{100}Mo(^{14}N, ^{12}B)$
E_{lab} = 90 MeV
Θ_{lab} = 20°
50
P (%)
0
-50
CIRCULAR ORBIT
one-step
V_N = 28 T = 5 θ = 0.7
two-step
V_N = 0 T = 5 θ = 0.4
40
60
80
$E_{lab}(^{12}B)$ (MeV)

Fig. 18.

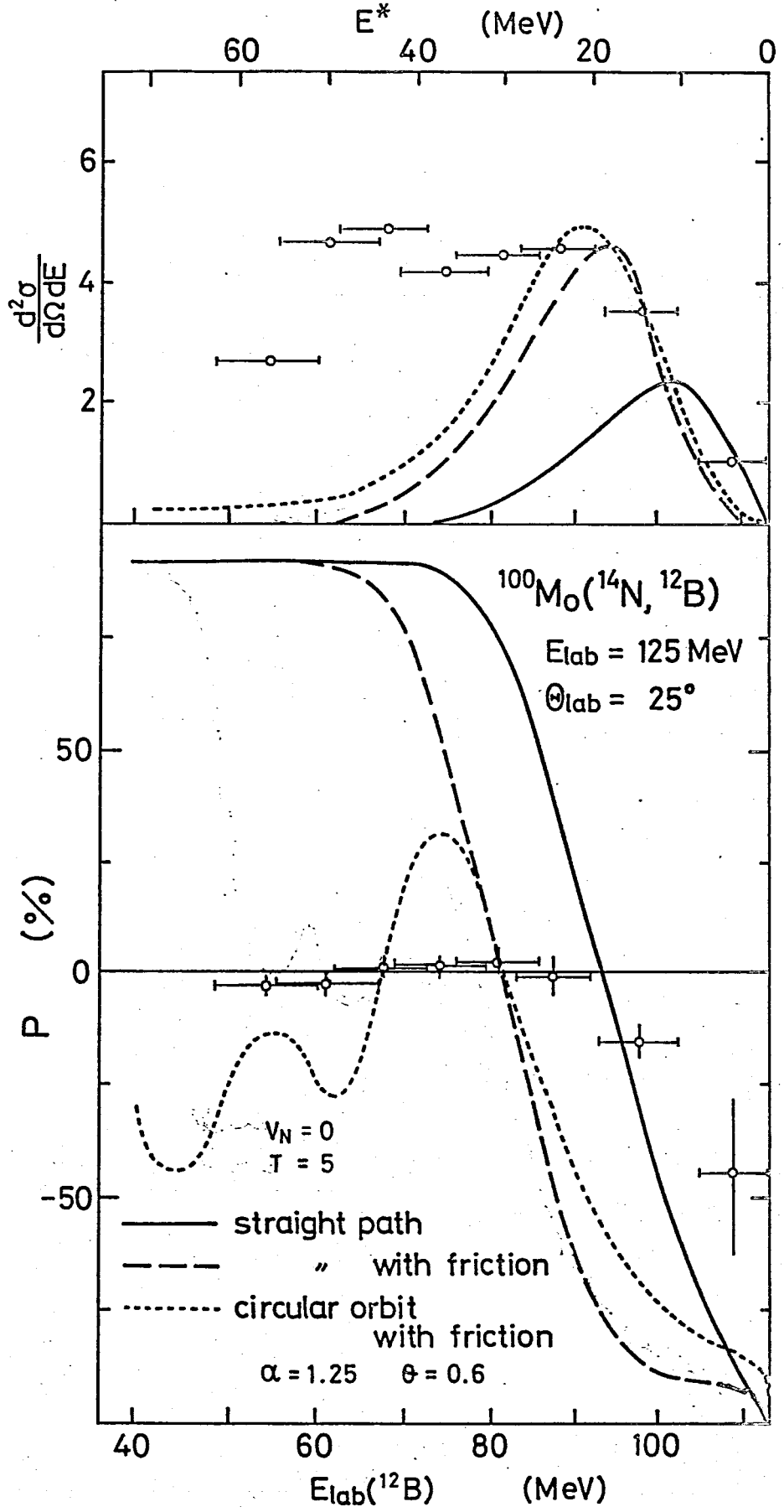
E* (MeV)
60
40
20
0
6
4
2
$\frac{d^2\sigma}{d\Omega dE}$
$^{100}Mo(^{14}N, ^{12}B)$
E_{lab} = 125 MeV
Θ_{lab} = 25°
50
0
-50
P (%)
V_N = 0
T = 5
straight path
" with friction
circular orbit with friction
α = 1.25 θ = 0.6
40
60
80
100
$E_{lab}(^{12}B)$ (MeV)

Fig. 19.

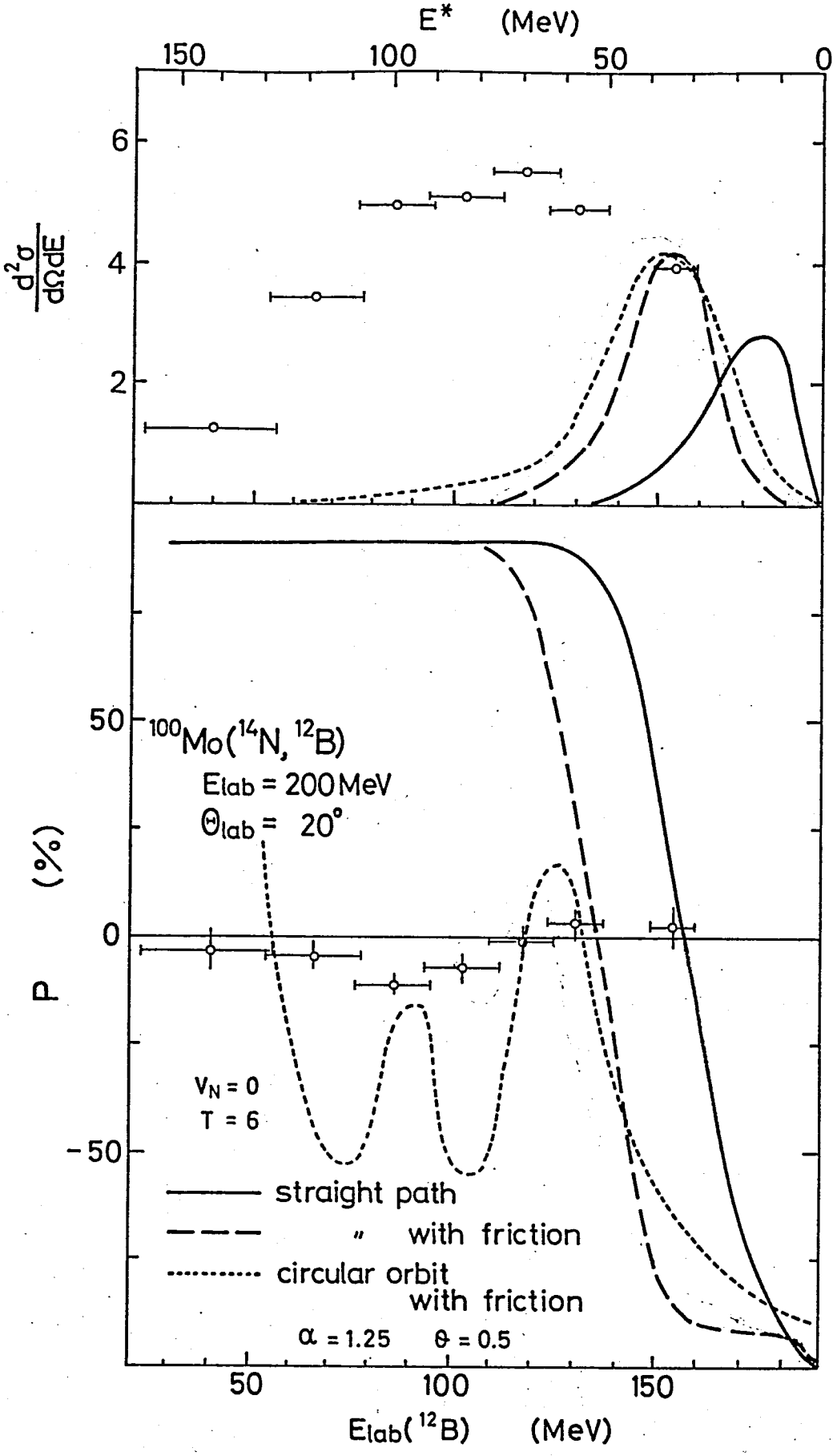
E* (MeV)
150
100
50
0
6
4
2
$\frac{d^2\sigma}{d\Omega dE}$
50
0
-50
P (%)
$^{100}Mo(^{14}N, ^{12}B)$
Elab = 200 MeV
Θ_{lab} = 20°
V_N = 0
T = 6
straight path
" with friction
circular orbit with friction
α = 1.25 θ = 0.5
50
100
150
Elab(^{12}B) (MeV)

Fig. 20.

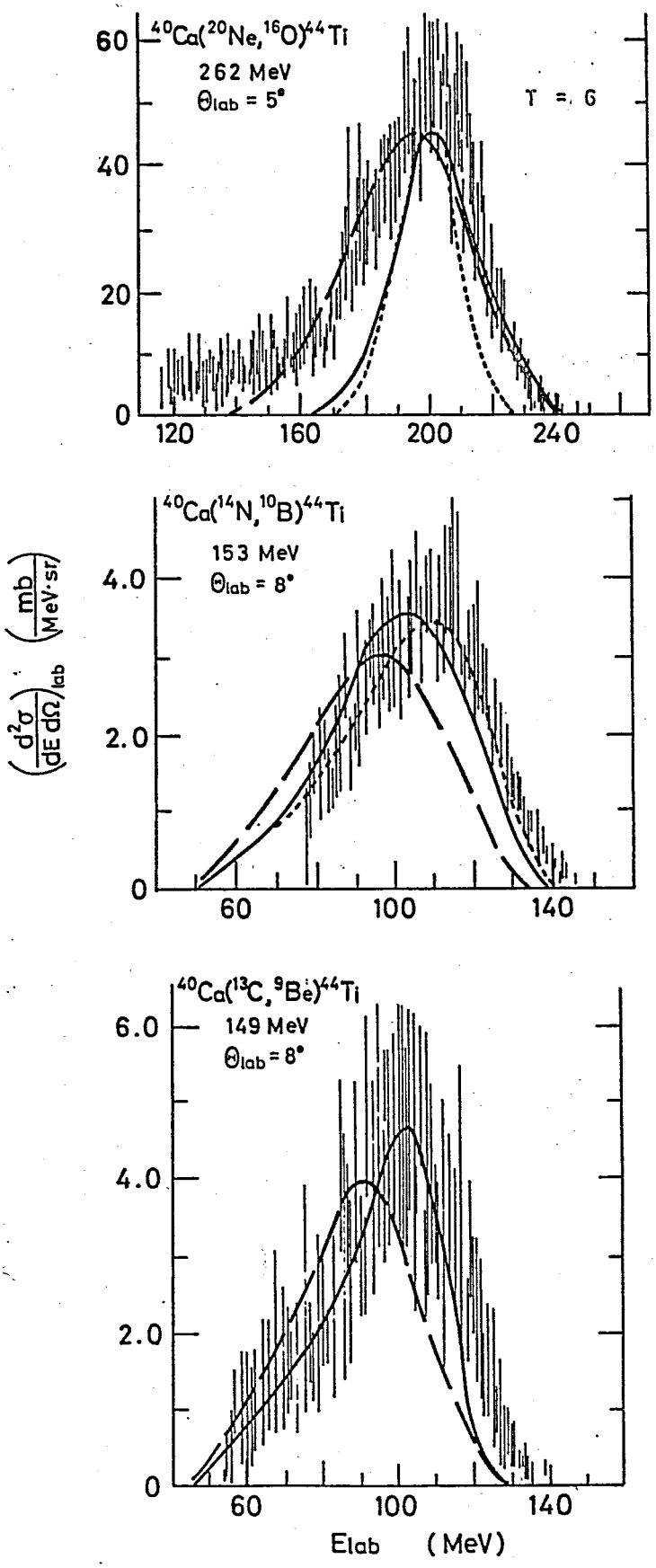
$^{40}Ca(^{20}Ne,^{16}O)^{44}Ti$
262 MeV
$\theta_{lab} = 5°$
T = 6
$^{40}Ca(^{14}N,^{10}B)^{44}Ti$
153 MeV
$\theta_{lab} = 8°$
$^{40}Ca(^{13}C,^{9}Be)^{44}Ti$
149 MeV
$\theta_{lab} = 8°$
$\left(\frac{d^2\sigma}{dE\,d\Omega}\right)_{lab}$ $\left(\frac{mb}{MeV \cdot sr}\right)$
E_{lab} (MeV)

Fig. 21.

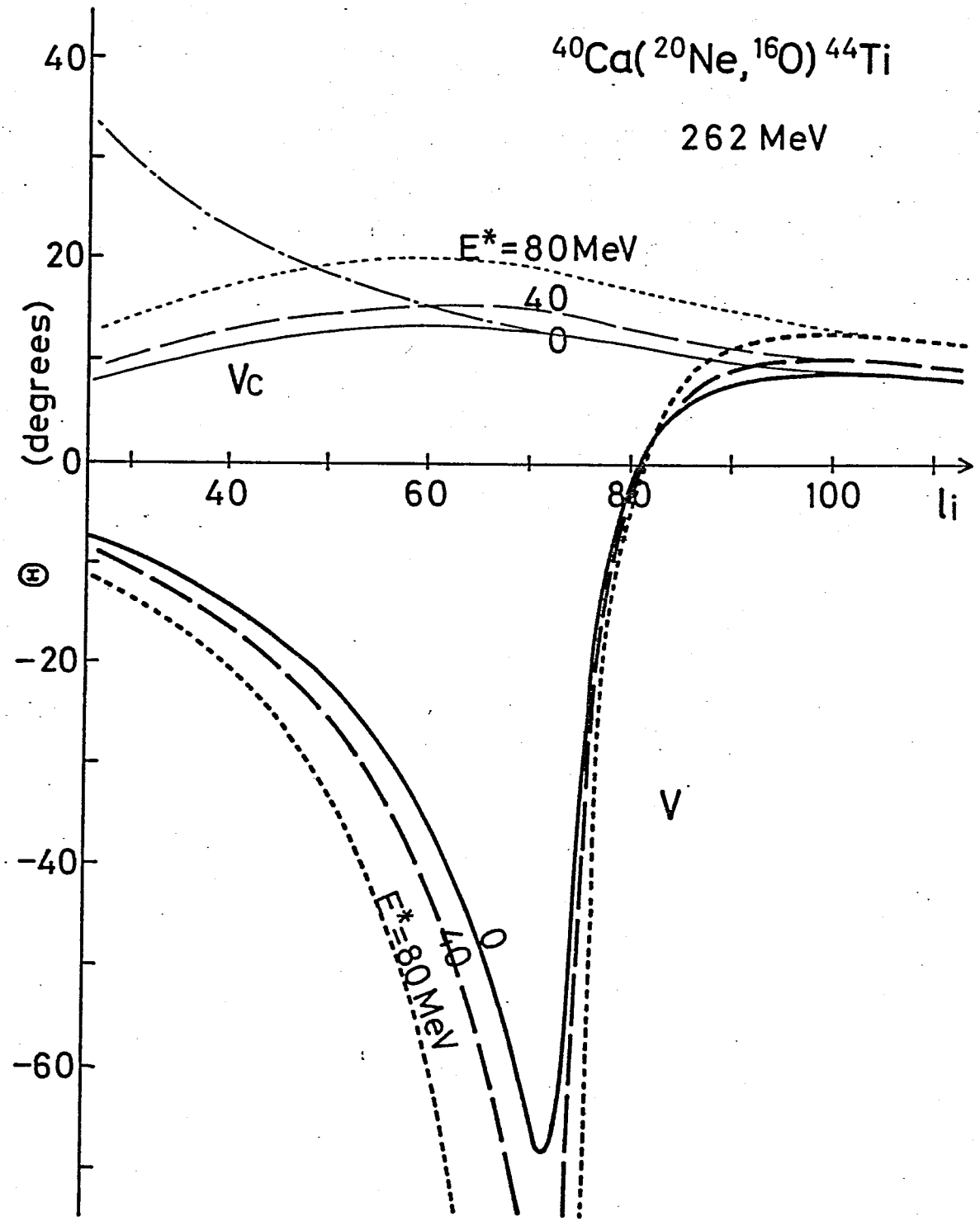
$^{40}Ca(^{20}Ne,^{16}O)^{44}Ti$
262 MeV
E*=80MeV
40
0
Vc
40
20
0
−20
−40
−60
(degrees)
Θ
40
60
80
100
li
V
E*=80MeV
40
0

Fig. 22.

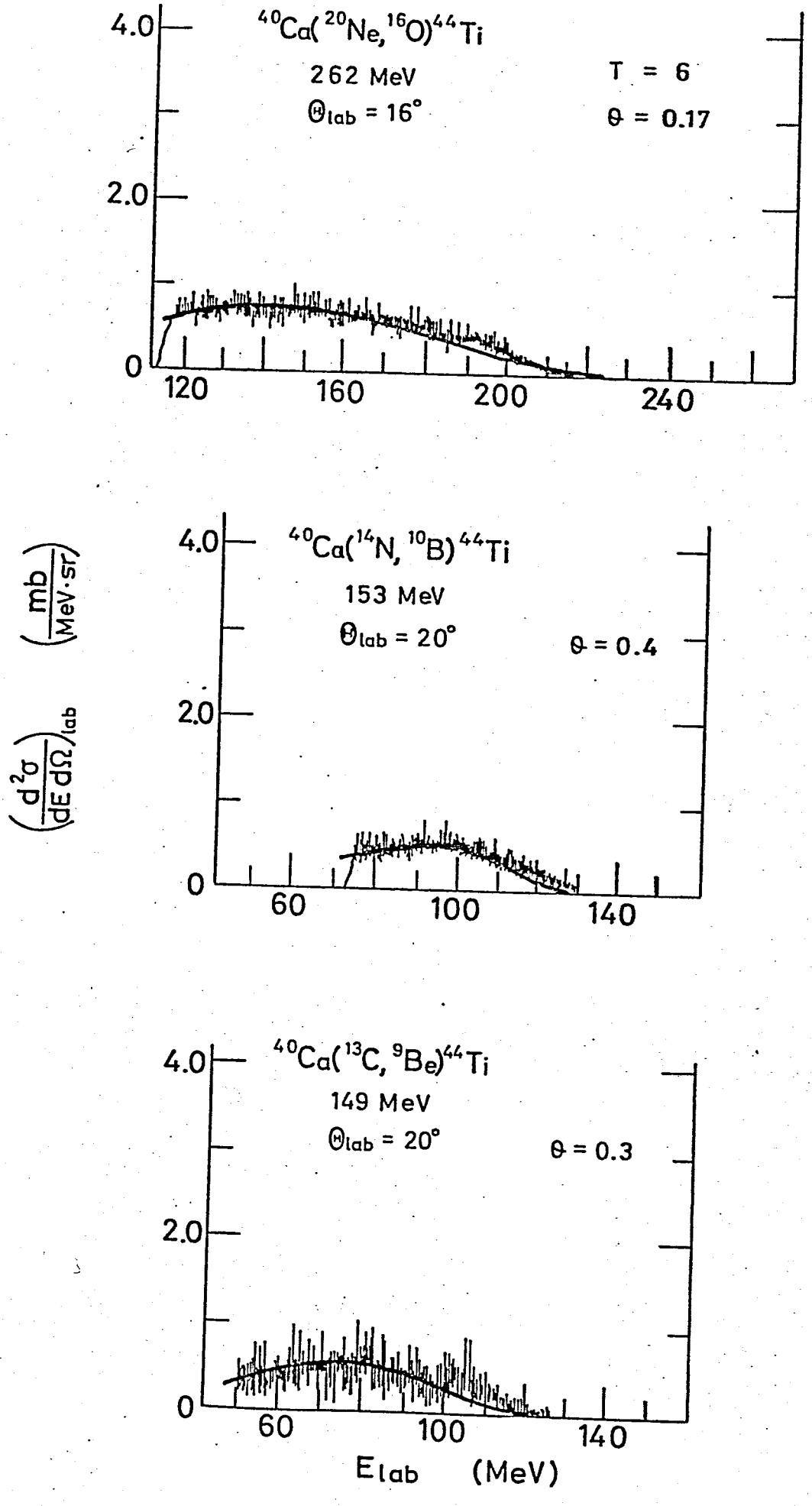
$^{40}Ca(^{20}Ne,^{16}O)^{44}Ti$
262 MeV
$\Theta_{lab} = 16°$
T = 6
θ = 0.17
$^{40}Ca(^{14}N,^{10}B)^{44}Ti$
153 MeV
$\Theta_{lab} = 20°$
θ = 0.4
$^{40}Ca(^{13}C,^{9}Be)^{44}Ti$
149 MeV
$\Theta_{lab} = 20°$
θ = 0.3
$\left(\frac{d^2\sigma}{dE\,d\Omega}\right)_{lab}$ $\left(\frac{mb}{MeV \cdot sr}\right)$
4.0
2.0
0
120
160
200
240
60
100
140
E_{lab} (MeV)

Fig. 23.

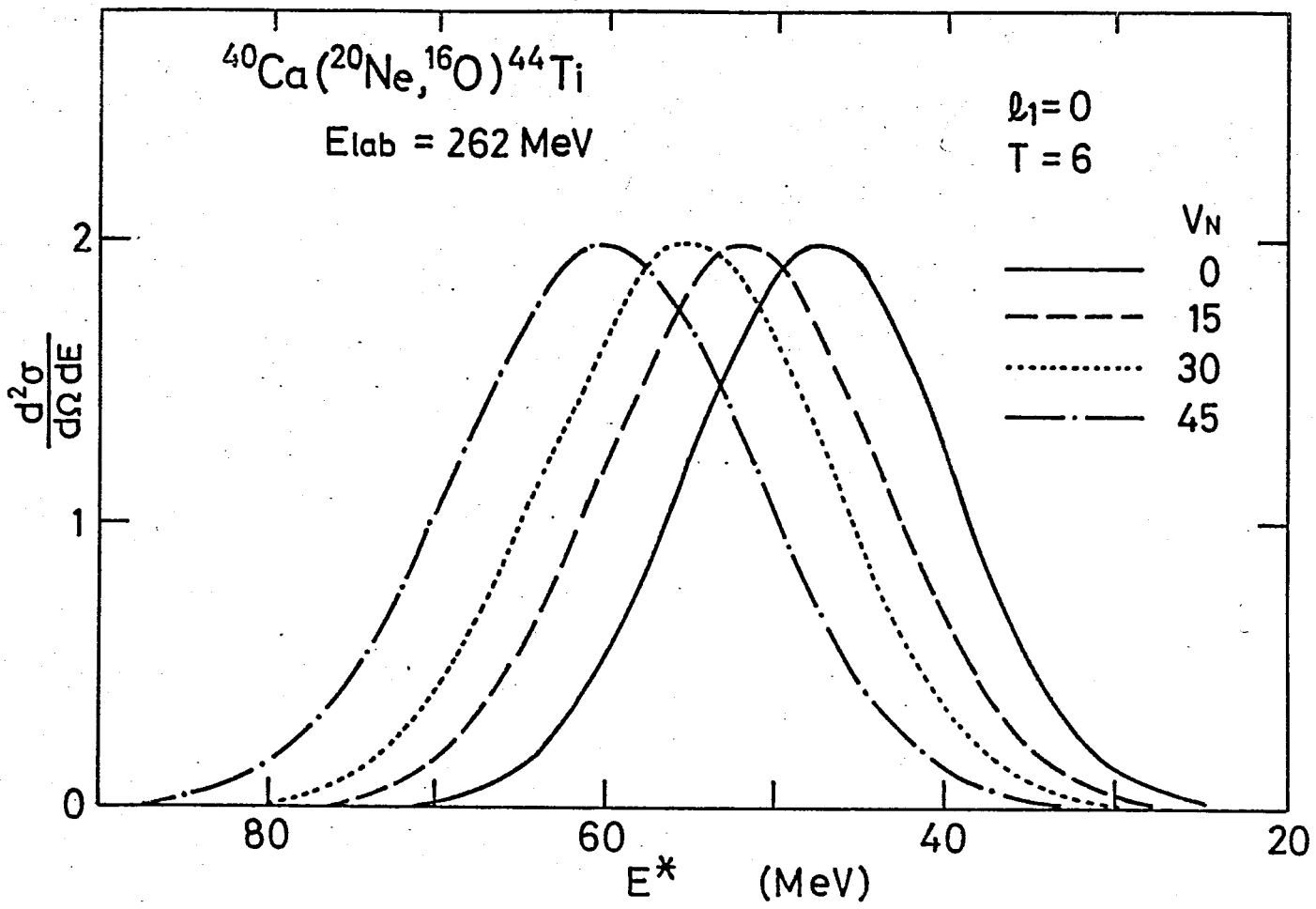
$^{40}Ca(^{20}Ne,^{16}O)^{44}Ti$
Elab = 262 MeV
$\ell_1 = 0$
T = 6
V_N
0
15
30
45
$\frac{d^2\sigma}{d\Omega\, dE}$
2
1
0
80
60
40
20
E* (MeV)

Fig. 24.

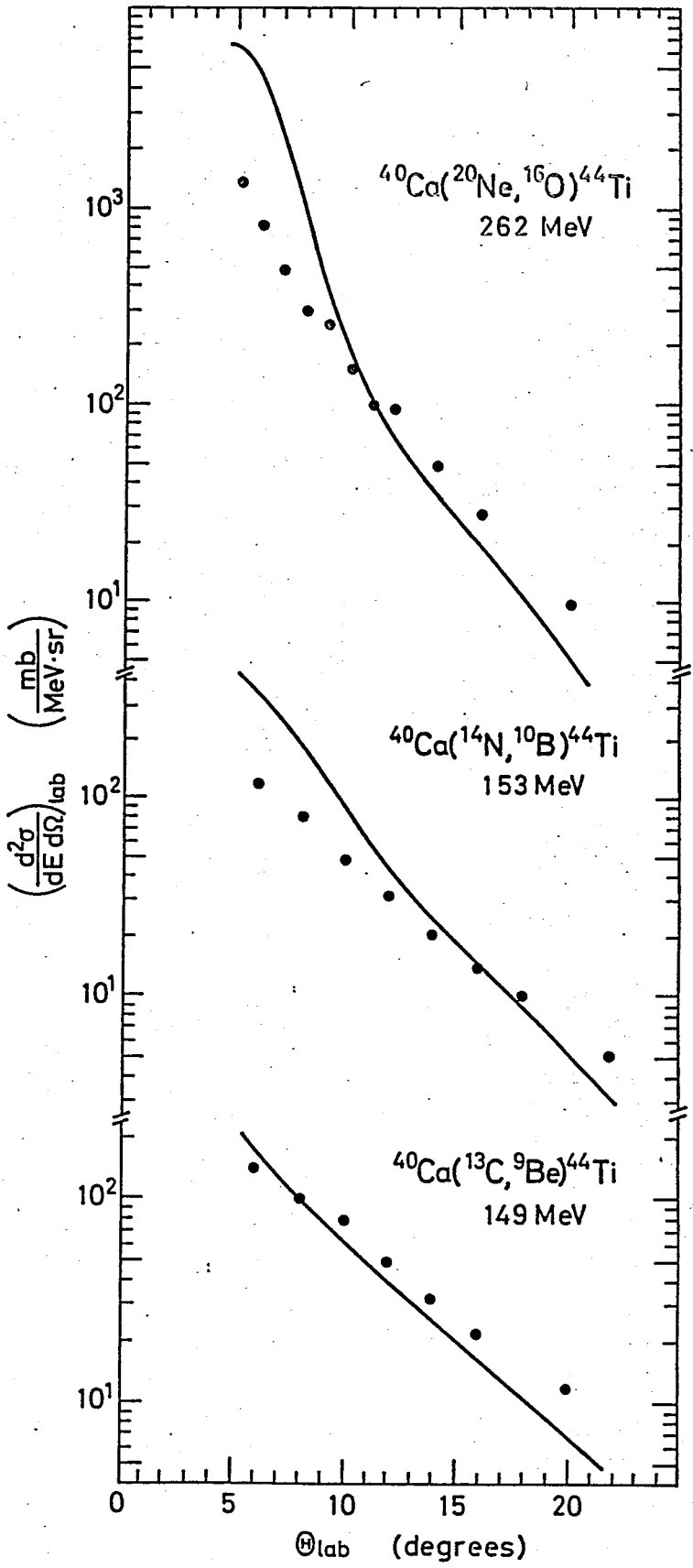
$^{40}Ca(^{20}Ne,^{16}O)^{44}Ti$
262 MeV
$^{40}Ca(^{14}N,^{10}B)^{44}Ti$
153 MeV
$^{40}Ca(^{13}C,^{9}Be)^{44}Ti$
149 MeV
$\left(\frac{d^2\sigma}{dE\,d\Omega}\right)_{lab}$ $\left(\frac{mb}{MeV\cdot sr}\right)$
10^3
10^2
10^1
10^2
10^1
10^2
10^1
0
5
10
15
20
Θ_{lab} (degrees)

Fig. 25.

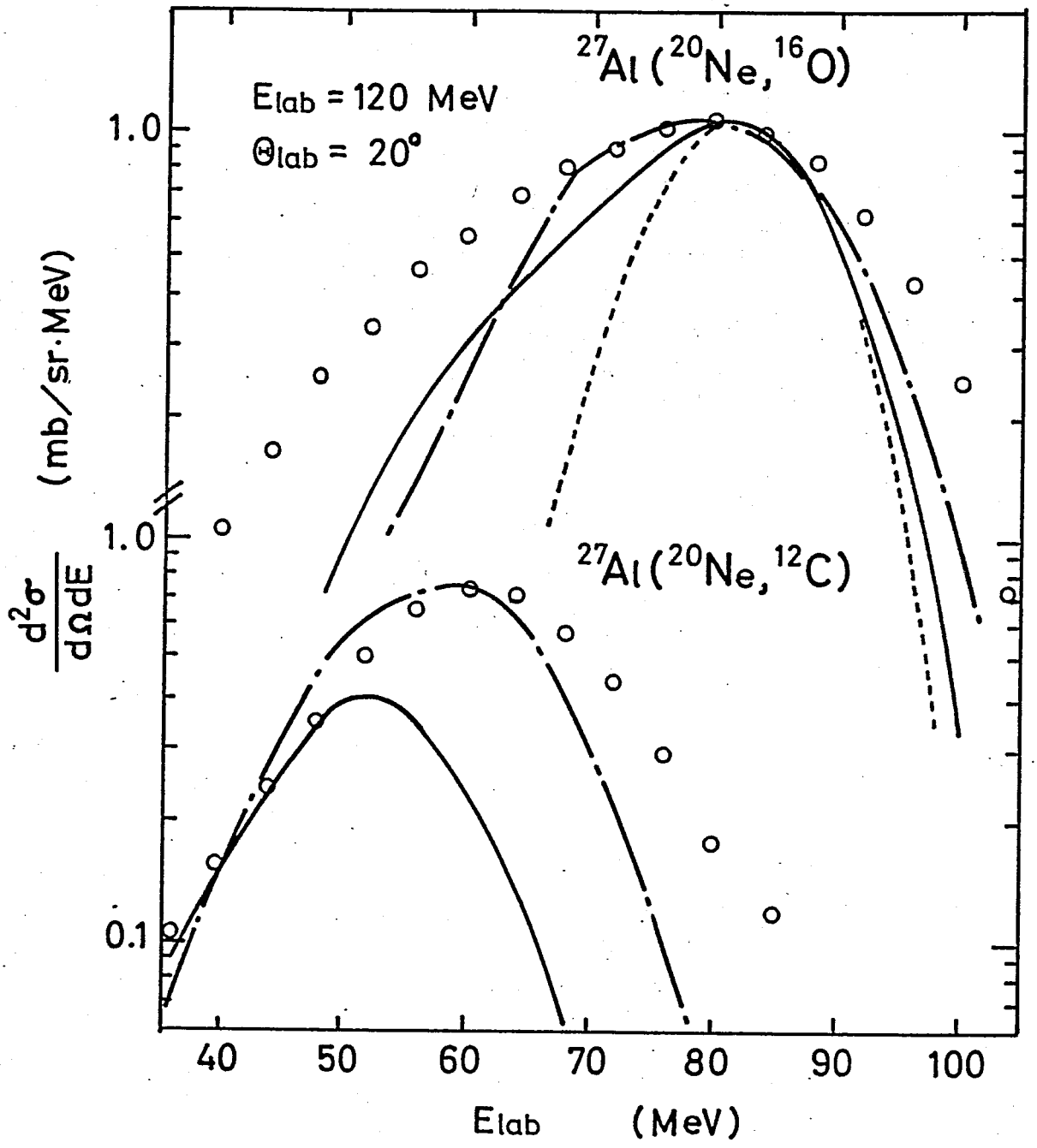
^{27}Al (^{20}Ne, ^{16}O)
E_{lab} = 120 MeV
Θ_{lab} = 20°
^{27}Al (^{20}Ne, ^{12}C)
1.0
1.0
0.1
$\frac{d^2\sigma}{d\Omega dE}$ (mb/sr·MeV)
40
50
60
70
80
90
100
E_{lab} (MeV)

Fig. 26.

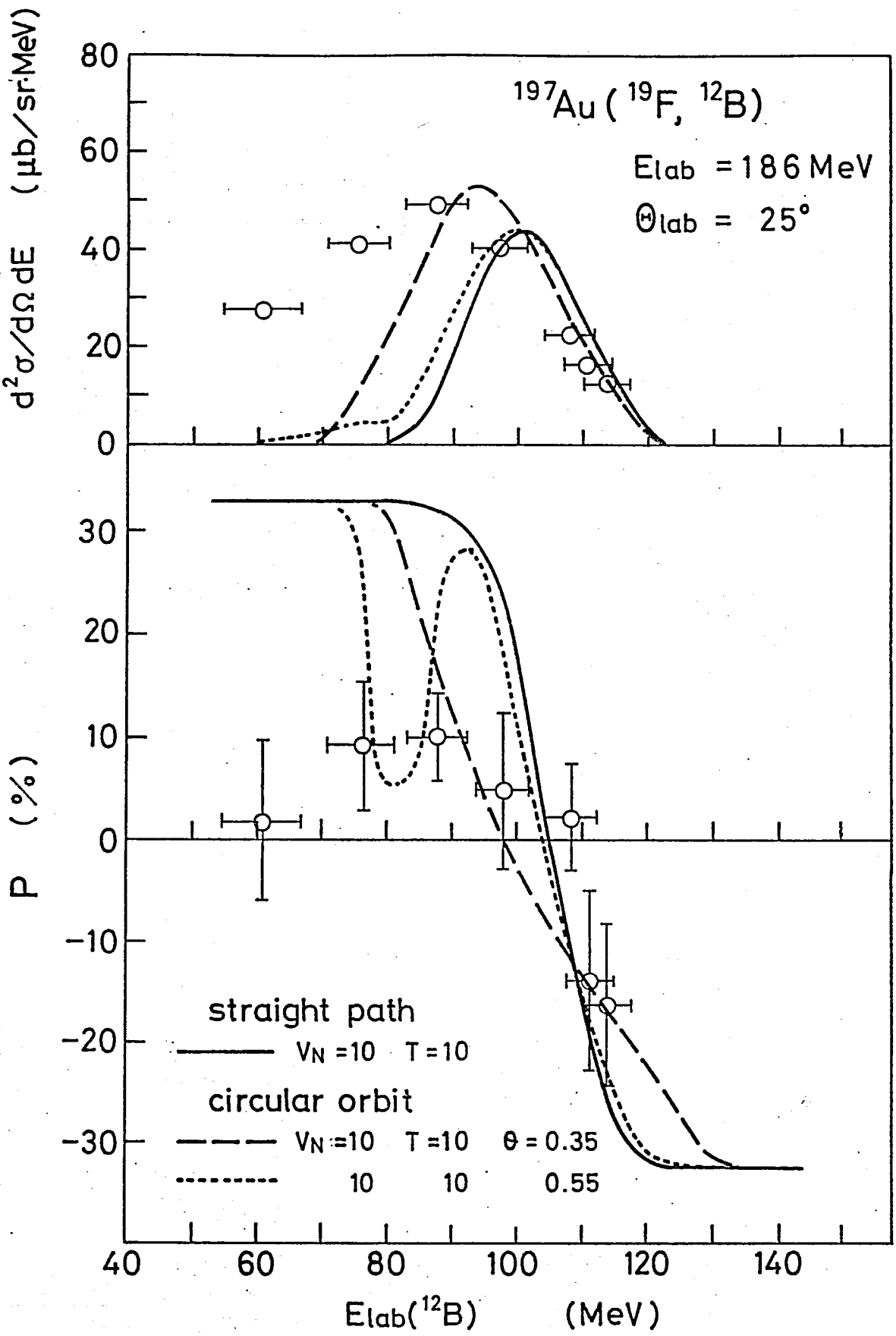
$^{197}Au(^{19}F, ^{12}B)$
Elab = 186 MeV
θlab = 25°
d²σ/dΩdE (μb/sr·MeV)
P (%)
straight path
VN = 10 T = 10
circular orbit
VN = 10 T = 10 θ = 0.35
10 10 0.55
Elab(12B) (MeV)

Fig. 27.